Mathematical modelling of all-optical buffering for ultrafast optical time division multiplexed networks.

ALS, Adrian A.

charged at **50p per** dour

REFERENCE

Mathematical Modelling of All-optical Buffering for Ultrafast Optical Time Division Multiplexed Networks

Adrian Andrew Als

A thesis submitted in partial fulfilment of the requirements of

Sheffield Hallam University

for the degree of Doctor of Philosophy

June 2004

GLOSSARY OF ABBREVIATIONS

AON	All-Optical Network
APON	Asynchronous Transfer Mode Based Passive Optical Network
ASE	Amplified Spontaneous Emission
ATM	Asynchronous Transfer Mode
AWGN	Additive White Gaussian Noise
BER	Bit Error Rate
BISDN	Broadband Integrated Service Data Network
BOD	Bandwidth on Demand
BPM	Beam Propagation Method
CATV	Cable Antenna Television
CCITT	International Telegraph and Telephone Consultative Committee
CCW	Counter Clockwise
CPMZ	Colliding Pulse Mach Zehnder
CW	Clockwise
DSF	Dispersion Shifted Fibre
DWDM	Dense Wavelength Division Multiplexing
E/O	Electro-Optic
EDFA	Erbium-doped Fibre Amplifier
FDM	Frequency Division Multiplexing
FP-SLA	Fabry-Perot Semiconductor Optical Amplifier
FWHM	Full Width Half Maximum
FWM	Four Wave Mixing
GVD	Group Velocity Dispersion
ITUT-T	International Telecommunications Union – Telecommunications Sector
LAN	Local Area Network
MEMS	Micro-Electro-Mechanical Systems
MZI	Mach Zehnder Interferometer
NLE	Non-Linear Element
NLSE	Non-Linear Schrödinger Equation

NLWG	Non-Linear Wave Guide
NOLM	Non-Linear Optical Loop Mirror
NRZ	Non-Return-to-Zero
O/E	Opto-Electronic
OC	Optical Carrier
OEO	Opto-Electro-Optical
OOK	On Off Keying
OTDM	Optical Time Division Multiplexing
PDH	Plesiochronous Digital Hierarchy
POTS	Plain Old Telephone System
PSDN	Packet Switched Data Network
QoS	Quality of Service
RAM	Random Access Memory
RFLB	Recirculating Fibre Loop Buffer
RZ	Return-to-Zero
SBS	Stimulated Brillouin Scattering
SDH	Synchronous Digital Hierarchy
SLA/SOA	Semiconductor Laser Amplifier / Semiconductor Optical Amplifier
SLALOM	Semiconductor Laser Amplifier Loop Optical Mirror
SMF	Single Mode Fibre
SMZ	Symmetric Mach Zehnder
SNR	Signal-to-Noise Ratio
SONET	Synchronous Optical Network
SPM	Self-Phase Modulation
SRS	Stimulated Raman Scattering
STM	Synchronous Transfer Mode
STS	Synchronous Transport System
TDM	Time division Multiplexing
TOAD	Terahertz Optical Asymmetric Demultiplexer
TON	Transparent Optical Network
TWA	Travelling Wave Amplifier
UNI	Ultra-fast Non-linear Interferometer

GLOSSARY OF SYMBOLS

Symbol	Definition
$\hat{D}$	Differential operator
$\hat{N}$	Non-linear operator
ω	Angular Frequency
κ	Attenuation
ρ	Change density
Γ	Confinement factor
γ	Non-linear coefficient
θ	Phase
λ	Wavelength
$\chi^{(i)}$	i^{th} order material susceptibility
μ_0	Permeability of a vacuum
ε_0	Permittivity of a vacuum
β_0	Propagation constant
β_1	Inverse of the pulse velocity
β_2	Group velocity dispersion (GVD) parameter
β_3	Third order dispersion parameter
α_{AMP}	Internal waveguide scattering loss
τ_c	Recombination time
ϑ_{cf}	Coupling factor
α_{dB}	Intrinsic fibre loss (in decibels)
α_l	Fibre loss per loop iteration
ψ_{lef}	Line enhancement factor
ϕ_{NL}	SPM phase shift
Δt	Time difference between the two control pulses
$A(z,t)$	Slowly varying envelope of optical pulse at spatial position z and time t
A_{eff}	Effective fibre core area
A_r	Relative amplitude
B	Bit rate
B	Magnetic flux density

B_e	Electrical bandwidth
B_o	Optical bandwidth
C	Speed of light in a vacuum
D	Electric flux density
E	Electric field vectors
E_0	Signal energy
G	Amplifier gain
$g(N)$	Material gain coefficient
G_0	Small signal gain
g_B	Brillouin gain coefficient
g_R	Raman gain coefficient
H	Magnetic field vectors
h	Planck's constant
I	Optical intensity
I_B	Bias current
J	Current density
K_B	Boltzmann constant
L	Length
L_A	Amplification period
L_{AMP}	Amplifier length
L_D	Dispersion length
L_{eff}	Effective fibre length
l_n	Loop traversal number
L_{NL}	Non-linear length
M	Magnetisation polarisation
M	Storage capacity in bits
N	Carrier density
n	Refractive index of the fibre
N	Soliton Order
N_0	Noise spectral density
n_2	Non-linear refractive index
N_A	Number of amplifiers

n_{sp}	Spontaneous emission noise factor
N_{tr}	Carrier density at transparency
$\mathbf{P}$	Dielectric polarisation
P	Power
P_0	Peak power
P_b	Probability of a bit error
q	Electron charge
q_0	½ the time separation between two adjacent soliton pulse
R	Photodiode responsitivity
R_L	Load resistance
S_{sp}	Noise spectral density of optical amplifier
T	Temperature
t	Time
T_0	Normalised pulse width
T_B	Bit period
T_{FWHM}	FWHM pulse width
T_{Loop}	Unit loop traversal time
V	Volume of active medium
X_{ratio}	Normalised crosstalk energy ratio
z	Distance
Z_0	Soliton Period
Δx	Eccentricity of SOA
τ_{win}	Temporal duration of switching window

LIST OF FIGURES

LIST OF TABLES

ACKNOWLEDGEMENTS

I would like to thank God first for his blessings, and second, the experiences and opportunities afforded me during the course of my research. Without Him, this journey would have been impossible.

I would like to thank my director of studies, Prof. Ghassemlooy, for his inspirational guidance and support. He has been an invariable source of help throughout the research project.

I would like to acknowledge the USENIX committee as this work would not be possible without the financial support provided by the USENIX Scholars Program in the form of a scholarship during the second year of my PhD project. Moreover, I am indebted to Dr. Fabian Monrose for his kind endorsement on my behalf to the USENIX committee. His patience and persistence ensured my scholarship was approved, and that my internship at Lucent Technologies was assured.

Many thanks to my other supervisors, Dr. Graham Swift, Dr. Jacques Chi and Prof. Peter Ball for their academic support especially during the tedious proofreading and editing sessions before publications.

To my peers in the Optical Communications Research Group, I extend my kindest gratitude. The weekly discussion sessions provided stimulus whenever I was perplexed by a problem, and ensured that I was always keenly aware of the developments within the related research fields.

I am grateful for the encouragement and support provided by the many friends I made in Sheffield, especially Laurence, George, David, Firat and Boran.

Finally, I would like to thank the home circle: my parents, Zastron and Arlene Als; my inspiration, Margarette Mayers; and my relatives in London, Noel and Donna Layne, for their unwavering support, their empathetic ears and steadfast love.

ABSTRACT

The development of a practical solution to all-optical buffer remains a challenge for high-speed (≥ 20 Gbit/s) optical networks. Most of the research in the field has concentrated on building test-bed solutions, however the literature review shows little evidence in the use of mathematical models to aid in the design process. This PhD study is an attempt to design and develop a mathematical model of an all-optical buffer suitable for use within optical time division multiplexed systems. The emphasis is placed on recirculating fibre loop buffers because of their inherent storage advantages. The most critical of these advantages is that the storage delay time is independent of the fibre length.

While there is a precedent of employing large recirculating fibre loop architectures to simulate ultra-long haul transmission lines in research projects, their use in short length (≤ 500m) buffering architectures is not prevalent in the literature. This work finds a niche in this domain where the physical effects of the buffer components (e.g. optical switches) have not been previously documented.

In order to optimise the bit error rate performance and characterise its dependence on the physical buffer characteristics, the buffer models are designed and simulated in MATLAB and VPI. The associated mathematical models, developed in this work, are validated by the results produced using these simulation packages.

The benefit of this research is reflected in the fact that varying the parameters of the mathematical model effectively simulates the changing of physical device characteristics. Consequently, the designing process becomes less arduous, as lengthy simulation times are now reduced. Moreover, as physical implementation can now be delayed until the buffer design is optimised, production cost may be reduced.

Chapter 1

Introduction

Over the last century, advances in technology have prompted the move from electrical to optical based communication networks. The primary motivation for this transition was the dramatic increase in the available bandwidth offered by the optical fibre. Additionally, the bulk manufacturing cost was comparably cheaper, there was increased security since it is difficult to physically tap, and the light waves travelling within optical fibres were immune to electromagnetic interference and crosstalk. Finally, as attenuation within the fibre is significantly lower than in electrical wiring, long-haul high capacity communication systems became feasible. The first generation optical systems comprised of point-to-point links with opto-electrical (O/E) and electro-optical (E/O) repeater stations littered along the path to maintain signal integrity. More recently, the proliferation of all-optical fibre-based communication systems has resulted from the relentless pursuit of increased bandwidth utilisation to satisfy consumer demands. Today optical networks employing wavelength division multiplexing (WDM) technology operating at tens of gigabits per second are commercially available. In such networks, each data channel has a unique optical carrier and may be transmitted simultaneously. However, the inherent growth of non-linear effects as the number of channels per optical fibre increases, places restrictions on the capacity of such systems.

An alternative approach, and an area of active research, is optical time division multiplexing (OTDM). In this scheme, the channels are time multiplexed and transmitted using a single wavelength at speeds in the region of hundreds of gigabits per

second. Consequently, the end node equipment is conceptually simpler as only one wavelength needs to be considered. OTDM is considered an essential feature of future all-optical networks because of its flexibility. Essentially, the number of channels can be varied without the need for additional hardware components (e.g. tuneable lasers) by simply adjusting the timing intervals. Although OTDM is not envisioned to be a replacement for WDM, it may be employed in scenarios where major traffic is carried by an OTDM backbone or where each channel in a WDM system is optically time division multiplexed to further increase the network capacity.

Solutions to the challenges facing the commercialisation of high-speed OTDM systems such as ultra-short pulse generation, add/drop time division multiplexing, optical regeneration, all-optical clock extraction and synchronisation has been demonstrated in many laboratories. However their large-scale non-commercialisation is due firstly, to the fact that they still remain to be proven economically beneficial in point-to-point link transmissions compared to current 10 and 40Gbit/s WDM systems. Secondly, they must ensure that high-speed (>100Gbit/s) systems comply with a flexible all-optical network and offer time-domain routing capabilities.

The importance of an all-optical buffering solution to resolve flow-control and contention resolution issues within high-speed OTDM networks cannot be ignored. In this work a buffering solution based on a recirculating fibre loop architecture is investigated by developing a mathematical model for both the passive and active versions of the device.

1.1 Organisation of Thesis

The thesis is divided into eight chapters. Following the introduction, a literature review showing the history of communication networks is given in Chapter 2. This chapter highlights the various electrical switching strategies technologies, in chronological order, that preceded the transition to the optical domain. Additionally, the motivation behind WDM and OTDM and their associated challenges are discussed along with the envisioned future development of multiplexed network systems.

The performance of the optical buffer critically relies on the switching mechanism employed. Factors such as switching time, repetition rate, noise figure, integratability and control pulse energy (where applicable) may be used to characterise the switches and to gauge their practicality and applicability. In Chapter 3, a review of the current optical switching architectures is presented. Subsequently, the above criteria are used to select the most likely candidate for the all-optical recirculating fibre loop buffer.

In chapter 4, a mathematical analysis of wave propagation in optical fibre is presented along with the origins of the factors that contribute to performance deterioration within the WDM and OTDM systems. This information is presented as a precursor to the beam propagation method (BPM), and is deemed critical for a thorough understanding of the algorithm. The BPM is employed throughout this work to numerically model the propagation of light within optical fibre. The evolutionary properties of propagating soliton pulses and their use in communication based systems are also discussed in this chapter.

The passive recirculating fibre loop buffer is the focus of Chapter 5. First, the uncomplicated architecture, which is based on a fibre loop and a switching mechanism that is initially assumed ideal, is presented. Subsequently, the BER performance of an OTDM system model employing such a buffer is investigated using both computer simulations and an extended mathematical model. The performance of the buffer is also investigated for different incident pulse shapes, namely soliton and Gaussian-soliton, bit rates and fibre types. Finally, the performance after the inclusion of insertion and crosstalk switch losses are considered.

In Chapter 6, the passive recirculating fibre loop buffer model is extended to include an active element. A mathematical model for the resulting active device, which considers the noise sources associated with both the buffer and receiver, is also presented. The BER performance is investigated as a function of delay (i.e. number of loop traversals), amplification period and fibre type. Additionally, the effect of amplifier noise, switch losses and optical filtering on the buffer performance are also investigated. In each instance, the amplifier model is assumed to be generic with a linear gain.

Chapter 7 investigates the performance of the recirculating fibre loop buffer, which employs a symmetric Mach Zehnder (SMZ) to provide the gain and switching functions. As the SMZ critically relies on the properties of the non-linear amplification element, the operation principle and mathematical model of the semiconductor optical amplifier (SOA) are presented first. Subsequently, two novel modes of operation for the SMZ are presented and mathematically modelled, highlighting the gain-switching and

crosstalk properties of each operational mode. It is envisioned that the application of such a switch will have wide implications especially in the optical broadcast networks. Simulation results, based on the mathematical model, show the successful implementation of the buffer and highlight the far reaching benefits of buffers employing this switching technique. Eye diagrams, which indicate the performance of the architecture, are also presented.

Finally, conclusions and suggestions for further works are discussed in Chapter 8.

1.2 Aims and Objectives

The fundamental aim of the work presented in this thesis is to design, model and investigate the performance of an all-optical recirculating fibre loop buffer suitable for use within OTDM systems. In order to achieve this aim the following research milestones were identified:

- Design and simulate the use of a simple passive recirculating fibre loop buffer within an OTDM system, and develop a mathematical model that characterises its BER performance.

- Investigate the characteristics of the passive optical fibre loop buffer against several system parameters such as bit rate, pulse shape, delay, and fibre type.

- Extend the work on the passive version of the device to form a simple active recirculating fibre loop buffer and investigate its BER performance. Furthermore, to develop a new mathematical model which characterises this performance.

- Investigate the characteristics of the active optical loop fibre buffer against several system parameters such as bit rate, fibre type, delay, and amplification period.

- Design, simulate and mathematically model a more realistic version of the active all-optical buffer, which incorporates a practical switching component. Moreover, to investigate its performance with respect to two novel operational modes.

1.3 Original Contributions

During this work the following original contributions have been made:

- Generally within the literature, either Gaussian or hyperbolic secant profiled data pulses are employed for the transmission of OTDM signals within a communication system. In this work the use of Gaussian-soliton pulses is considered for the first time. The communication system and its BER characterisation is realised by simulation using a combination of MATLAB and VPI software packages. (Sections 5.3 and 5.4)

- Development of an analytical expression for determining the BER of a passive recirculating fibre loop buffer as a function of the packet delay (i.e. loop number). Such an expression is absent from the literature. (Section 5.4.2)

- Development of an analytical expression for determining the BER of an active recirculating fibre loop buffer as a function of the packet delay (i.e. loop number). Such an expression is absent from the literature. (Section 6.5)

- The influence of the physical characteristics of the switch on pulse propagation dynamics within RFLBs was detailed for the first time. More specifically, simulations using the VPI software package facilitated the investigation on the effects of switch loss on peak power fluctuations. This is crucial as the peak power of the data pulses is associated with their stability and by extension achievable the BER. (Section 6.6)

- Two novel modes of operation for the SMZ were designed and their associated mathematical models were developed. These modes, refereed to as the joint- and independent- modes of operation do not rely on relative a π-phase difference between the arms of the SMZ device to effect switching and are simulated using the VPI software package. (Sections 7.3 and 7.4)

- Optimisation of the recirculating fibre loop buffer employing the SMZ switch, employing the independent mode of operation, to eliminate the inter-packet crosstalk is investigated using simulations. (Section 7.5)

1.4 Publications

The work in this thesis has resulted in the following publications, which are listed in reverse chronological order.

- A. Als, and Z. Ghassemlooy, "Bit Error Rate Analysis of an All-Optical Buffer Employed in a Soliton Based Optical Time Division Multiplexed Transmission System", *Optics Communications*, Elsevier, Vol. 238, Issue 4-6, August 2004, pp. 281-290.

- A. Als, R. Ngah, Z. Ghassemlooy, G. Swift and J. Chi," Simulation of an All-Optical Recirculating Fiber Loop Buffer Employing a Symmetric Mach-Zehnder (SMZ) Switch," *Proceedings of 7th World Multiconference on Systemics, Cybernetics and Informatics* (CDROM), SCI 2003, Orlando, USA, July 2003.

- A. Als, Z. Ghassemlooy, P. Ball, G. Swift, P. Ball and J. Chi, "Performance of the Passive Recirculating Fiber Loop Buffer within an OTDM Transmission Link", *Optics Communications*, Elsevier, Vol. 209, Issue 1-3, August 2002, pp. 137-147.

- A. Als, Z. Ghassemlooy, G. Swift, P. Ball and J. Chi, "Simulation of Recirculating Fibre Loop Buffers", *Proceedings of 3rd International Symposium on Communication Systems, Networks and Digital Signal Processing*, CSNDSP 2002, Staffordshire University, UK, 2002, pp. 208-211

- A. Als, Z. Ghassemlooy, P. Ball, G. Swift, P. Ball and J. Chi, "All-Optical Packet Buffering for OTDM Networks", *Proceedings of Postgraduate Networking Conference*, PGNET 2002, Liverpool, UK., 2002, pp. 215-220

- A. Als, Z. Ghassemlooy, P. Ball, and J. Chi, "Ultrafast High-Speed Networks: Beyond 2002", Set for Britain House of Commons Poster Presentation, London, UK., March 2002

- A. Als, Z. Ghassemlooy, G. Swift, P. Ball, and J. Chi, "Simulation of the Passive Recirculating Fibre Loop Buffer", *Proceedings of SPIE International Symposium on Information Technologies and Communications, ITCOM* 2001, USA, 2001, pp. 500-509

- R. Gao, A. Als, Z. Ghassemlooy, G. Swift, and P. Ball, "Simulated Error Performance of an All Optical Time Division Multiplexed System", *Proceedings of Postgraduate Networking Conference*, PGNET 2001, Liverpool, UK, pp. 171-176

Chapter 2

Literature Review – The History of Communication Networks and Future Methodologies

2.1 Introduction

The ultimate goal of the information age is to revolutionise the way data is accessed. An important objective is to provide end users with total access to information network resources (e.g. Internet), from any location and in real time [1]. Indeed, this is already becoming a reality with some mobile phone operators employing 3G technologies to make email, photo-messaging and video conferencing services available to their customers. These developments are the latest tools employed both by company employees to maintain their competitive edge and by individuals for personal use. In this chapter, the history of communication networks is traced from the computer era to its current position. In addition, the current trends are extrapolated to forecast the trends that will emerge in the near future. In section 2.2, the progression from circuit switched to message and packet switched networks in the electrical domain is discussed. Thereafter, the transition to optical networks is justified. The bandwidth utilisation schemes, namely wavelength division multiplexing (WDM) and optical time division multiplexing (OTDM) and their associated technological issues will be presented in sections 2.3 and 2.4, respectively. In section 2.5, a brief discussion on the current state

of these multiplexing technologies is presented. Second generation transparent optical networks (TONS) and third generation all-optical networks (AONS) are then introduced in section 2.6. Finally, the chapter concludes with a summary in section 2.7.

2.2 Network Switching Strategies

2.2.1 Circuit switching

In a circuit switched network, a dedicated link is established between the communication parties before any transfer of information occurs. As illustrated in Figure 2.1, the link (nodes A, D, E, G and H) may extend over many communicating (router) nodes and networks. Moreover, the link may also include satellite and microwave components and is maintained for the entire length of the communication process. The inherent advantages of such a strategy include, data format (voice, fax, etc), bit rate, and framing transparency. Additionally, once the initial communications path is established there is no need for complex routing decisions.

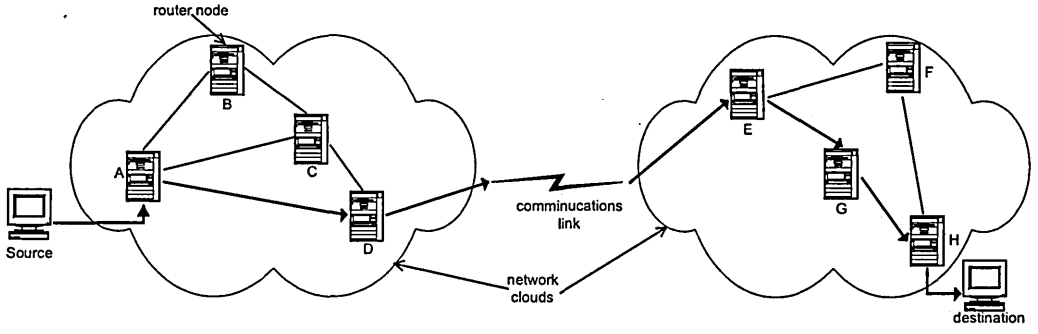

Figure 2.1 Schematic of an arbitrary network topology

The exclusive link setup between the two communicating parties means that congestion does not occur, as all the required bandwidth is reserved in advance. A serious drawback of this method is that periods of available bandwidth are not fully utilised.

2.2.2 Message switching

Message switching presents an alternative strategy whereby no physical link between the communicating parties occurs prior to information transfer. Instead, this method operates on a store-and-forward premise. Entire blocks of data, which have no determinate size limitation, are sent from the source to destination node via intermediate nodes. Each intermediate node has the responsibility for storing, error- checking and then forwarding the blocks that it receives. This mode of operation reduces the initial communication overhead time, as no acknowledgement is required from the receiving party before the information is sent, and is well suited for connection-less oriented systems. However, as there is no limit on the block size each node must have sufficient buffer capability to store very large blocks of data. Moreover, large blocks of data may result in an increased monopoly of the inter-node links rendering message switching useless for dynamic traffic routing scenarios [2].

2.2.3 Packet switching

Packet switching improves the overall system throughput by increasing the link utilisation efficiency. This is achieved by separating large message blocks into smaller entities called packets and routing them independently between the source-destination pair. This ensures that no packet can monopolise an inter-node link for an extended period. Moreover, subsequent packets are transmitted in quick succession, reducing any delays.

As the packets are routed independently, it is possible that they may not arrive in the same chronological order that they were transmitted, and a reordering mechanism must then be employed at the receiver. This is further compounded by the fact that error checking is performed on a point-to-point basis as opposed to end-to-end as in the

circuit switching strategies. However, independent routing has the inherent advantage that single link failures do not necessarily terminate communications between communicating parties, as other paths to the destination may exists (see Figure 2.1). The major disadvantage in packet switching is that large surges in the traffic dynamic may result in packets being dropped at the nodes.

Each of the above switching strategies was developed to meet the specialised requirements of a particular information service. For example, circuit switching was employed in plain old telephone service (POTS) as it was suitable for voice services. Electronic data transfer applications were realised by employing a packet switched data network service (PSDN) [1]. However, transmission speeds were limited to 9600 baud due to the relatively small bandwidths. Services such as the original community antenna television (CATV), were developed to provide larger bandwidths capable of transmitting commercial video. However, CATV was unsuitable for high-speed data communications because the information flow was unidirectional. These factors, coupled with the goal of the information age, prompted the development of the broadband integrated service data network (BISDN). This integrated service is capable of handling telephone, high-speed data transfer, video-on-demand, video conferencing, distance learning and future information formats [1], [3-4]. BISDN is employed in many modern asynchronous transfer mode (ATM) networks including local area networks (LANs) and the Internet. It exploits both circuit and packet switching concepts for effective movement of information across the network. More specifically, the virtual circuit model is loosely based on the circuit switching strategy employed in connection oriented service applications such as Telnet. The datagram model resembles the packet switching strategy employed in connectionless oriented service applications such as

email. Note that although the virtual circuit is implemented on packet switching networks, the packets within the message are not routed independently as a logical path is first initiated between the communicating parties. Furthermore, the path is not dedicated and may thus be shared with other virtual circuits connecting any communicating source-destination pair by employing multiplexing techniques to fully exploit the available bandwidth [5].

2.2.4 Plesiochronous digital hierarchical multiplexing

In digital time division multiplexing (TDM) networks a number of tributary rate signals are combined onto a single transmission line. This is achieved by allocating a dedicated time slot to the signals from the lower bit rate sources and multiplexing them in a rotating repeating sequence (i.e. round robin fashion) onto a high bit-rate transmission line. North America, Japan and the International Telecommunications Union – Telecommunications sector (ITU-T) has developed a suite of standard protocols that are based on multiplexing a number of voice channels sampled at a rate of 8 kHz [1]. The basic multiplex grouping used by both the North America and Japan standard is 24 voice channels whilst that of the ITU-T is 30 resulting in aggregate data rates of 1.544 and 2.048 Mbit/s, respectively. Table 2.1 [5] lists the aggregate bit rates achieved using each of the multiplexing hierarchical schemes.

Table 2.1 Multiplexing hierarchies used in digital transmission systems

	Circuit	Bit rate (Mbit/s)	Voice/Data Channels
North America/Japan	DS1	1.544	24
	DS1C	3.152	48
	DS2	6.312	96
	DS3	44.736	672
	DS4E	139.264	1920
	DS4	274.176	4032
ITU-T	E1	2.048	30
	E2	8.448	120
	E3	34.368	480
	E4	139.264	1920
	E5	565.148	7680

The higher aggregate link bit rates are achieved by multiplexing together the lower bit rate lines with additional bits provided for framing and control purposes. Note the scheme is termed a plesiochronous digital hierarchy (PDH) as each lower bit rate stream has its own clock source. In this scheme, the multiplexed output bit rate is slightly higher than the sum of the combined lower input bit rates. Any unused bit slots are then filled with justification bits.

2.2.5 SDH/SONET

Electrical signals travelling within relatively short lengths (<200m) of coaxial cables are capable of accommodating relatively high (100+ Mbit/s) data rates [3]. However, optical fibre is becoming more popular as they have low absorption and dispersion coefficients. The fibre loss is at a minimum of ~0.6 dB/km and ~0.2 dB/km in the wavelength ranges ~1.3 to ~1.4 μm and ~1.5 to ~1.7μm, respectively. It is relatively inexpensive, and not susceptible to electro-magnetic interference, making it relatively

secure to external hacking. Additionally, it has a huge potential bandwidth (25THz). The synchronous digital hierarchy (SDH), produced by Bellcore, and the synchronous optical network (SONET), produced by the CCITT, were primarily developed to exploit the superior high-speed data rates made practical by optical fibre [3]. The basic data rate of these hierarchical digital transmission systems, defined as synchronous transport module level 1 (STM-1), is 155.52 Mbit/s. However, as Table 2.2 [6-7] illustrates, the highest data rate to date is ~40 Gbit/s. Note that in SONET the term synchronous transport system (STS) or optical carrier (OC) is used to define the equivalent STM signal in SDH.

Table 2.2 SDH/SONET multiplexing hierarchies

SONET	SDH	Bit rate (Mbps)
STS-1/OC-1		51.84
STS-3/OC-3	STM-1	155.52
STS-9/OC-9		466.56
STS-12/OC-12	STM-4	622.08
STS-18/OC-18		933.12
STS-24/OC-24		1244.16
STS-36/OC-36		1866.24
STS-48/OC-48	STM-16	2488.32
STS-96/OC-96		4876.64
STS-192/OC-192	STM-64	9953.28
STS-768/OC-768	STM-256	39,814.32

The transition to the optical domain and the provisioning for the ultra high-speed data rates of hundreds of Gigahertz spurred the advancement of both WDM and OTDM technologies. In the following sections the technical issues, challenges and advances of each of these technologies are presented.

2.3 Wavelength Division Multiplexing Technology

The principle operation of WDM is analogous to the frequency division multiplexing (FDM) in the electrical domain. As highlighted in Figure 2.2, optical signals from multiple sources, each at a different wavelength (λ_n), are combined and transmitted simultaneously over a single fibre. By exploiting the wavelength domain to obtain greater transmission bandwidth, it is possible to implement optical networks with many attractive features. Namely the ability to add services or to increase the network capacity without disturbance to existing customers by increasing the number of unique wavelength channels. This process is completely transparent, as each channel may offer any service at any arbitrary bit rate and modulation format. The increase in the number of wavelengths requires that only the end-node terminal equipment needs to be upgraded. However, employing wavelength tuneable devices reduces the need to change the end-node equipment every time another single wavelength is added.

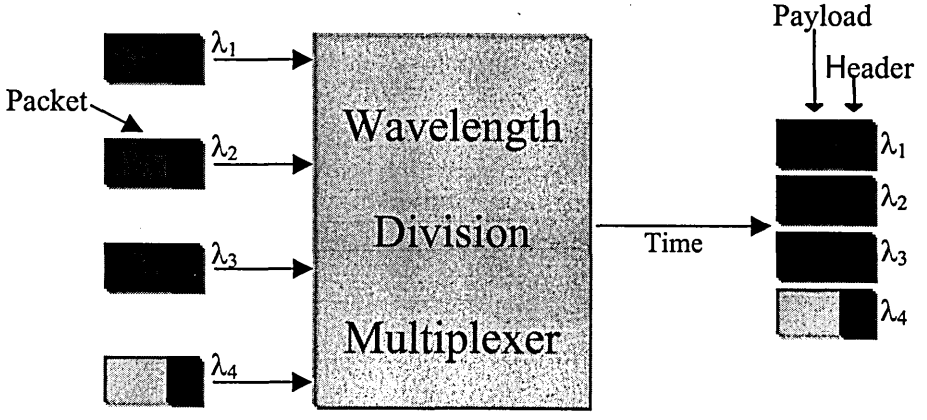

Figure 2.2 WDM operating principle

A significant benefit offered by the WDM technology is that the constituent components have been commercially available for over a decade. Early prototype WDM networks include one developed by the British Telecom Laboratories in December

1990. This simplified network supported telephone services at 1300 nm, with two distributive video services at 1320 and 1340 nm, and a bi-directional dialogue service at 1280 nm [8]. The latter being based on an asynchronous transfer mode passive optical network system dubbed APON. This system operated at 155 Mbit/s with a payload of 140 Mbit/s.

The development of more wavelength stable laser sources resulted in greater exploitation of the 1.3 μm window as more wavelengths could now be added due to the reduction in the crosstalk. A further increase in the network capacity is attributed to shifting the operating wavelength into the third transmission window at 1.5 μm as shown in Figure 2.3. This facilitated the development of dense wavelength division multiplexing (DWDM) where the number of wavelengths per fibre link is greatly enhanced [9]. As a result, basic WDM systems with 40 Gbit/s capacities are now readily available, and test systems with capacities over 1 Tbit/s have been reported [10].

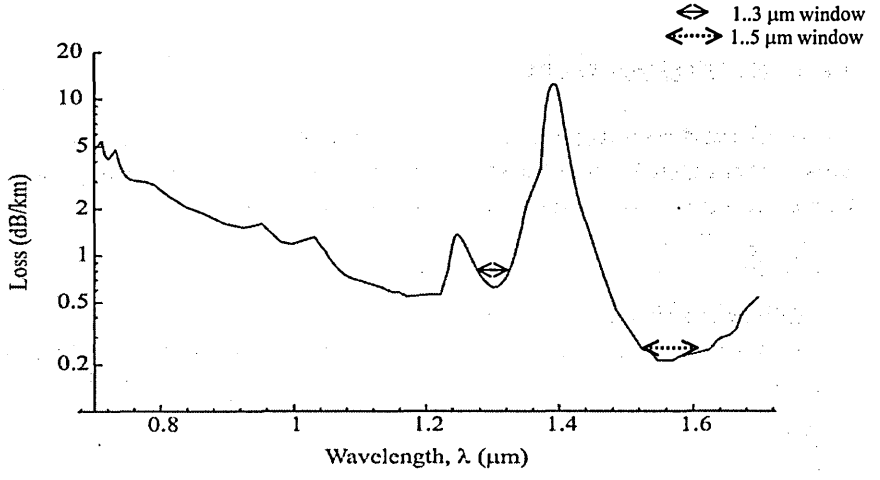

Figure 2.3 Spectral loss profile of optical fibre

In realising these phenomenal ultra-high speed bit rates, WDM has to overcome many obstacles. In particular, continually increasing the number of wavelength channels per

fibre to enhance fibre capacity has a practical limit, as each wavelength channel must be spaced from its neighbour to mitigate against damaging non-linear effects. These effects namely, four-wave mixing (FWM), stimulated Raman scattering (SRS), stimulated Brillouin scattering (SBS) and cross phase modulation (XPM), and methods to reduce their effects will be the subject of the following subsections. The issues of dispersion and self-phase modulation (SPM) that can occur to an extent in WDM will be presented in section 2.4, where the factors that degrade the performance of the OTDM systems are presented.

2.3.1 Four-wave mixing (FWM)

The FWM effect can be described by equation (2.1), which shows three optical fields with different carrier frequencies ω_n co-propagating within the same fibre medium. FWM causes a new composite field to be created from the mixing of these signals. This process is a major source of non-linear crosstalk within WDM systems [10].

$$\omega_{FWM} = \omega_p \pm \omega_q \pm \omega_r \tag{2.1}$$

For a large *M*-Channel WDM system *p, q* and *r* may vary from 1 to *M*, resulting in an abundant combination of new FWM channels. These newly created channels degrade system performance by either coherently interfering with the existing closely spaced data channels or by increasing the background noise thereby reducing the signal-to-noise (SNR) ratio.

2.3.2 Stimulated Raman scattering (SRS)

Stimulated Raman scattering is an inelastic scattering process in which incident (pump) photons are annihilated on propagating through a dielectric fibre medium. A photon at the down shifted Stokes frequency and a phonon with sufficient energy and momentum to maintain that the laws of conservation are created in the process. Note that the SRS process results in optical power losses for the pump signals and the optical phonons created co-propagate with the diminished pump signal. For low signal powers, the power loss is negligible [11]. However, the intensity of the scattered light grows exponentially once the incident power crosses a threshold value, which can be estimated by considering how the scattered light intensity grows from noise [12]. The threshold power P_{th}, defined as the incident power at which half of the power is lost to SRS at the output of the fibre, is given as [11]:

$$P_{th} = 16 A_{eff} / g_R L_{eff}, \tag{2.2}$$

where g_R is the Raman gain coefficient, A_{eff} is the effective fibre core area, and L_{eff} is the effective fibre length given by:

$$L_{eff} = \left(1 - e^{-\alpha L}\right) / \alpha, \tag{2.3}$$

where α and L are the intrinsic fibre loss and length of the fibre, respectively. Using typical fibre characteristics, α_{dB} = 0.2 dB/km and A_{eff} = 50 um^2, then for long lengths of fibre (L_{eff}=1/α), with g_R = 1x10^{-12} m/W, the threshold power is approximately 570 mW near 1.55 μm [11]. This does not represent a significant problem when a single channel, at ~10 mW of power, is propagating down the fibre. However, in WDM applications it places an upper bound on the number of channels allowed as each channel has an

associated incident power. Moreover, the fibre acts as a Raman amplifier whereby the shorter wavelength channels amplify the longer wavelength channels as long as the wavelength difference is within the bandwidth of the Raman gain.

2.3.3 Stimulated Brillouin scattering (SBS)

Stimulated Brillouin scattering is another inelastic scattering process. However, it differs from SRS in two fundamental ways. First, acoustic phonons are produced and second, they propagate contrary to the incident pump pulse. The threshold power for SBS is given by:

$$P_{th} = 21 A_{eff} / g_B L_{eff}, \tag{2.4}$$

where g_B is the Brillouin gain coefficient and the other terms are as defined previously. By using the parameters from the previous subsection and taking $g_B = 5\text{x}10^{-11}$, note that the threshold power is approximately 1 mW near 1.55 μm [11]. This low threshold power makes SBS the more dominant scattering process, severely limiting the input power and repeater spacing in lightwave systems [13-19]. Consequently, techniques that exploit the relationship between the SBS threshold and the spectral width of the incident light are employed to increase the threshold level. These include increasing the source linewidth through phase or frequency modulation [16-17] or alternatively, broadening the Brillouin gain of the fibre by applying a non-uniform Brillouin frequency downshift along the length of the fibre. The downshift may be achieved by either changing core dimension or dopant concentration during the fibre manufacturing process [13], [16], or by producing a strain or a temperature gradient on the transmission fibre. Temperature

distributions within highly non-linear fibre were used by Hansyrd to raise the input power to a possible few hundred milliwatts [15].

2.3.4 Cross phase modulation (XPM)

Cross phase modulation is the non-linear phase shift that occurs when signals of different wavelengths co-propagate within optical fibres and results in asymmetric spectral broadening. In addition to this, the SNR is deteriorated as fibre dispersion converts the phase modulations into amplitude fluctuations. As the phase of each wavelength channel is affected by the average power and the bit pattern of all other channels it limits the total number of channels that can be physically realised. Reducing the number of channels and appropriate wavelength spacing are methods used to reduce the power penalties caused by XPM.

2.4 Optical Time Division Multiplexing Technology

The principle operation of OTDM is analogous to time division multiplexing (TDM) in the electrical domain. As depicted in Figure 2.4, optical signals from multiple sources, each at the same wavelength (λ_1), are time interleaved in a round robin manner and transmitted over a single fibre. The simple N-packet interleaving architecture shown inset in Figure 2.4 consists of a passive N+1 star splitter/combiner pair, N+1 modulators Mod i, i = 1, 2... N+1, and N+1 optical fibres with their lengths adjusted to provide the appropriate delays. The clocking signals that are input to Mod 1 are used as framing pulses for system synchronisation. Both bit- and packet-interleaving OTDM systems are possible with this architecture with minor modifications to the fibre delay lengths and/or bit rate. However, packet-interleaving OTDM provides better throughput efficiency in slotted networks where statistical multiplexing is employed [20].

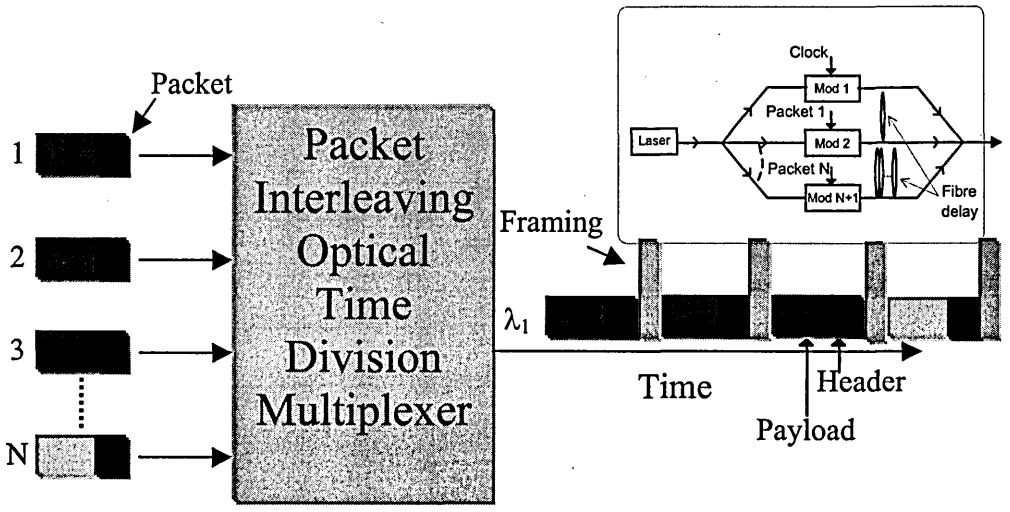

Figure 2.4 OTDM operating principal

The interest in ultra-high bit rate OTDM lightwave systems began in the 1990s when transmission at 1 Tbit/s over a single channel was proposed [11]. Using this technique, many of the performance inhibiting non-linear effects that hindered WDM could be avoided [8]. On of the early demonstrations of OTDM was in 1992, when Mollenauer *et al* successfully used this technique to transmit data at 5 Gbit/s over 15,000 km [21]. Nakazawa *et al* improved the bit rate and achieved penalty-free transmission at 20 Gbit/s over 1020 km in the same year [22]. Research results for full systems first appeared in 1996 [23] and are now commercially available. Today testbeds that demonstrate transmission rates exceeding 100 Gbit/s are now commonplace [20], [24-27]. Indeed, there are cases of 640 Gbit/s and 1 Tbit/s [28-30] reported in the literature. To obtain these ultra-high speed data rates, the traditional non-return-to-zero (NRZ) format that was commonly used in WDM light wave systems was replaced by a return-to-zero (RZ) format [11], [31]. At these rates, the effects of dispersion and self-phase modulation are the dominant performance inhibitors of OTDM. These processes will be considered in the following subsections. Gordon-Haus timing jitter, which is also

responsible for degrading the performance of OTDM amplified lightwave systems will be considered in Chapter 6.

2.4.1 Dispersion

Increasing the bit rate leads to the requirement for narrower pulse widths, which results in a broadening of the spectral profile of the pulses. Each of the frequency components within the profile will propagate along the fibre at a slightly different velocity. The resulting temporal separation of the components is responsible for the distortion observed when transmitted pulses travel an appreciable distance. Dispersion management then becomes necessary when the optical path length extends to tens of kilometres [7]. One solution is to litter the link with opto-electro-optical (OEO) converters to help combat the dispersion. However, this option is not practical for ultra-high speed systems as the converter will be a potential source of bottlenecks. Alternatively, an all-optical approach employing lengths of normal and anomalous dispersion fibre may be used. This technique exploits the inherent nature of the two fibre types in maintaining the pulse profile. Pulses propagating along the normal-fibre experience a medium with a positive first order dispersion parameter (β_2) that broadens the pulses with the increasing distance. In the length of anomalous dispersion fibre, where β_2 is negative, the pulse widths are reduced. Interleaving these two types of fibre, as illustrated in Figure 2.5, then creates an effective dispersion management tool.

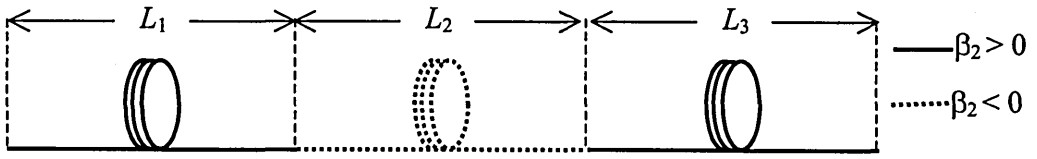

Figure 2.5 A simple dispersion management system

Mid-span spectral inversion (MSSI) presents another dispersion management technique. In this technique, the spectral components of the data pulses are inverted at the halfway point of the optical path link using a FWM technique. The components that were red-shifted during the first half of the propagation path are blue-shifted along the second half, and visa versa. Consequently, the spectrum realigns itself over the second half of the journey and the distortion effectively reverses itself.

2.4.2 Self-phase modulation (SPM)

Self-phase modulation refers to the self-induced phase shift experienced by an optical field as it propagates within an optical fibre. This results in chirping and a spectral broadening of the optical pulses. The magnitude of the SPM phase shift ϕ_{NL}, experienced by an optical carrier with power P, after traversing a length of fibre L, is given as:

$$\phi_{NL} = \gamma.L.P, \tag{2.5}$$

The non-linear coefficient γ is defined as:

$$\gamma = \frac{2\pi n_2}{\lambda A_{eff}}, \tag{2.6}$$

where n_2, λ and A_{eff} are the non-linear refractive index, the wavelength of the optical carrier and the effective fibre core area, respectively. Substituting (2.6) into (2.5) to form (2.7) reveals that the SPM contribution is proportional to the optical intensity I of the pulse and the distance propagated.

$$\phi_{NL} = I.L. \qquad (2.7)$$

Consequently, SPM is particularly damaging on the long haul optical paths. Note that although SPM leads to pulse broadening in normal dispersion fibre, it has the reverse effect in anomalous dispersion fibre. This feature is exploited by the soliton pulses in anomalous fibre, which attempt to balance the compression effect induced by SPM with the broadening effect of dispersion to create a stable pulse profile [32]. Soliton pulses will be described in further detail in chapter 4.

2.5 Further Development of Multiplexed Networks Systems

The practical realisation of OTDM and WDM lightwave systems has allowed data rates to be extended into the terabit region. However, both systems fail to exploit the full bandwidth of optical fibre. Recent advances have combined both OTDM and WDM technologies to provide even greater link capacities. More specifically, each wavelength channel within a WDM transmission links may contain OTDM signals. Zhu *et al* successfully transmitted 3.08 Tbit/s over 1200 km. In that work, each of the 77 WDM channels contained OTDM multiplexed channels with an aggregate data rate of 42.7 Gbit/s [33-34].

Nuss *et al* demonstrated that the number of wavelength channels could also be increased to 206 by employing a technique referred to as the chirped-pulse WDM. Essentially, femto-second pulses are chirped by passing them through dispersive fibre and then

modulating them using a high-speed modulator [35-36]. In [37] the same authors suggest that the number of individual wavelength channels may be increased from approximately 300 to 1021 using spectral slicing. Each of these channels may then be time division multiplexed. However, in their experiment, only 110 WDM channels were used and each was time division multiplexed at 2.35 Gbit/s to yield an aggregate data rate of ~258 Gbit/s. This highlights the enormous potential of future systems.

With the development of coded division multiple access schemes [38], and the generation of optical pulses as short as 4.5 ps [37], the possibility of even higher data rates is a reality.

2.6 Optical Network Infrastructures

The first generation optical networks needed O-E-O regenerator stations at strategic positions along the fibre link to maintain the data integrity. Contention resolution, packet loading and unloading within such networks were implemented at the electrical stage of the re-generation process. With the advent of lithium niobate ($LiNbO_3$) modulators and the erbium doped fibre amplifier (EDFA), second generation transparent optical networks (TONs) were developed, and the data signals remained in the optical domain over the complete transmission path. However, as the control and routing mechanisms were essentially electrical, packet loading and unloading was still relatively easy. Network topologies that are based on the TONs concept include the Shufflenet and Manhattan Street Network [7], [39-41].

Third generation optical networks are commonly referred to as all-optical networks (AONs) as both the data signals and control signals are optical. AONs were developed

specifically to accommodate transmission at the ultra-high data rates offered by modern OTDM and WDM technologies. With WDM being a mature technology, issues surrounding synchronisation, routing and buffering are relatively straight forward as each channel is assigned a unique wavelength. However, corresponding OTDM functions are handicapped by strict timing constraints making these tasks non-trivial. Synchronisation may be achieved by recognising and extracting the framing (clock) pulses [42]. The extracted clock can then used for header recognition and by extension, self- routing [43-49].

In the next chapter, interferometric switching architectures that are capable of performing clock extraction are presented. Moreover, all-optical router employing such switches is found in Appendix A.

2.7 Summary

In this chapter, a historical review of optical networks was presented, tracing their origins from the electrical counterparts. The evolution from first- to second- and third generation optical networks was chronicled. Finally, a technical review of the issues and challenges surrounding the WDM and OTDM technologies were discussed giving insights as to their foreseeable futures.

A critical review of the current switching architecture technologies is presented in the next chapter. This review is then employed to identify the optimal switch architecture for use within the RFLB.

Chapter 3

Review of Optical Switching Architectures

3.1 Introduction

The growth of the Internet and the associated surge in multimedia traffic has necessitated the transformation from electrical to optical network infrastructures that are capable of realising future bandwidth on demand (BOD) requirements. The second generation transparent optical networks (TONs) are systematically being replaced by the third generation all-optical networks in an effort to increase the communication throughput efficiency. Recall that in TONs, the data signals remain in the optical domain for the complete communications path between the source and destination nodes. However, the electro-optic switches employed by the routers limit the speed of these networks to tens of gigahertz [11]. This bottleneck is avoided in AONs where both the data signals and routing control mechanisms exist solely in the optical domain. The all-optical switches employed in these networks are well well-matched for operations in the order of 100 GHz or more [10]. In addition, their switching action enables them to be easily employed as either single-bit demultiplexers, or packet switches, with only minor architectural or operational modifications. The functional role of the all-optical switch has also been extended beyond demultiplexers and packet switches to all-optical devices such as the Boolean gates [50-55], wavelength converters [56-58], filters [11], [59], equalisers [60], regenerative memories [61-63] and routers [43;45;64;65;65;66]. In

this chapter, a number of existing optical switching architectures are presented. More specifically, the Mach Zehnder Interferometer (MZI) and some of its derivatives, the non-linear optical loop mirror (NOLM), terahertz optical asymmetric demultiplexer (TOAD), the symmetrical Mach Zehnder (SMZ) and colliding-pulse Mach Zehnder (CPMZ) interferometers. In addition, the ultra-fast non-linear interferometer (UNI) and the non-linear waveguide (NLWG) switch are highlighted along with emerging switching technologies such as those employing micro-electro-mechanical systems (MEMS), bubble technology, liquid crystals and holograms. A comparative study will be employed to select the optimal switch configuration to be integrated firstly within an all-optical router and secondly, within the buffering architecture presented in Chapter 7.

3.2 Switching Architectures

In this section, a review of the optical switches highlighted previously is presented. The MZI and NOLM architectures are presented in subsections 3.2.1 and 3.2.2, respectively. Also in subsection 3.2.2, the semiconductor laser amplifier loop mirror (SLALOM) is introduced as a precursor to the TOAD architecture and its derivative, the SMZ that are presented in subsections 3.2.3 and 3.2.4, respectively. The UNI and the NLWG architectures are described in subsections 3.2.5 and 3.2.6, respectively. Finally, some of the emerging switching architectures are highlighted in subsection 3.2.7.

3.2.1 The Mach Zehnder interferometer (MZI)

The MZI, shown in Figure 3.1, has long been established as a mature switching technology. The device uses the relative phase difference between the data signals travelling along two waveguide paths to achieve a switching action. A common configuration uses lithium niobate ($LiNbO_3$) for the waveguides. In the absence of an external voltage, the data signals entering the device are divided into two identical copies after the first 50:50 3-dB coupler (C_1).

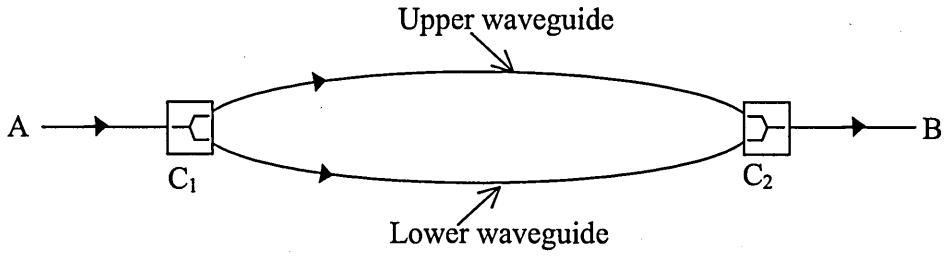

Figure 3.1 - Schematic of a simple MZI configuration

As signals traverse the upper and lower waveguides, they experience identical phase shifts and interfere constructively at the output (B). An external voltage applied to one of the waveguides induces a refractive index change, which results in a relative phase difference between the two paths. For a particular voltage, where a relative phase difference of π is generated, the interference at the second 3-dB coupler (C_2) becomes destructive. Note that although the $LiNbO_3$ MZI modulator is electro-optic, but it is capable of operating at speeds up to 20 Gbit/s [11]. A variation of this concept is observed in the thermo-optic switches where the variation of the refractive index of the dielectric material results from varying the temperature of the material itself. In this case, one arm of the MZI is saddled with a heating electrode.

3.2.2 Non-linear optical loop mirror (NOLM)

Figure 3.2 illustrates the NOLM architecture which is constructed from a 2x2 3-dB coupler (C_1) and a long loop of mono-mode fibre that is formed by connecting the two ends of the fibre to ports 'C' and 'D' of C_1. An additional 3-dB coupler (C_2) is placed within the loop to enable the input of a control pulse. This device relies on the weak interaction between the control pulse and the data signal as they co-propagate the loop to produce the switching action.

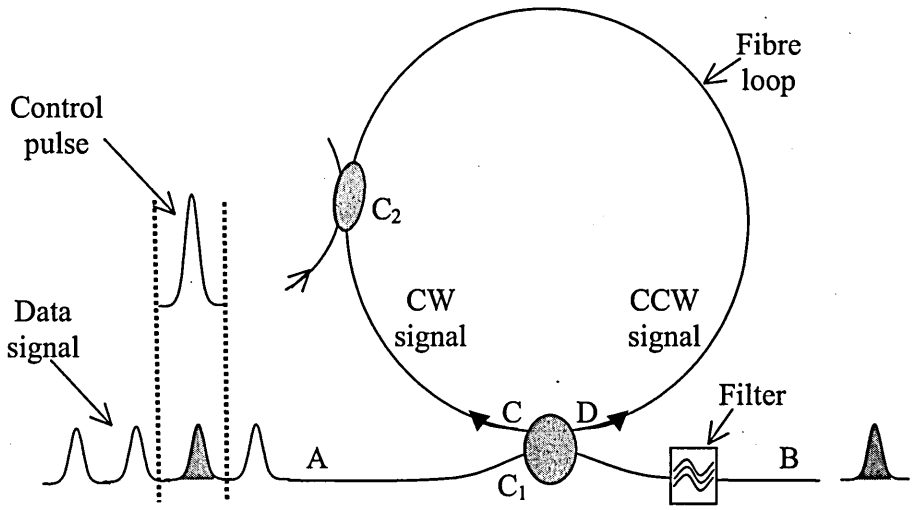

Figure 3.2 - Schematic of the NOLM architecture

The operation is very similar in principle to the MZI, in that data entering the loop via port A is split at C_1 into two identical streams that counter-propagate the loop. In the absence of a control pulse at C_2, both data streams encounter the same medium conditions and therefore experience the same phase change. Consequently, on recombining at C_1 the pulses interfere constructively and exit via the input branch. Conversely, when a control pulse is suitably aligned with a given co-propagating (CW) pulse within the stream, XPM causes the phase of that pulse to continually change over the length of the loop mirror. As this action is not replicated within the associated

counter-propagating (CCW) pulse, a relative phase change is produced. Depending on the relative phase shift, a portion of the data pulse intensity is transmitted to the output port (B) on recombining at the coupler. A relative phase difference of π generated between the counter-propagating pulses ensures that the entire pulse (intensity) is transmitted to the output port (B). An optical band-pass filter is then employed to prevent the control pulse from propagating with the switched data signals. Note that as all the remaining pulses experience the same medium, they are completely reflected to the input port (A).

The NOLM relies solely on the intensity dependent non-linearity produced within the fibre loop. Consequently, a long length of fibre L (100m < L < ~1 km) [44], [67] is needed to produce a π phase difference. The introduction of a semiconductor optical amplifier (SOA) within the loop architecture, as shown in Figure 3.3, eliminates the need for such lengthy loop mirrors as the phase change now depends on the non-linearity within the SOA. The principle operation of this device, called the semiconductor laser amplifier in a loop mirror (SLALOM), is not dissimilar to the NOLM. The clockwise signal reaches the SOA first and is amplified by its gain profile ($g_{cw}(t_1)$). At time T seconds later, the counter-clockwise signal arriving at the SOA experiences a different gain profile ($g_{ccw}(t_2)$), which depends on the saturation of the amplifier caused by the previous signals and the gain recovery characteristics of the device. Having traversed the loop, the counter-propagating signals are superimposed and the ensuing interference determines the output port destination of the signals. More specifically, if the $g_{cw}(t_1) = g_{ccw}(t_2)$ then the injected signal will be totally reflected to the input port. This occurs when the eccentricity of the SOA within the loop (Δx) is small. Note that in addition to the relative phase difference between the counter propagating pulses this device is also affected by the relative gain to produce the desired switching

action. Although the rising edge of the temporal switching window is only a few picoseconds, the falling edge is dependent on the gain recovery time of the SLA (>100ps) [68]. In the next subsection we consider an architectural innovation, which builds on the strengths of the NOLM and SLALOM. It combines the use of a control

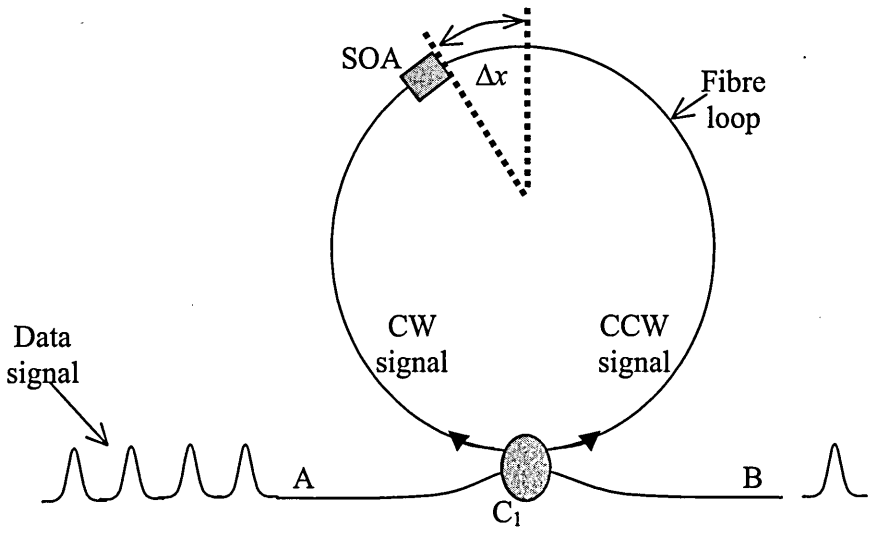

Figure 3.3 - Schematic of the SLALOM configuration

pulse, to effect switching, with a change in the asymmetry of the SOA within the loop, to limit the influence of the gain recovery on the falling edge of the temporal switching window.

3.2.3 Terahertz optical asymmetric demultiplexer (TOAD)

The TOAD is an interferometric switch that uses an active non-linear element (NLE), such as a SOA, to produce a phase change in the signals to be switched. Figure 3.4 shows the basic configuration of the TOAD. The major differences between this architecture and the SLALOM lie in the introduction of a control pulse and the eccentricity of the NLE. Whereas the SLALOM in [68] was used to investigate the optimisation of contrast ratios, the TOAD was specifically designed to enhance ultra-fast switching capabilities [69].

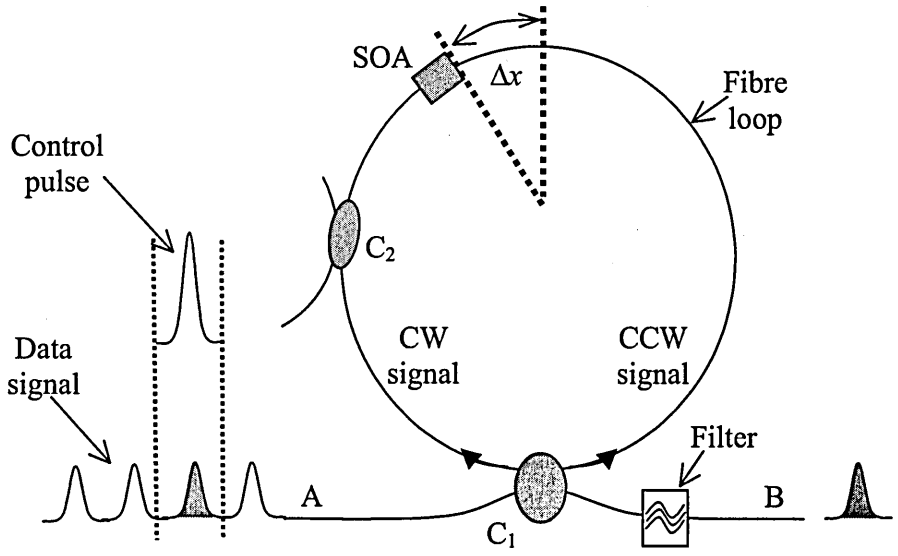

Figure 3.4 - Schematic of the TOAD configuration

In the absence of a control pulse, injected data signals are split into two signals of equal intensity by the 50:50 3-dB coupler (C_1). The counter-propagating signals enter the SOA at two different instances of time, determined by the difference in path length Δx, and then recombine interferometrically at the C_1. Assuming that the intensity of the data signals is insufficient to cause saturation, then both the clockwise (CW) and counter-clockwise (CCW) components experience the same attenuation and phase shift as they propagate within the fibre loop. On recombining at C_1 the data signals are reflected to the input port (A). When a suitable aligned control pulse is injected into the loop, the device operates in a manner very similar to the SLALOM. More specifically, the control pulse, which arrives at the SLA just prior to the CW propagating data signals, causes the SLA to saturate. The associated gain and refractive index change results in the counter-propagating signals experiencing different gain and phase shifts as they traverse the SOA. This differential gain and phase shift is responsible for the switching action of the TOAD. Under ideal conditions, a π-radian phase shift produces complete switching of

the intended data signal(s) at the output port of the device. The temporal duration of the switching window is given as [67]:

$$\tau_{win} = \frac{2\Delta x\, n}{c}, \tag{3.1}$$

where c is speed of light in a vacuum, n is the refractive index of the fibre and Δx is the offset of the SOA from the centre of the loop. Only data pulses that co-propagate with and travel just behind the control pulse by up to twice the optical path length of the SOA offset are effectively switched to the output port. The filter at the output port prevents the control pulse from propagating with the data. Equation (3.1) highlights that the switching window duration can be adjusted by varying the asymmetry of the SOA within the loop. This feature is exploited in the TOAD router presented in Appendix A.

3.2.4 Symmetric Mach-Zehnder (SMZ)

The SMZ is an architectural innovation of the TOAD switch and closely resembles the original MZI configuration. As illustrated in Figure 3.5, this interferometric switch employs a SOA in each arm of the device [70].

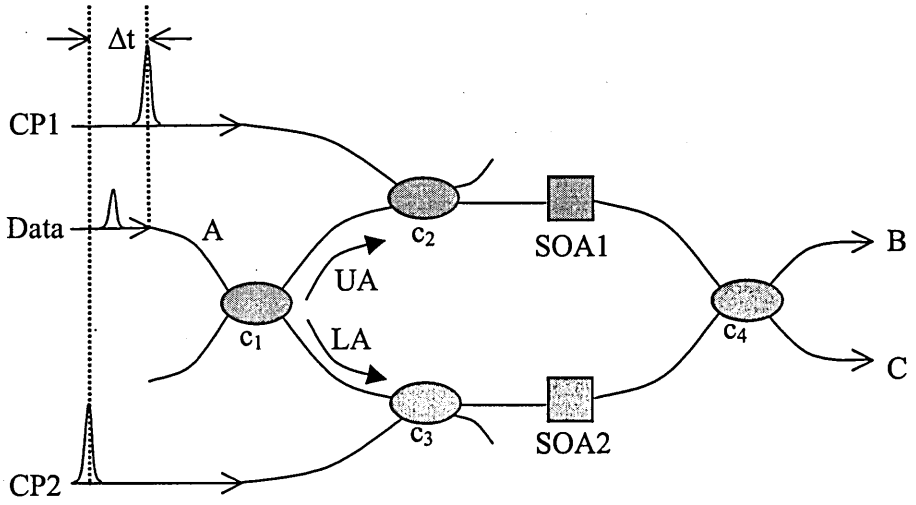

Figure 3.5 Schematic of the Symmetric Mach-Zehnder (SMZ) switch

The operating of the device is similar in principle to the switches considered in the previous sections. However, in this device two control pulses co-propagate with the data signals to produce the switching action. When the control pulses are injected into the device, a differential phase shift caused by carrier depletion in the SOA is generated between the two arms of the interferometer. Consequently, data signals may be switched to output port B. As with the TOAD, data pulses following the control pulse pass through the switch during the recovery period of the SLA are switched to output port C. The control signals are removed from the data using an optical filter. Assuming that each SOA is in the same relative position within the interferometer, the temporal duration of the switching window τ_{win} is determined by the relative time difference between the two control pulses (Δt) prior to entering the interferometer such that $\tau_{win} \approx \Delta t$. In the absence of control pulses, the SMZ is characterised as "balanced" as the data pulses traversing both arms of the device experience the same medium conditions. On recombining at C_4, the data pulses emerge from the output port B.

The colliding-pulse Mach-Zehnder (CPMZ), shown in Figure 3.6, is a small variation of the SMZ.

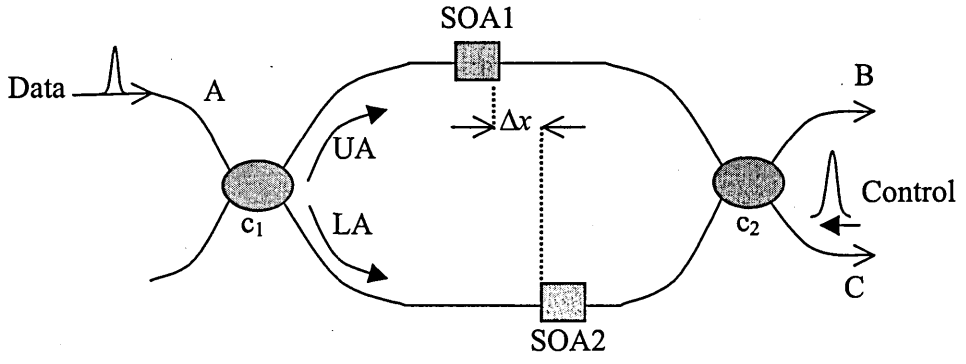

Figure 3.6 Schematic of colliding pulse Mach-Zehnder (CPMZ) switch architecture

In this derivative the control pulses counter-propagate with the data signals inside the interferometer. As a result the control pulses can be injected into the interferometer without additional coupling losses and no optical filter is required to reject the control pulses. In principle, the CPMZ operates identically to the TOAD and it achieves the same temporal switching window width as given by Equation (3.1). However, the minimum switching window is constrained by the length of the SOA in both devices [71]. Note the CPMZ may require temperature stabilisation as the data signals travel along separate waveguides in this device.

3.2.5 Ultra-fast non-linear interferometer (UNI)

The UNI, shown in Figure 3.7, is a single arm interferometer, which uses an SOA as the NLE to implement switching. A long length of birefringent fibre is used to temporally separate orthogonally polarised components of the data pulses. This birefringent property arises in fibres that are not perfectly circularly symmetric, thus allowing the propagation of two orthogonally polarised modes, each having a different propagation constant.

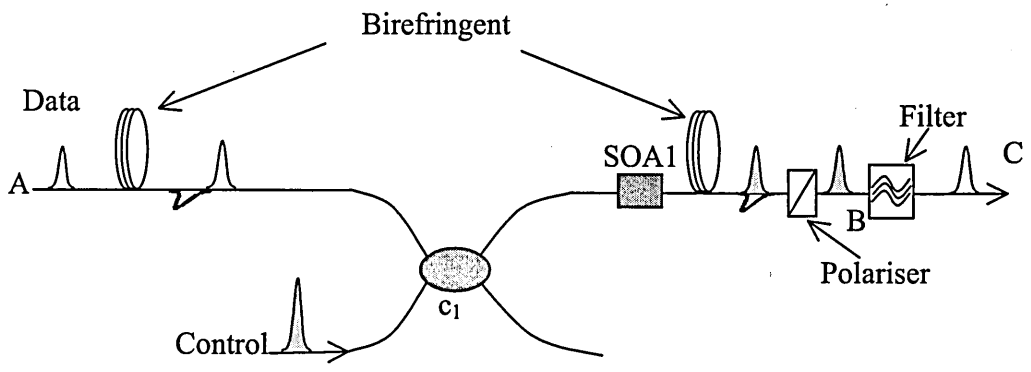

Figure 3.7 Schematic of the UNI architecture

A suitably aligned control pulse is then introduced between the data pulse components to be switched. After traversing the SOA, only the data pulses that are separated by the control pulse experience a differential phase change. Consequently, when the data pulses are realigned (by using another length of birefringent fibre) they interfere and only the data pulses that have experienced the differential phase shift are switched out to the polariser located at port B [72].

3.2.6 Non-linear waveguide (NLWG) switch

The NLWG switch uses a Mach-Zehnder configuration with passive semiconductor material for the waveguides offset within each arm. This approach is very similar to the SMZ with the exception that the switching action is accomplished via passive means. For this reason the device is loosely described as a passive-TOAD [73]. The operating principle is based on the data and control pulses being sufficiently separated in wavelength to produce a band filling effect within the waveguide. Essentially, when a control pulse with the required wavelength is introduced to the device it is absorbed by the NLWG creating an instantaneous change in the refractive index of the semiconductor material. Subsequent data pulses entering the switch then experience a differential phase change, which is responsible for the switching action. The control pulse is then separated from the switched output by a wavelength selective optical band-pass filter.

3.2.7 Emerging optical switching alternatives

In this section, alternative optical switching techniques that are currently being considered commercially are presented.

Presently, the leading technology manufacturers are designing circuit switches that employ micro-electro-mechanical systems (MEMS) switching fabrics. These switches use electrostatic or magnetic forces to adjust the positions of tiny pivoted mirrors whose diameters are no larger than the human hair. In essence, optical pulses from an input fibre are incident to a mirror, which is directed to move the light onto another mirror on a facing array. This mirror than reflects the optical pulses to the desired output fibre [74-75]. Complex fabrics are available in which the directing mirrors have two degrees of freedom thereby making a three dimensional architecture realisable [76]. MEMS architectures offer the advantages of protocol transparency, low power consumption, low loss, compact size good scalability and the data signals remain in the optical domain. However, because the switching mechanism is inherently mechanical, they are generally slow to reconfigure (10 ms) [77] and are thus unsuitable for switching packets as in IP routing. MEMS based switches are thought to be best suited for use by interconnect service providers where large continuous streams of traffic are maintained for extensive periods of time between fixed locations. Lucent pioneered this field by establishing their Lambda Router which has port dimensions of 256×256 and is capable of supporting single data rates as high as 40 Gb/s [78-79].

Lucent's sister company, Agilent, has pioneered an optical switching device that is based on mature ink-jet and planar lightwave circuit technology [80]. The switching fabric is made of a horizontal and vertical array of permanently aligned waveguides. Optical pulses traverse horizontal light paths from the input to the output port unless a switching operation has occurred. In that case, a bubble is created at the intersection of the desired waveguide and the information is reflected down the vertical path to the switched port. Bubble technology switches share all the desirable attributes of MEMS

type switches and have the added advantage of no movable parts. Consequently, they are perceived as more durable. The disadvantages centre around the latency required for the bubble creation and annihilation processes (≈5 ms) [81]. As both the bubble and MEMS switching technology have relatively long switching latencies, they compete for the same target applications.

Liquid-crystals may be used in conjunction with polarisation-dependent materials which absorb or reflect light with a specific polarisation to make liquid-crystal switches [82]. This technology exploits an inherent property of the liquid crystal material to produce the switching action. In the liquid-crystal phase, molecules align themselves in accordance with their permanent electrical dipole moment. When a voltage is applied across the liquid-crystal the orientation of the molecules, and hence the optical properties of the material, are altered. Consequently, the development of a simple on/off switch can be easily realised.

The advantages of employing liquid crystals are that the technology is well developed and reliable. However, the switching action is slow (especially at low temperatures), and it is generally difficult to integrate with other optical components. Additionally, there are high losses from the liquid crystal itself and it is difficult to implement, as the polarisation of the input pulse is completely uncontrolled. Note however that an innovation proposed by Digilens Inc. [83] combined liquid-crystals with polymers to form small sized 1×2 electro-optic switches.

Electro-holographic switches are the newest optical switching technology used in WDM applications. A solid-state switch matrix is created form rows and columns of

ferroelectric crystals. Essentially the switching action is based on the ability to control the reconstruction process of (volume) holograms using an electric field [84]. In the absence of an applied voltage, the crystal is transparent and optical pulses pass straight through. Conversely, using a suitable driving voltage, the optical pulses crossing the crystal are deflected. By exploiting this phenomenon, it is possible to adjust the light path of the optical pulses traversing the array to perform switching. The main advantage of this technology is that each crystal may store several holograms making it possible to drop single wavelengths, or groups of wavelengths from a WDM signal. Additionally, they are very fast and consume negligible power. However, increasing the switching matrix size requires the addition of more specialised components e.g. devices for collimating and focussing the beams. Consequently, these devices don't scale well. In addition, the non-energised blocks in the optical path will contribute to loss and cross-talk of the switch. Dispersion and polarisation-dependent losses occur also as the light signals travel through the crystals.

3.3 Comparison of Switching Architectures

This section presents a critique of the previously described switching methodologies. More importantly, the optimal switching technologies for the buffering and routing devices presented in Chapter 7 and Appendix A, respectively, are highlighted. Here, the switching mechanisms are considered for an OTDM system, and have to be transparent to the protocol used, require low power, and capable of operating at ultra-fast data rates with high repetition rates. In addition, they must be reliable and be capable of integration into other optical devices.

Among the emerging switching technologies highlighted in section 3.2.7 MEMS have emerged as the most popular choice within industry [85]. This is due to their precision, simplicity, small size and low manufacturing cost in high volume. In addition, they exhibit exceptional optical performance with a high reflection coefficient leading to low loss and cross-talk. Unfortunately, these opto-mechanical devices are slow, taking milliseconds to switch, require moving parts and have a limited scalability. The bubble switches considered have the added advantage of having no movable parts but again the switching process is still slow. Moreover, scalability is limited to about 100 ports because of the loss and cross-talk at each intersection. The liquid-crystal switches are reliable and well characterised but are slow and difficult to integrate with other optical technologies. The high losses experienced by the optical pulses as they traverse the medium prohibit its uses for packet switching. Electro-holographic switches are very promising especially for WDM technology despite their limited scalability. They are fast and consume negligible amounts of power, however because of their limited scalability they are not considered. In summary, these emerging technologies are better suited for circuit switching applications within TONs because of their slow speeds.

The interferometric switches highlighted in sub-sections 3.2.1 – 3.2.6 are all capable of accommodating the rigorous requirements for packet switches. The challenge is to determine which of these is the best option for routing and buffering applications.

The NOLM is reputed to be the first successful architecture used by groups such as British Telecom and Michigan for ultra-fast switching. This architecture relies solely on a passive non-linearity for its switching operation with the minimum temporal switching

duration reported to be ~0.6 ps [86]. Because of its passive operation the refractive index change rapidly relaxes. Consequently, the repetition rate of the device is very high (~100 GHz) as it only relies on the pulse rates of the control pulse laser source. Unfortunately, the passive operation requires long lengths of fibre for the non-linearity to be effective for switching. Even though modern techniques have reduced the fibre length to 10 m from the original 1 km the relatively high control pulse energy of tens of picojoules remains a strong deterrent to making this a practical switching option.

The NLWG is another passive structure but unlike SOA-based switches it does not exhibit intraband carrier dynamics or carrier heating. This technique has recently produced the smallest temporal switching window width of 200 fs at a repetition rate of 10 GHz [87]. Moreover, rates of up to 40 GHz have been demonstrated experimentally [88]. These rates are significantly slower than those produced by NOLMs because of the recombination time required for the photo-generated carriers produced by the control pulse. This passive switch has a poor control pulse coupling efficiency and requires a significant amount of energy (50 pJ) to facilitate switching. Moreover, the wavelength separation between control and data pulses places the data signals in the impractical 1.7 μm region. Consequently, applications for this device are very limited.

The UNI has a reported switching window of 1 ps at a repetition rate of 100 GHz [89]. Higher repetition rates are difficult to achieve because of the SOA carrier dynamics. Note that as the UNI employs a birefringence mechanism to temporally separate the orthogonally polarised pulses far enough to insert the control pulse, long lengths of fibre (≥ 15m) are needed. In addition, as strict polarisation control measures are essential, auxiliary components, which increase the cost of the device, are required.

The TOAD and the SLALOM operate on the same principle, with the main difference between the being the asymmetrical position of the SOA. With small asymmetries, these

devices can produce a very narrow switching window, which is independent of the long carrier relaxation time (100 to 500 ps) of SOA. Consequently, they are both capable of similar performance and will be considered together (denoted TOAD/SLALOM). Note that in each device the minimum switching window width (1ps) is limited by the length of the SOA. The other benefits of these architectures are that the required control pulse energy is very low (<1 pJ), the repetition rates are similar to the UNI (100 GHz), and they are highly integratable because of the short fibre lengths (< 0.5 m) [90].

The only architecture that currently rivals the TOAD/SLALOM performances is the SMZ. This device is capable of switching even narrower pulses because the length of the SOA does not limit the minimum switching window. In theory, the minimum switching window width is determined by the control pulse width. Another advantage of the SMZ is that the switching windows are symmetrical with sharp rise and fall times thereby effectively reducing optical cross-talk at the window boundaries. The asymmetrical switching windows of the TOAD/SLALOM can be avoided by cascading two of these devices ensuring that the asymmetry of the SOA in one device is the mirror image of the other [91].

Table 3.1 [92-93] lists the essential properties of each device separately to facilitate direct comparisons. Note that all the architectures that employ SOAs have an inherent noise figure, which is dependent of the amplifier noise characteristics. Note that the device is classified as integratable if it can be monolithically produced.

Table 3.1 Characteristics of optical switches

Switching Device	Switching Time	Repetition Rate	Control Pulse Energy (pJ)	Noise Figure (dB)	Integratable
SMZ	< 1 ps	100+ GHz	0.25	4-6	Yes
TOAD/ SLALOM	< 1 ps	100+ GHz	0.25	4-6	Yes
UNI	< 1 ps	100+ GHz	0.25	4-6	No
NLWG	0.2 ps	40+ GHz	50	< 2 dB	Yes
NOLM	0.8 ps	100+ GHz	50+	Low	No
MZI modulator	-	20+ GHz	N/A	Low	Yes
MEMS	10 ms	< 1 kHz	N/A	N/A	Yes
Bubble	10 ps	< 1 kHz	N/A	N/A	Yes
Liquid-crystals	-	-	N/A	N/A	No
Electro-holography	-	-	N/A	N/A	-

The SMZ and the TOAD/SLALOM architectures are best suited for optical packet switching because of their fast switching times, high repetition rate, low control pulse energy and good integratability. In addition, these devices have a high degree of operational flexibility and can be manufactured from off the shelf components. In Appendix A the TOAD architecture is used an all-optical 1x2 router, which directs fixed-length packets form its input port to either of its two output ports based on the address information. The SMZ architecture will be used as a switching element within a

recirculating buffer architecture, this is presented in Chapter 7. Such an architecture is ideal for this purpose as the assumption of fixed size data packets is removed. Unlike the TOAD architecture, no physical changes to the device will be required.

3.4 Summary

In this chapter the most popular optical switching technologies available today have been highlighted and their performances compared. The opto-mechanical and opto-electrical devices such as MEMS and Bubble switches, respectively, are identified as more suitable for TONs as they are highly integratable and their relatively slow speed is not a limiting factor. Electro-holography was presented as an innovative technology better suited for WDM switching applications, and investigations revealed that liquid-crystal switching architectures have too many inhibiting features to make them practical. All-optical architectures employing long lengths of fibre (e.g. NOLM and UNI) or requiring large control pulse energies (e.g. NLWG) were also ruled out as contentions for the optimal switching designs. Only the TOAD/SLALOM and SMZ met the requirements for an ultra-fast packet switch. More detailed aspects of these switches will be considered in Appendix A and Chapter 7, when the analysis of the TOAD router and RFLB employing an SMZ switch are presented.

Chapter 4

Wave Propagation and Soliton Transmission

4.1 Introduction

In the previous chapter, various factors that contribute to the performance deterioration of OTDM and WDM transmission systems were highlighted. The origins of these inhibitors can be traced to the non-linear relationship between the refractive index and the electric field intensity. More specifically, because a small non-linear index coefficient arises as the magnitudes of the higher order susceptibility terms are non-zero. In this chapter, a robust mathematical analysis of optical wave propagation is presented. In section 4.2, the Maxwell's equations are employed to develop the general wave propagation equation. The inherent effects of the non-linear contributions are then highlighted in the following section. The non-linear Schrödinger equation (NLSE), which describes the evolution of the pulses within the fibre medium, and the beam propagation method (BPM) along with its numerical implementation, are then presented in sections 4.4 and 4.5, respectively. Soliton theory and the issues surrounding soliton transmission are the subjects of sections 4.6 and 4.7, respectively. Finally, the chapter concludes with the summary section 4.8.

4.2 Non-linear Wave Propagation in Single Mode Fibre

Traditionally, the geometrical optics approach is used to describe the transmission of light rays along optical fibre core by the total internal reflection mechanism. However, this is only valid for multi-mode fibres where the radius of the fibre core is much larger than the operating wavelength [7]. For small core radii, such as in single mode fibres (SMF), geometrical optics fails as it only describes the propagation direction of planar waves. This eliminates any properties of planar waves that interfere during transmission of light along the fibre. To be more precise, light waves within SMF propagate by diffraction. Moreover, the diffraction is duly compensated for by refraction as the core refractive index is higher that the refractive index of the cladding material. In other words, the inhomogeneous medium acts to continuously focus the light into the fibre core. Consequently, the light may be guided over long distances. This is crucial to this study as only SMF are employed since they inherently avoid the inter-modal dispersion associated with multi-mode fibres. The wave theory approach using Maxwell's equations (4.1) – (4.4) [94] are employed to fully expound the dynamics governing the propagation of electric $\mathbf{E}(\mathbf{r},t)$ and magnetic $\mathbf{H}(\mathbf{r},t)$ field vectors in space $\mathbf{r}$ and time t within the SMF medium.

$$\nabla \cdot \mathbf{D} = \rho \tag{4.1}$$

$$\nabla \cdot \mathbf{B} = 0 \tag{4.2}$$

$$\nabla \times \mathbf{E} = -\frac{\partial \mathbf{B}}{\partial t} \tag{4.3}$$

$$\nabla \times \mathbf{H} = \mathbf{J} + \frac{\partial \mathbf{D}}{\partial t} \tag{4.4}$$

Note that **D**, **B**, ρ and **J** are the electric flux, the magnetic flux, charge and current densities, respectively. Where **J** is defined as product of the electric field vector and the conductivity σ of the material, given as:

$$\mathbf{J} = \sigma \mathbf{E} \tag{4.5}$$

The field variables are related to the material equations by:

$$\mathbf{D} = \varepsilon_0 \mathbf{E} + \mathbf{P} \tag{4.6}$$

$$\mathbf{B} = \mu_0 \mathbf{H} + \mathbf{M} \tag{4.7}$$

where ε_0 and μ_0 are the permittivity and permeability of a vacuum, respectively. **P** and **M** represent the dielectric and magnetisation polarisation, respectively. In optical fibre, **M** = 0 and the dielectric polarisation is related to the electric field intensity by [95]:

$$\begin{aligned}\mathbf{P}(\mathbf{r},t) &= \varepsilon_0 \int_{-\infty}^{t} \chi^{(1)}(\mathbf{r}, t-t_1)\mathbf{E}(\mathbf{r},t_1)dt_1 \\ &+ \varepsilon_0 \int_{-\infty-\infty-\infty}^{t\ t\ t} \chi^{(3)}(t-t_1, t-t_2, t-t_3)\mathbf{E}(\mathbf{r},t_1)\mathbf{E}(\mathbf{r},t_2)\mathbf{E}(\mathbf{r},t_3)dt_1 dt_2 dt_3\end{aligned} \tag{4.8a}$$

$$\mathbf{P}(\mathbf{r},t) = \mathbf{P}_L(\mathbf{r},t) + \mathbf{P}_{NL}(\mathbf{r},t) \tag{4.8b}$$

where the subscripts *L* and *NL* denote the linear and non-linear components of the dielectric polarisation. Additionally, $\chi^{(1)}$ and $\chi^{(3)}$ are the linear and third order non-linear

material susceptibility, respectively. Since (4.8a) represents a convolution, it is more convenient to represent it in the frequency domain by taking its Fourier transform. Assuming $\chi^{(3)}(.)$ to be instantaneous yields:

$$\tilde{\mathbf{P}}(\mathbf{r},\omega)=\varepsilon_0\tilde{\chi}^{(1)}(\mathbf{r},\omega)\tilde{\mathbf{E}}(\mathbf{r},\omega)+\varepsilon_0\tilde{\chi}^{(3)}(\mathbf{r},\omega)\tilde{\mathbf{E}}^3(\mathbf{r},\omega). \tag{4.9}$$

Substituting (4.9) into (4.6) gives:

$$\begin{aligned}\tilde{\mathbf{D}}(\mathbf{r},\omega)&=\varepsilon_0\,\tilde{\mathbf{E}}(\mathbf{r},\omega)+\varepsilon_0\tilde{\chi}^{(1)}(\mathbf{r},\omega)\tilde{\mathbf{E}}(\mathbf{r},\omega)+\varepsilon_0\tilde{\chi}^{(3)}(\mathbf{r},\omega)\tilde{\mathbf{E}}^3(\mathbf{r},\omega)\\&=\varepsilon_0\left[1+\tilde{\chi}^{(1)}(\mathbf{r},\omega)\right]\cdot\tilde{\mathbf{E}}(\mathbf{r},\omega)+\varepsilon_0\left[\tilde{\chi}^{(3)}(\mathbf{r},\omega)\tilde{\mathbf{E}}(\mathbf{r},\omega)\right]\cdot\tilde{\mathbf{E}}^2(\mathbf{r},\omega)\\&=\varepsilon\,\tilde{\mathbf{E}}(\mathbf{r},\omega)+\varsigma\cdot\tilde{\mathbf{E}}^2(\mathbf{r},\omega),\end{aligned} \tag{4.10}$$

where $\varepsilon=\varepsilon_0\left[1+\tilde{\chi}^{(1)}(\mathbf{r},\omega)\right]$ and $\varsigma=\varepsilon_0\left[\tilde{\chi}^{(3)}(\mathbf{r},\omega)\tilde{\mathbf{E}}(\mathbf{r},\omega)\right]$.

Further substitution of (4.6) and (4.7) into the Maxwell equations allows the elimination of the flux densities from curl equation (4.3) in favour of the electronic and magnetic field vectors. These details are presented in Appendix B, where the final solution is as shown in (4.11) and (4.12). Note that the assumption that $\mathbf{P}_{NL}$ was negligible (i.e. $\varsigma\tilde{\mathbf{E}}^2(\mathbf{r},\omega)=0$) was made to simplify the calculations.

$$\nabla \times \nabla \times \tilde{\mathbf{E}} = \mu_0 \varepsilon \omega^2 \tilde{\mathbf{E}} \tag{4.11}$$

$$\nabla \times \nabla \times \tilde{\mathbf{H}} = \mu_0 \varepsilon \omega^2 \tilde{\mathbf{H}} \tag{4.12}$$

Equations 4.11 and 4.12 are commonly referred to as the wave equations and they assume that the medium is isotropic.

Note that from this point only the electric field will be considered as it conventionally used to describe the amplitude of the optical signals. Thus (4.14) is obtained by taking the Fourier transform of (4.11) and employing the vector identity in (4.13) where $\mathbf{X}$ represents any arbitrary vector.

$$\nabla \times \nabla \times \tilde{\mathbf{X}} = \nabla(\nabla \cdot \tilde{\mathbf{X}}) - \nabla^2 \tilde{\mathbf{X}} \tag{4.13}$$

$$\nabla^2 \tilde{\mathbf{E}} + \mu_0 \varepsilon \omega^2 \tilde{\mathbf{E}} = \nabla(\nabla \cdot \tilde{\mathbf{E}}) \tag{4.14}$$

Assuming a homogenous medium (4.14) may further be simplified to form (4.15).

$$\nabla^2 \tilde{\mathbf{E}} + \mu_0 \varepsilon \omega^2 \tilde{\mathbf{E}} = 0 \tag{4.15}$$

By noting that the speed of light c and the refractive index n are given by $c = 1/\sqrt{\varepsilon_0 \mu_0}$ and $n^2 = 1 + \chi^{(1)}$ [95], respectively, (4.15) may also be defined as:

$$\nabla^2\tilde{\mathbf{E}}+\frac{\omega^2 n^2}{c^2}\tilde{\mathbf{E}}=0 \tag{4.16}$$

Equations 4.15 and 4.16 describe the propagation of waves in a linear, isotropic medium. However, for the fibre medium, the linearity criteria assumed in its derivation must be relaxed especially under ultra-high speed transmission conditions. More specifically, the higher order susceptibility terms defined in (4.8) must be employed to account for the non-linear dielectric polarisation. This concept is presented in the next section where the origins of the non-linear performance inhibitors previously discussed in Chapter 2 are highlighted.

4.3 Non-linear Phenomenon

The general form of the wave propagation derived in section 4.2 does not readily lend itself to the explanation of the origins of non-linear phenomena present in high-speed communications within optical fibre. To resolve this issue, first rearrange (4.15) to reveal the dielectric polarisation contribution as shown below:

$$\nabla^2\tilde{\mathbf{E}}+\frac{\omega^2}{c^2}\tilde{\mathbf{E}}+\frac{\omega^2}{c^2}\chi^{(1)}\tilde{\mathbf{E}}=0 \tag{4.17}$$

$$\nabla^2\tilde{\mathbf{E}}+\frac{\omega^2}{c^2}\tilde{\mathbf{E}}+\omega^2\mu_0\tilde{\mathbf{P}}=0 \tag{4.18}$$

Second, form (4.19) by finding the inverse Fourier transform of (4.18) [96].

$$\nabla^2 \mathbf{E}(\mathbf{r},t) = -\frac{1}{c^2}\frac{\partial \mathbf{E}^2(\mathbf{r},t)}{\partial t^2} - \mu_0 \frac{\partial \mathbf{P}^2(\mathbf{r},t)}{\partial t^2}. \tag{4.19}$$

Finally, note that both the linear and non-linear dielectric polarisation contribution defined in (4.8) must be considered in (4.19).

In describing the effect of the non-linearity on the electric field propagation lets assume a monochromatic plane wave with an electric field defined by [10]:

$$\mathbf{E}(z,t) = E\cos(\omega_0 t - \beta_0 z), \tag{4.20}$$

where z and β_0 represent the distance and the propagation constant, respectively. Taking the inverse Fourier transform of the second term in (4.9) and considering propagation in the z direction alone yields (4.21).

$$\begin{aligned} P_{NL}(z,t) &= \varepsilon_0 \chi^{(3)} E^3 \cos^3(\omega_0 t - \beta_0 z), \\ &= \varepsilon_0 \chi^{(3)} E^3 \left[\frac{3}{4}\cos(\omega_0 t - \beta_0 z) + \frac{1}{4}\cos(3\omega_0 t - 3\beta_0 z)\right] \\ &\approx \left(\frac{3}{4}\chi^{(3)} E^2\right)\varepsilon_0 E\cos(\omega_0 t - \beta_0 z). \end{aligned} \tag{4.21}$$

As is shown in Appendix B, when the non-linear contributions are taken into account in the wave propagation equation it may be solved for β_0 yielding [7]:

$$\beta_0 = \frac{\omega_0}{c}\left(n + \frac{3}{8}\chi^{(3)} E^2\right),$$

$$\beta_0 = \frac{\omega_0}{c}\left(n + n_2 E^2\right), \tag{4.22}$$

where n_2 represents the intensity dependant refractive index.

The effect of n_2 is observed in the magnitude of SPM, which is defined as [96] (also see (2.5)):

$$\varphi_{NL} = \frac{\omega_0}{c} n_2 E^2 L, \tag{4.23}$$

where L is the propagation length.

Applying the above definition, to the scenario where two electrical fields of the same magnitude given by $\mathbf{E}_a(z,t) = E_a \cos(\omega_a t - \beta_a z)$ and $\mathbf{E}_b(z,t) = E_b \cos(\omega_b t - \beta_b z)$ are co-propagating within the fibre medium, the magnitude of the resulting non-linear phase shift is given by $\varphi_{NL} = \frac{\omega_0}{c} n_2 L\left(E_a^2 + 2E_b^2\right)$. Here, the first and second terms within the brackets represents the contributions due to SPM and XPM, respectively. XPM is a major concern in long haul high-speed WDM links since it contributes twice as much as SPM to the phase change.

4.4 Pulse Propagation within Single Mode Optical Fibre

Assuming the transmission of monochromatic plane waves, then the associated electric field of a fundamental mode may be described by [95]:

$$\mathbf{E}(\mathbf{r},t) = A(z,t)e^{-(i\omega_0 t - \beta_0 z)}, \tag{4.24}$$

where $A(z,t)$ represents the slowly varying complex wave envelope. To highlight the relationship between the angular frequency and refractive index β_0, defined in (4.22), is rearranged to form:

$$\beta_0(\omega) = \frac{\omega_0}{c} n(\omega) + \gamma P, \tag{4.25}$$

where the non-linear coefficient γ is equivalent to $\omega n_2/(A_{eff}c)$. Note that E^2 is normalised so that it is proportional to the power P of the pulse. To account for effects of fibre dispersion the (linear) propagation constant is (Taylor series) expanded about the centre frequency (ω_0) to give:

$$\begin{aligned} \frac{\omega_0}{c} n(\omega) &= \beta_0 + \beta_1(\Delta\omega) + \frac{1}{2}\beta_2(\Delta\omega)^2 + \frac{1}{6}\beta_3(\Delta\omega)^3 + \cdots \\ &= \beta_0 + \Delta\beta, \end{aligned} \tag{4.26}$$

where $\Delta\beta = \beta_1(\Delta\omega) + \frac{1}{2}\beta_2(\Delta\omega)^2 + \frac{1}{6}\beta_3(\Delta\omega)^3 + \ldots$, $\Delta\omega = \omega - \omega_0$, $1/\beta_1$ is the velocity of the pulse, and β_2 and β_3 are the group velocity dispersion (GVD) parameter and the third order dispersion parameter, respectively.

To mathematically describe the variation of the amplitude profile $A(z,t)$ as it propagates within SMF first note that its Fourier transform pair is defined by [97]:

$$A(\Delta\beta,\Delta\omega) = \iint A(z,t)e^{-i\Delta\beta z}e^{i\Delta\omega t}d(\Delta\beta)d(\Delta\omega) \tag{4.27}$$

$$A(z,t) = \frac{1}{(2\pi)^2}\iint A(\Delta\beta,\Delta\omega)e^{i\Delta\beta z}e^{-i\Delta\omega t}d(\Delta\beta)d(\Delta\omega) \tag{4.28}$$

Taking the partial derivatives of (4.28) with respect to z and t, results in:

$$\frac{\partial A(z,t)}{\partial z} = i\Delta\beta \cdot A(z,t) \tag{4.29}$$

$$\frac{\partial A(z,t)}{\partial t} = -i\Delta\omega \cdot A(z,t) \tag{4.30}$$

$$\frac{\partial^2 A(z,t)}{\partial t^2} = -\Delta\omega^2 \cdot A(z,t) \tag{4.31}$$

$$\frac{\partial^3 A(z,t)}{\partial t^3} = i\Delta\omega^3 \cdot A(z,t) \tag{4.32}$$

Substituting the expression for $\Delta\beta$ into (4.29) and then further substituting (4.30) – (4.32) into the resulting expression eliminates the $\Delta\beta$ and $\Delta\omega$ terms and forms the pulse evolution expression given as [11], [96], [98-99]:

$$\frac{\partial A(z,t)}{\partial z} + \beta_1 \cdot \frac{\partial A(z,t)}{\partial t} + \frac{i}{2}\cdot\beta_2 \cdot \frac{\partial^2 A(z,t)}{\partial t^2} - \frac{1}{6}\cdot\beta_3 \cdot \frac{\partial^3 A(z,t)}{\partial t^3} - i\gamma \cdot P \cdot A(z,t) = 0 \tag{4.33}$$

It is useful to employ this frame of reference before solving the pulse propagation equation. By utilising the transform $\tau = t - \beta_1 z$ and assuming loss free fibre (4.33) may be expressed as [11], [96], [98-99]:

$$\frac{\partial A(z,\tau)}{dz}+\frac{i}{2}\cdot\beta_2\cdot\frac{\partial^2 A(z,\tau)}{\partial\tau^2}-\frac{1}{6}\cdot\beta_3\cdot\frac{\partial^3 A(z,\tau)}{\partial\tau^3}-i\gamma\cdot P\cdot A(z,\tau)=0 \qquad (4.34)$$

Equation 4.34 is commonly referred to as the non-linear Schrödinger equation (NLSE).

4.5 Beam Propagation Method

In general, the exact analytical solution of (4.34) is difficult to obtain unless the effects of fibre loss and higher order non-linear terms are assumed to be negligible [11], [96], [98-99]. However, no such assumptions are required in the beam propagation method (BPM), which is a numerical technique that can readily be used to model pulse profile evolution in optical fibre by means of computer simulation.

As illustrated in Figure 4.1, this recursive algorithm splits the entire propagation distance into small segments of length Δz and exploits the independent nature of dispersion including fibre loss and the fibre non-linearity over small distances. More specifically, the dispersion and loss effects are considered as the pulse propagates over the first and second halves of the segment whereas the non-linear effects are assumed to be lumped at the centre.

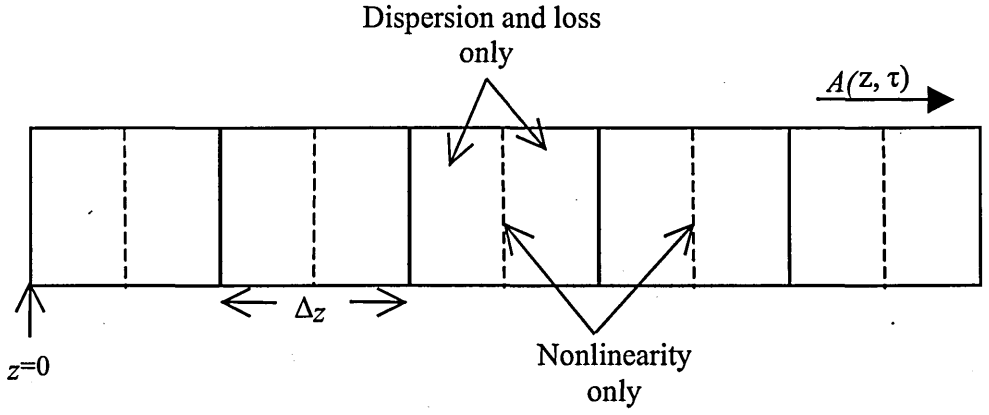

Figure 4.1 Schematic illustration of the beam propagation technique

To include the effects of the intrinsic fibre loss α in the NLSE (4.34) may be expressed as [11], [96], [98-99]:

$$\frac{\partial A(z,\tau)}{dz}+\frac{\alpha A(z,\tau)}{2}+\frac{i}{2}\cdot\beta_2\cdot\frac{\partial^2 A(z,\tau)}{\partial\tau^2}-\frac{1}{6}\cdot\beta_3\cdot\frac{\partial^3 A(z,\tau)}{\partial\tau^3}-i\gamma\cdot P\cdot A(z,\tau)=0 \qquad (4.35)$$

For convenience, (4.35) may then be separated out into its differential operator $\hat{D}$, which accounts for the dispersion and loss, and non-linear operator $\hat{N}$, which governs the effects of non-linearity on pulse propagation to yield [11], [96], [98-99]:

$$\frac{\partial A(z,\tau)}{dz}=(\hat{D}+\hat{N})A(z,\tau) \qquad (4.36)$$

where

$$\hat{D} = -\frac{i}{2} \cdot \beta_2 \cdot \frac{\partial^2}{\partial t^2} + \frac{1}{6} \cdot \beta_3 \cdot \frac{\partial^3}{\partial \tau^3} - \frac{\alpha}{2} \tag{4.37}$$

$$\hat{N} = i\gamma \cdot P \tag{4.38}$$

Substituting (4.31) and (4.32) into (4.37) results in:

$$\hat{D} = i\frac{\beta_2}{2} \cdot \omega^2 + i\frac{\beta_3}{6} \cdot \omega^3 - \frac{\alpha}{2}. \tag{4.39}$$

which can now be numerically manipulated.

As (4.36) is a first order differential equation, the general solution for $A(z,\tau)$ is an exponential form. Consequently, using the algorithm as explained above and further illustrated in Figure 4.1, the profile at distance $z+\Delta z$ may mathematically express as:

$$A(z+\Delta z,\tau) = \exp\left[\frac{\Delta z}{2}\hat{D}\right] \cdot \exp\left[\hat{N}(A(z+\Delta z/2,\tau) \cdot \Delta z\right] \cdot \exp\left[\frac{\Delta z}{2}\hat{D}\right] \cdot A(z,\tau). \tag{4.40}$$

The first and last exponential product terms in (4.40) represent the dispersion and loss, whereas the second exponential product term represents the non-linearity. This process may then be repeated recursively over the entire propagation distance L_{tot} to determine the pulse profile $A(L_{tot},\tau)$.

4.6 Solitons

The analytical NLSE solutions are obtained by employing the inverse scattering technique under the assumptions outlined in Section 4.5 [99]. In the anomalous chromatic regime (i.e. $\beta_2 < 0$) the solution are termed soliton pulses. The envelopes of these pulses are either stationary with distance or periodic. Moreover, the initial amplitude profile at $z = 0$ is described by the general equation:

$$A(0,\tau) = \overline{N}\, sech\left(\frac{1.763 \cdot \tau}{T_{FWHM}}\right) \tag{4.41}$$

where T_{FWHM} is the full width half maximum pulse width and $\overline{N}$ is the soliton number defined by:

$$\overline{N}^2 = \frac{T_{FWHM}^2 \cdot \gamma \cdot P_0}{3.108 \cdot |\beta_2|} \tag{4.42}$$

where P_0 is the peak optical power of the launched pulse.

The parameters listed in Table 4.1 were input to the BPM equation and the resulting fundamental ($\overline{N} = 1$) soliton propagation pulse profile is shown in Figure 4.2. The pulse width chosen is typical for high-speed communication as it allows for the narrow inter-pulse spacing. Observe that in the absence of fibre loss the pulse profile remains unchanged over the entire propagation distance. The negative time on the x-axis results from the temporally retarded frame of reference (τ) in (4.34), and is consistent with the literature.

Table 4.1 Parameter listing for fundamental soliton propagation

Parameter	Value
Pulse width (T_{FWHM})	17.63 ps
GVD parameter (β_2)	-18 ps^2 km^{-1}
Nonlinear refractive index (n_2)	$3.2x10^{-8}$ μm^2 W^{-1}
Effective cross-sectional area (A_{eff})	50 μm^2
Carrier frequency (ω_0)	1.55 μm
Intrinsic fibre loss (α)	0 dB km^{-1}
Speed of light in a vacuum (c)	$3x10^8$ ms^{-1}
Soliton Order ($\overline{N}$)	1
Peak power (P_0)	69.38 mW
Total propagation distance (L_{tot})	17.6 km

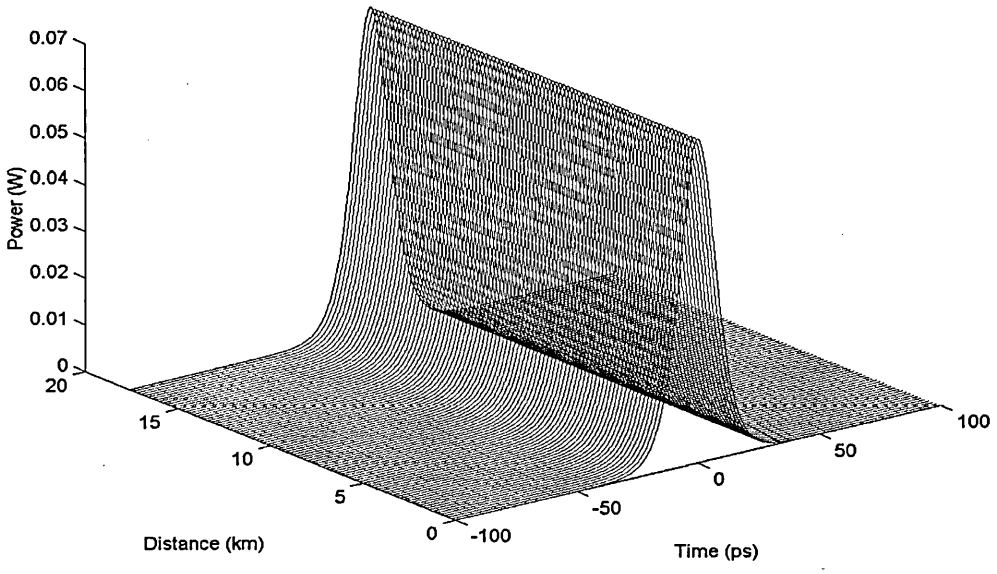

Figure 4.2 Evolutionary profile of the fundamental soliton pulse

Second ($\overline{N} = 2$) and third ($\overline{N} = 3$) order soliton pulses are obtained by using the same parameters in Table 4.1 except for changing the peak powers to 277.5 mw and 624.4 mw, respectively. The associated changes to the propagating profile are as shown in

Figures 4.3 and 4.4. Note that the second and third order solitons pulse profiles oscillate with a period (Z_0) defined by [11], [96], [98-99]:

$$Z_0 = 0.505 \cdot \frac{T_{FWHM}^2}{|\beta_2|} \tag{4.43}$$

For the second order soliton, the launched pulse is initially compressed to a narrower width and higher peak power at the initial stage of propagation due to the positive chirping induced by SPM. The presence of small side lobe pulses are observed between ~3 and ~4 km. The maximum peak power is obtained at distance $Z_0/2$ = 4.36 km after which the pulse broadens and returns to its original launched profile at Z_0 = 8.72 km. The third order soliton is also observed to undergo initial compression, however at $Z_0/2$ = 4.36 km, two distinct pulses are created due to the SPM and GVD forces. The second half of the propagation distance is a mirror image of the first with the pulse merging to regain its initial shape at the end of the soliton period. Longer propagation distances for the higher-order solitons ($\overline{N} \geq 2$) result in the pulse profile cycle being repeated.

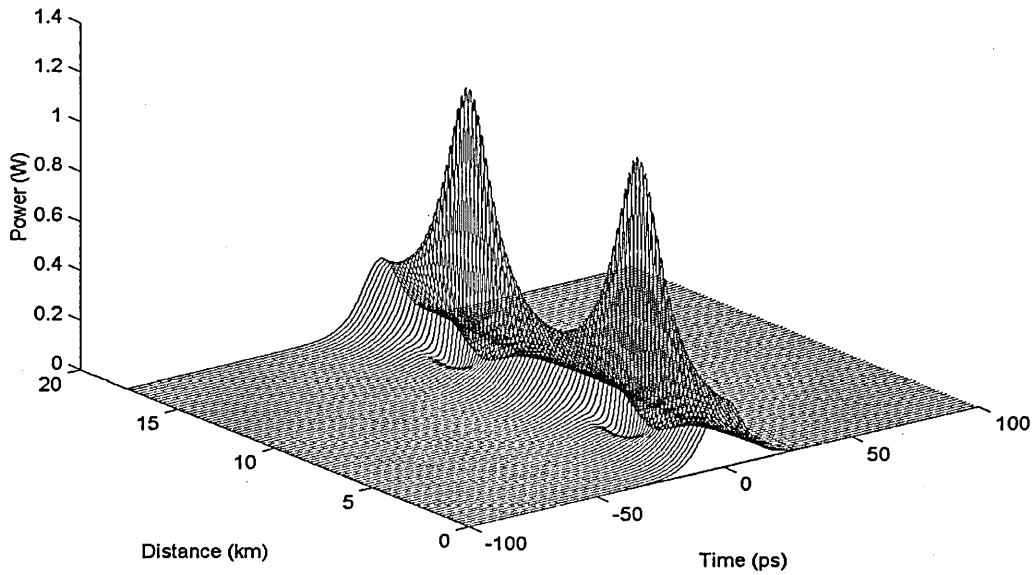

Figure 4.3 Evolutionary profile of a second order soliton pulse

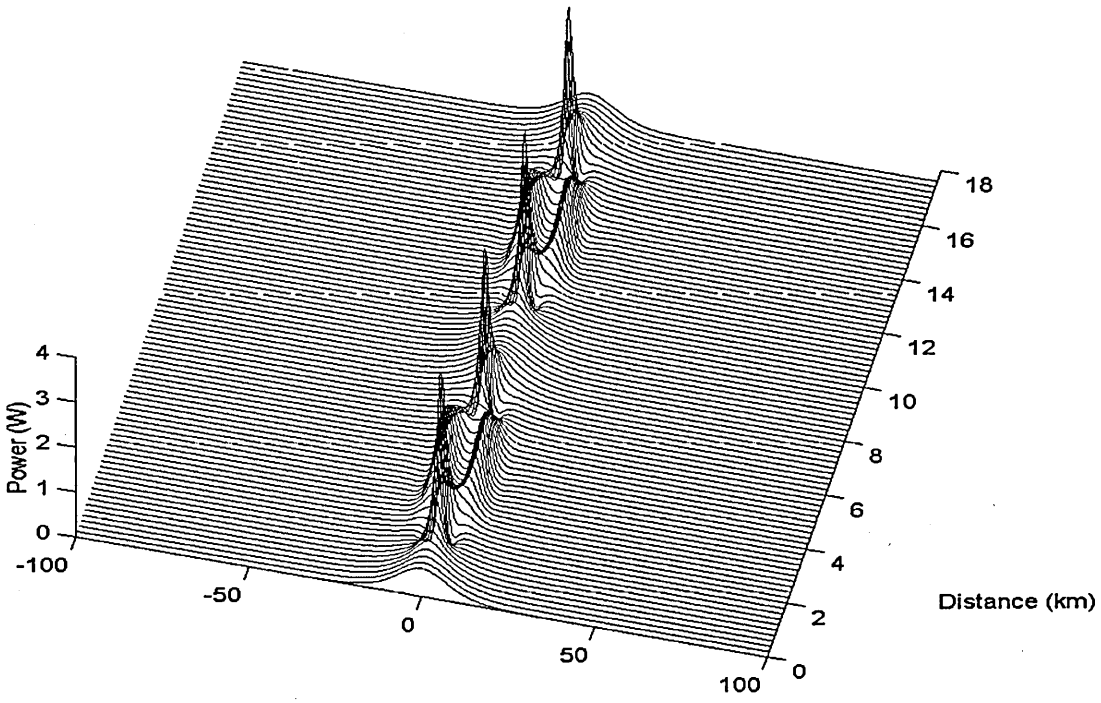

Figure 4.4 Evolutionary profile of a third order soliton pulse

4.7 Soliton Based Communication Systems

Recall that RZ pulses are exploited by the OTDM communication systems to increase the transmitted bit rates. For the ultra-high speed transmission rates this amounts to more than just changing the duty cycle of square wave pulses as the profile of the launched pulses also provides benefits. Soliton profiled pulses have been promoted as the solution to obtaining ultra-high bit rates as they inherently balance the effects of SPM and GVD to avoid pulse broadening. Moreover, they remain stable during collisions with other soliton pulses. Experimental results using soliton transmission systems have been reported to achieve bit rates ranging from 2.5 Gbits/s to 100+ Gbits/s [100-110] over long distances (>> 200 km), therein authenticating their application to

communications systems. Moreover, Nakazawa et al [111] have employed synchronous modulation controls to demonstrate soliton transmission over infinite distances (100 million km). Other soliton applications include employment within pulse position modulation systems [112], which inherently provide a degree of error detection and as control pulses to produce symmetric switching windows in NOLM and TOAD switches [97]. Eric Lerner [113] even touted them as the basis for replacement of WDM technologies.

While decreasing the bit period effectively increases the bit rate, a practical limit exists as soliton pulses may interact causing them to oscillate within their allocated bit positions [11], [96], [99], [114-115]. This will inevitably result in an increase in the bit error rate performance of the transmission. The interaction can be shown to be proportional to the relative amplitude A_r and relative phase θ of the pulses. Moreover, the interaction is found to be attractive when the relative phase is equal to zero and repulsive when the pulses are in anti-phase. To fully illustrate this point, consider (4.44), which describes the launched amplitude profile of the two adjacent soliton pulses with arbitrary relative amplitudes and phase [11], [96], [98-99].

$$A(0+\tau) = N\,\mathrm{sech}\left[\frac{1.763(\tau - q_0)}{T_{FWHM}}\right] + N \cdot A_r \cdot \mathrm{sech}\left[\frac{1.763(\tau + q_0)}{T_{FWHM}}\right] e^{i\theta}, \qquad (4.44)$$

Note that $2q_0$ represents the initial separation between the pulses.

The evolution profile is then determined numerically by substituting (4.44) into the BPM algorithm and again using the key parameters listed in Table 4.1. Figure 4.5 shows the evolutionary profile when the both pulses are identical, that is $A_r = 1$ and the pulses are in-phase; the initial separation of the pulses is 40 ps. Observe that the pulses first coalesce at $Z \cong 35$ km to form a single peak with a maximum power of ~250 mW before reacquiring the original two-pulse profile. This pattern repeats itself periodically.

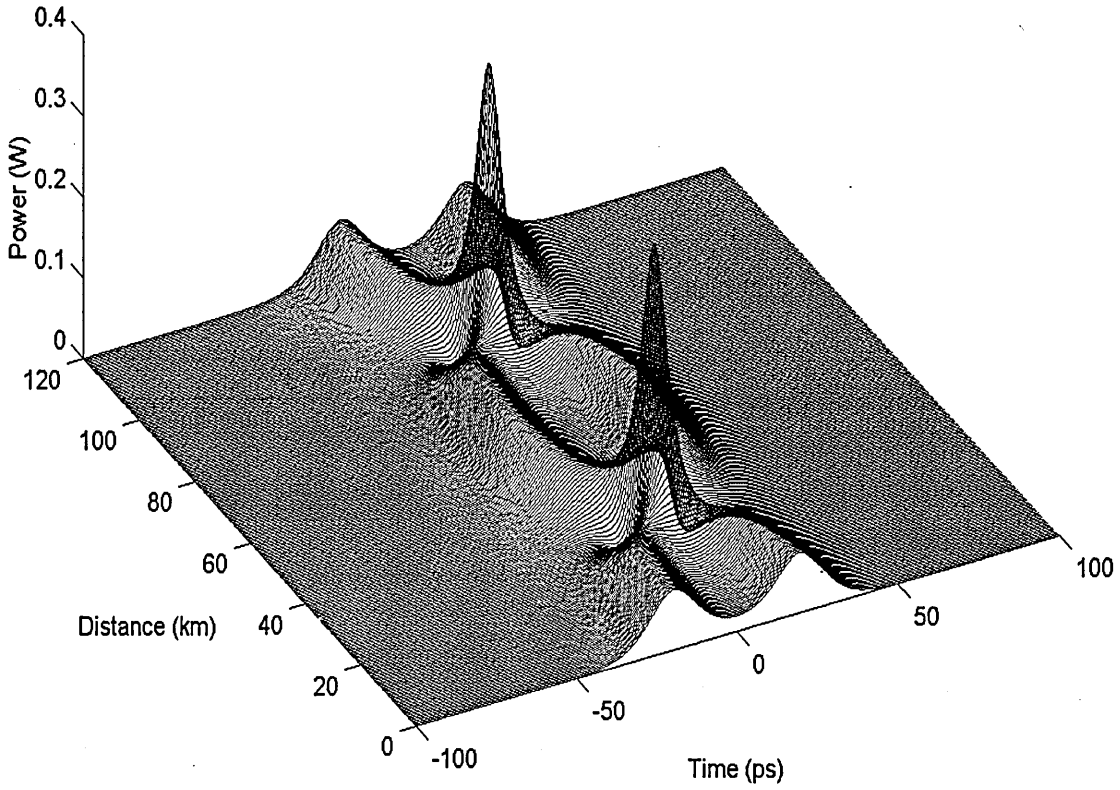

Figure 4.5 Evolution profile of two propgating soliton pulses ($N = 1$, $A_R = 1$, $\theta = 0$, $q_0 = 20$ps)

Figure 4.6 shows the evolutionary profile when both pulses are launched with the same amplitude (i.e. $A_r = 1$) and the relative phase is 180 °. In this scenario the pulses which where were initially 40 ps apart are observed to repel each other over the propagation distance, becoming apart 80 ps after 50 km.

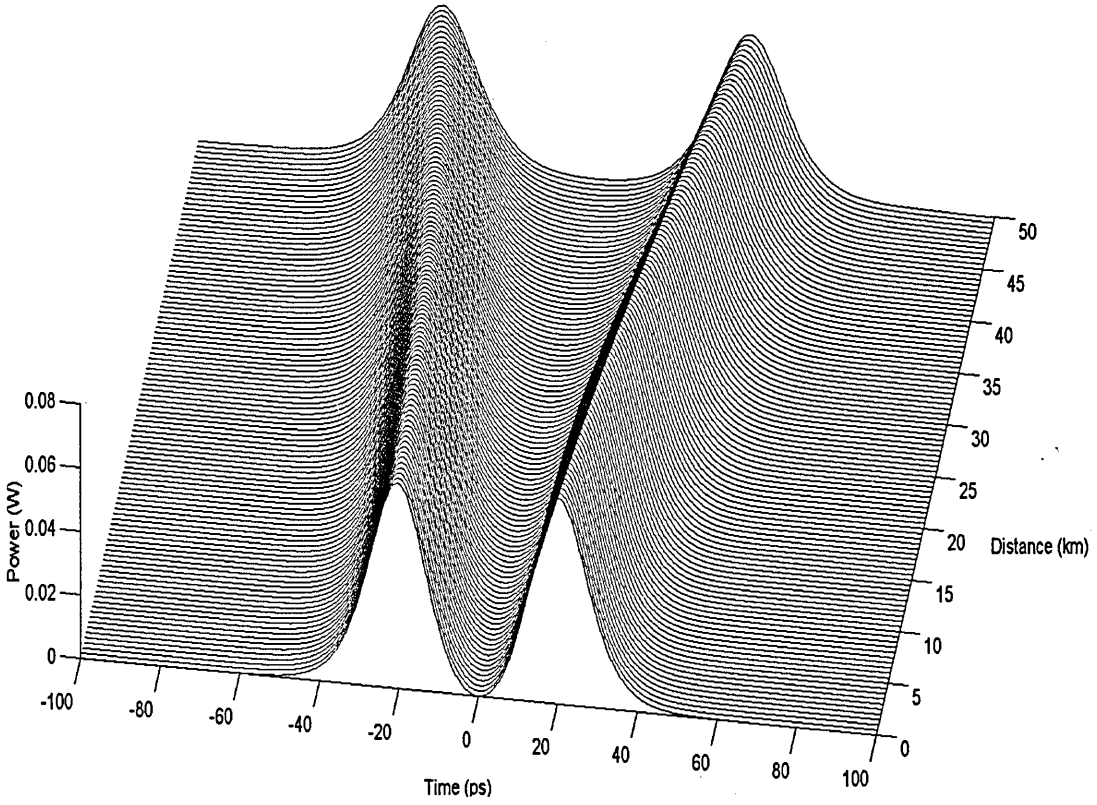

Figure 4.6 Evolution profile of two propgating soliton pulses ($N = 1$, $A_R = 1$, $\theta = \pi$, $q_0 = 20$ps)

Techniques to alleviate the interaction between the pulses include using pulses with different initial amplitudes and increasing the distance between the adjacent pulses. The latter effectively places an upper limit on the achievable bit rate. To illustrate, lets revisit the scenario where the two identical adjacent pulses are in phase. Figure 4.7 highlights that increasing the separation distance to 80 ps mitigates the interactive forces and effectively prevents the periodic oscillations.

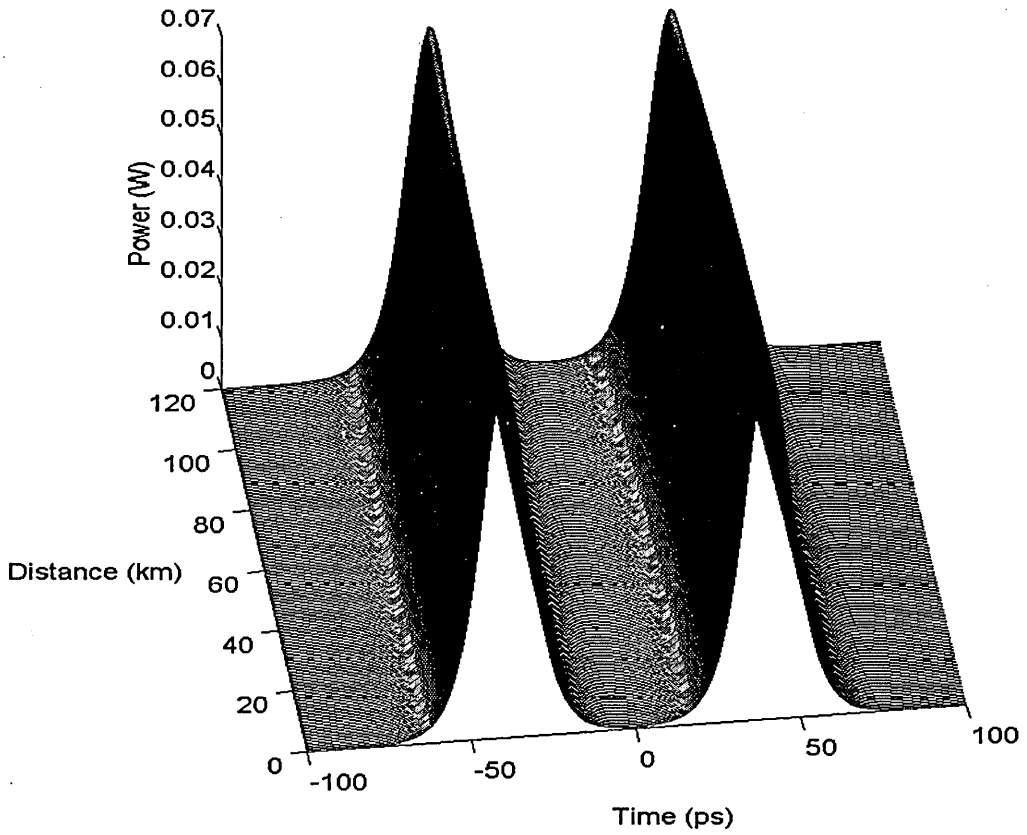

Figure 4.7 Evolution profile of two propgating soliton pulses ($N = 1$, $A_R = 1$, $\theta = 0$, $q_0 = 40$ ps)

4.8 Summary

In this chapter, the propagation of light within optical fibre has been examined. In addition, the origins of the non-linear phenomenon such as SPM and XPM have been presented. Moreover, the critical role that SPM plays in negating the effects of GVD for soliton propagation was highlighted. The NLSE equation and the BPM, which governs the propagation of pulses with the fibre medium, were also presented. Finally, soliton pulse dynamics and their implications on soliton based communication systems were examined.

The core material presented within this chapter is utilised in the subsequent chapter where the passive recirculating fibre loop buffer is modelled and its BER performance is characterised.

Chapter 5

The Passive Recirculating Fibre Loop Buffer (RFLB)

5.1 Introduction

The growing demand for increased network capacity has generated interest in the development of ultra-fast optical networks where the tardy opto-electrical (O/E) and electro-optical (E/O) conversions that are inherent in common fibre network systems are avoided [116-117]. Intuitively, this results in a significant reduction in bandwidth bottlenecks and superior quality of service (QoS) standards [118]. Recall that in OTDM networks where signals are combined for transmission on a single communications line or channel, the use of short duration (soliton) pulses allows information to be transmitted at very high bit rates (>100 Gbit/s) [49], [118-120]. Within such networks a mechanism for resolving contention among multiple input ports going to a single output port is a crucial requirement [121]. Thus it becomes necessary to provide a temporary storage element in order to avoid dropping packets. Since electronic buffering and retransmission reduces system throughput, then an all-optical approach is the preferred option. In addition, at the transmitter node, the optical buffers may hold data packets while they wait for access to the network. Similarly, at the receiver they may be used firstly, to present multiple copies of the incoming data packets to a demultiplexer or rate converter. Secondly, to compensate for the slow speeds inherent to the O/E interface. All-optical buffer designers are faced with a vast number of design variables and careful

analysis is required to determine the optimal configuration for given applications and network topologies. This is to ensure that both bit and packet integrity is maintained and maximum storage times are achieved without unrealistic expectations on power or energy requirements. In this chapter, we present a mathematical analysis of an all-optical passive RFLB. First, the RFLB model and its optimisation is briefly discussed in the section 5.2, followed by a case study of the propagation of different pulse profiles types within the buffer architecture in section 5.3. Next, a communications system model is presented in section 5.4 along with its associated simulated and theoretical results. The influence of optical fibre type and data rate on the BER performance for the buffer architecture is then presented in sections 5.5 and 5.6 respectively, before the chapter concludes with a summary in section 5.7.

5.2 Recirculating Fibre Loop Buffer Model

The key issues in designing the buffer model are simplicity with regard to the control mechanism and its suitability for OTDM systems. Given the current impracticality of storing the data (light) pulses, and in the absence of optical random access memory (RAM), lengths of fibre are employed as the popular choice of delay mechanism. However, light entering such buffers has a fixed propagation delay thereby making them impractical for long delay times and/or dynamic storage applications. Figure. 5.1 shows a typical passive RFLB [122-124]. Pulses entering the buffer via path AB circulate for a discrete period of time, until they are ready to be switched out via path BC. Conversely, unbuffered pulses travel along the path AC. The switch is assumed to be ideal with no insertion loss and crosstalk due to leakage, unless otherwise stated.

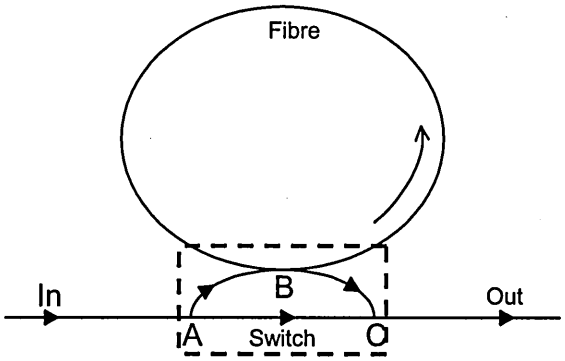

Figure 5.1 Schematic of passive RFLB

For a given fibre length L, the maximum delay per loop traversal T_{loop} is defined as [122-124]:

$$T_{loop} = \frac{nL}{c}, \tag{5.1}$$

where n is the refractive index and c is the speed of light in the vacuum. Moreover, the maximum number of bits M that can be stored within that length of fibre for a given bit rate B is defined as [122-124]:

$$M = \frac{nL}{c}B. \tag{5.2}$$

As indicated in (5.1) and (5.2) optimisation of the passive RFLB inherently depends on the fibre length and bit rates. Increasing L results in longer storage times and the possibility of storing a larger number of bits. To aid synchronisation, T_{loop} should be chosen to be an integer multiple of the packet duration including the appropriate guard band time required for any overhead processing. Consequently, M = Packet length (bits) + Processing time (bits).

Combining (5.1) and (5.2) produces the partial differential given by:

$$\frac{\partial T_{Loop}}{\partial L} = \frac{M}{BL}. \tag{5.3}$$

The second order partial derivative of the above equation yields:

$$\frac{\partial^2 T_{Loop}}{\partial L^2} = -\frac{M}{BL^2}, \tag{5.4}$$

which may be employed to measure the utilisation efficiency of the buffer. Whilst simultaneously increasing the number of bits and the data rate results in increased buffer storage capacity, the resulting inter-pulse interactions become non-negligible and degrade the BER. To avoid this scenario, the initial configuration is taken as the point where the numerical value of (5.4) approaches zero.

The efficiency derivative is normalised to one by dividing each efficiency derivative by the maximum efficiency derivative obtained. Figure 5.2 shows a plot of this normalised buffer efficiency under various conditions. In the first scenario, B and L are taken to be constant with values of 100 Gbit/s, and 500 m, respectively. M is then varied over the range of 1 kbit to 1 Mbit. The plot shows that reducing the number of bits increases the utilisation efficiency. Conversely, in the second scenario, M and L are taken to be constant with values of 1 kbit, and 500 m, respectively. B is then varied over the range of 2.5 Gbit/s to ~2 Tbit/s. In this case the utilisation efficiency is observed to increase as the bit rate is increased.

Significantly, the crossover point (efficiency derivative = $3.13E^{-2}$) represents a valid solution of (5.4) when L, M and B are 500 m, 38.2 kbits and 80 Gbit/s, respectively. Note that although this is the valid solution for the equation, it does not consider the soliton interaction or dispersive effects, which deteriorate the QoS performance of the

buffer. The task of the designer is to determine the optimal performance using this crossover point as a benchmark. Typically, better performances are obtained by lengthening the fibre, decreasing the data rate and increasing the number of bits.

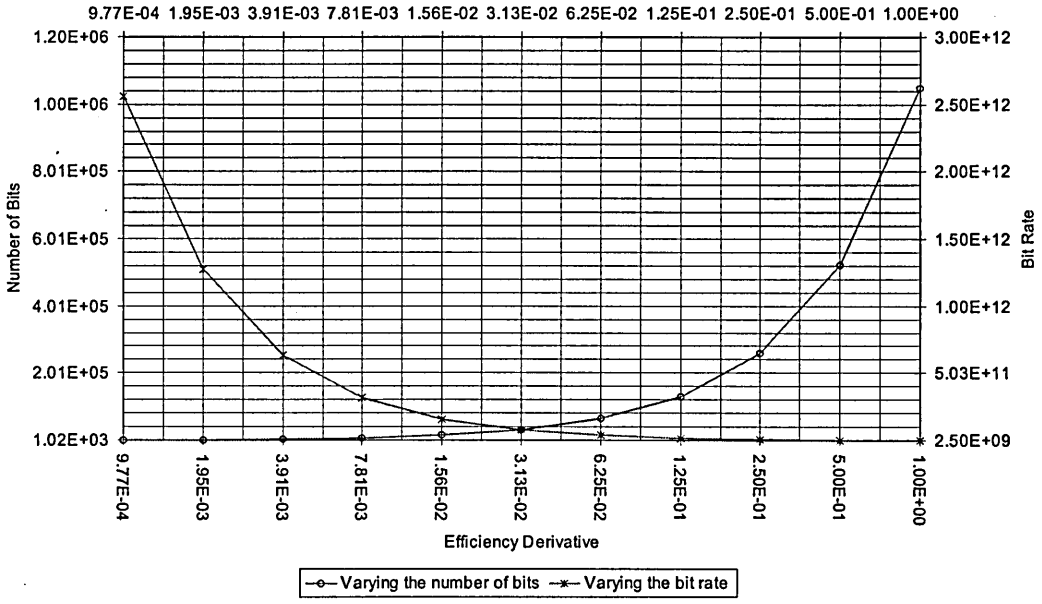

Figure 5.2 Plot of the buffer utilisation efficiency

5.3 Buffered Pulse Propagating Profiles

Two different pulse waveforms, namely the soliton and Gaussian, are used for circulation within a unit buffer length of fibre (500 m). The initial launched optical pulse profiles are defined by [11]:

Soliton: $$S(0,\tau) = \overline{N}\,\mathrm{Sech}\left[\tau/T_0\right], \tag{5.5}$$

Gaussian: $$G(0,\tau) = \overline{N}\,e^{-\left(\frac{\tau}{2T_0}\right)^2}, \tag{5.6}$$

where $\overline{N}$, τ and T_0 are as defined previously in Chapter 4.

However, note that for the soliton and Gaussian pulses, T_0 is defined as the full width half maximum divided by 1.763 and 1.665, respectively. The evolutionary profiles of these circulating pulse types were produced by substituting (5.5) and (5.6) into the BPM algorithm and employing the parameters listed in Table 5.1.

Table 5.1 Passive RFLB global simulation parameters

Parameter	Values
Wavelength of signal (λ_s)	1.55 μm
Refractive index of fibre (n)	~1.5
Speed of light (c)	$3x10^8$ ms^{-1}
Effective fibre core area (A_{eff})	50 μm^2
Non-linear refractive index (n_2)	$3.2x10^{-8}$ μm^2 w^{-1}
Loop unit length (L)	500 m
First order dispersion parameter (β_2)	-18 ps^2 km^{-1}
Fibre loss parameter (α_{dB})	0.2 dB/km
Number of bits generated	$2x10^5$ bits
Data rate(s)	2.5, 5.0 and 10 Gbit/s
Pulse shapes	Soliton and Gaussian

Figures 5.3 and 5.4 show the resulting output power versus the buffer loop number and the propagation time for the soliton and Gaussian pulses, respectively. Note that the intrinsic fibre loss limits the propagation distance of soliton transmission, since solitons need sufficient power to balance the non-linearity against dispersion. As is usually expected, in both cases the dispersion serves to broaden the pulses. This is due to power loss of the signal propagating along the fibre. To sustain soliton propagation, it is necessary to employ an optical amplifier to maintain the peak power level. Note that in both cases, the initial pulse width T_0 is 10 ps and the conditions necessary for fundamental soliton propagation (i.e. $\overline{N} = 1$) are employed. Notice that after a few loop traversals, the Gaussian shape is in the transformation process of becoming a

fundamental soliton shape before dispersing, due to the intrinsic fibre loss. Thus there is no reason why one should not employ Gaussian pulse within an optical buffer, provided it has enough peak power to sustain the soliton properties.

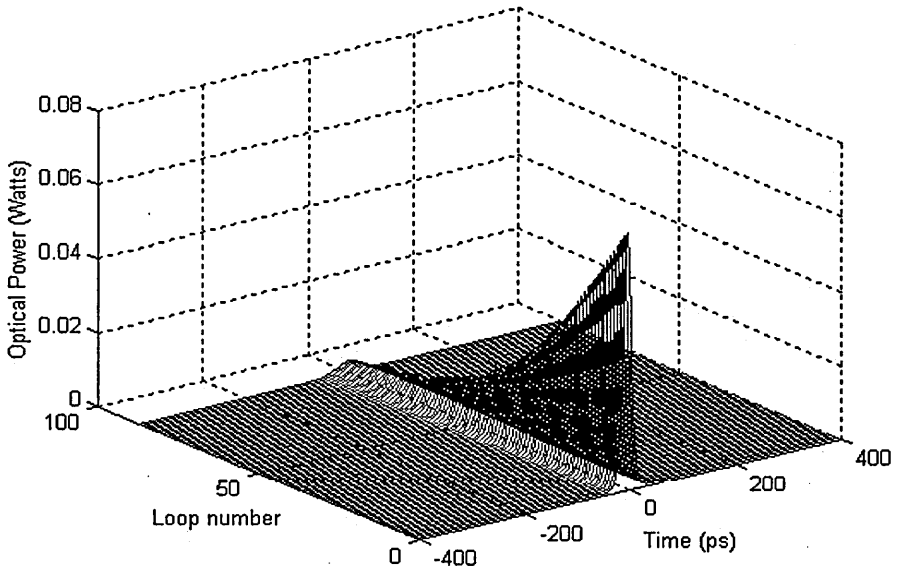

Figure 5.3 Power profile of propagating soliton pulse (T_0 = 10 ps)

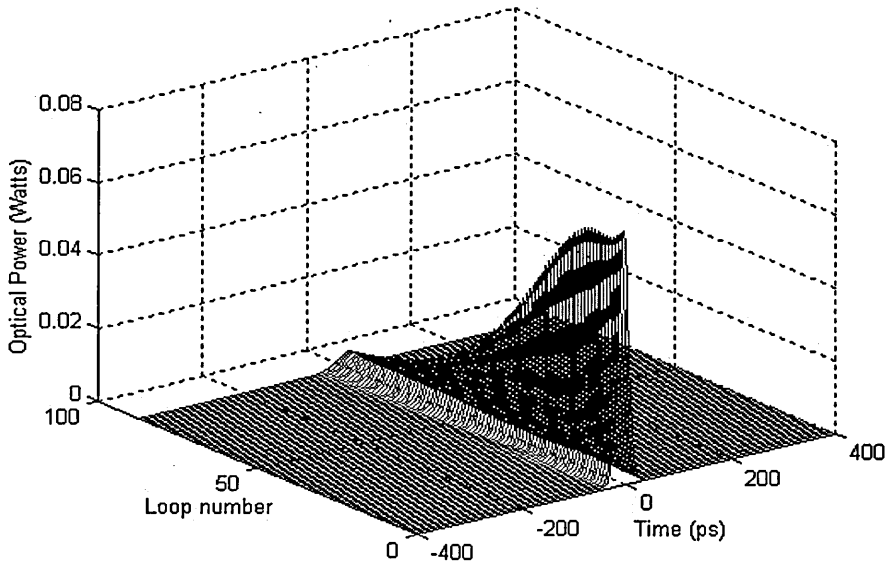

Figure 5.4 Power profile of propagating Gaussian pulse (T_0 = 10 ps)

Furthermore, as both pulse profiles attenuate exponentially, it suggests that using higher input powers and dispersion compensation fibre would result in longer storage times.

Note that Gaussian pulses launched under the conditions that allow them to become soliton will now be referred to as the Gaussian-soliton pulses.

Figure 5.5 shows the simulated energy pulse for both the soliton and Gaussian-soliton pulses as a function of the loop number l_n traversed. Notice that in both cases, the relationship between the gradient descent and the fibre attenuation parameter is highlighted. More specifically, we find that the gradient is equal to the fibre loss per loop iteration α_l. This result could explain the flattening of the Gaussian-soliton pulse profile for loop numbers from 9 to 30. In this region, to compensate for the energy decay rate and to therefore keep the balance between power loss and dispersion the pulse becomes narrower.

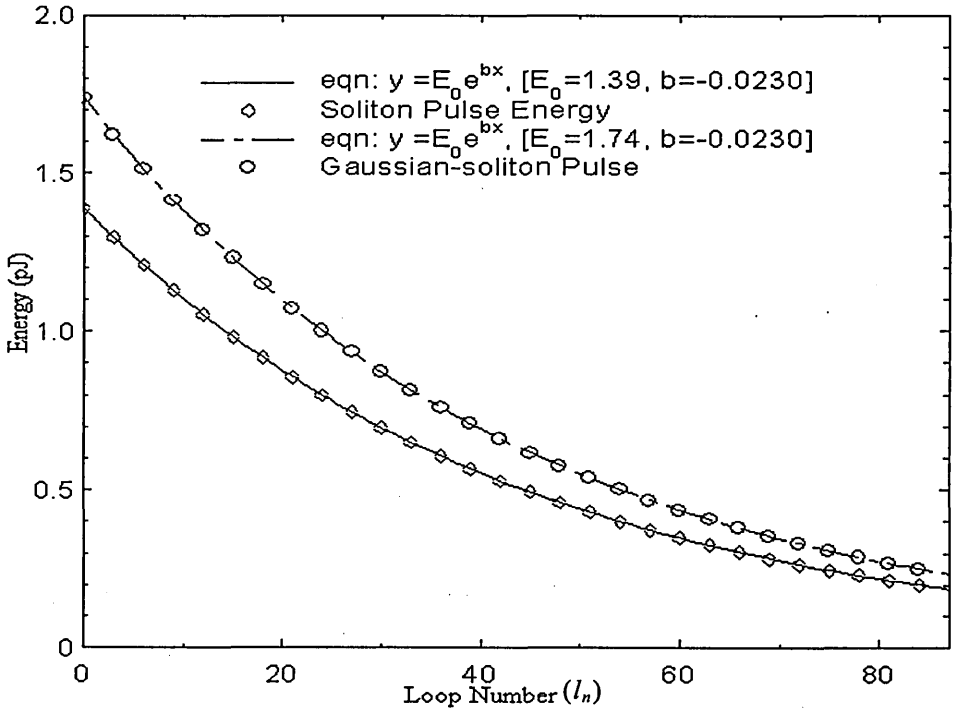

Figure 5.5 Energy against the loop number for the soliton and Gaussian-soliton pulses (T_0=10ps)

This is confirmed in Figure 5.6, which shows the normalised pulse width versus the loop number for both the soliton and Gaussian-soliton pulse. Whereas the pulse width

of the soliton pulse generally increases, there is an initial contraction for the Gaussian-soliton pulse, which corresponds to the region in which its peak power remains relatively constant over the loop traversals.

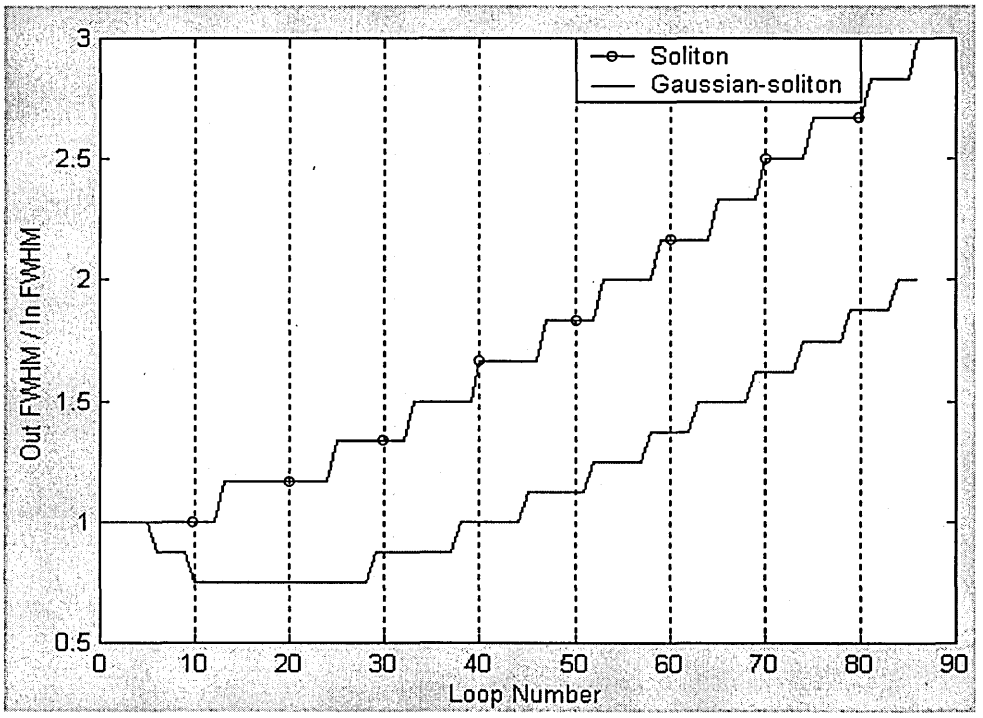

Figure 5.6 Normalised pulse width against the loop number for the soliton and Gaussian-soliton pulse types

5.4 OTDM System Employing a Passive RFLB

Figure 5.7 shows a block diagram of a typical OTDM transmission system employing an optical buffer. It consists of an OTDM transmitter, an additive white Gaussian noise (AWGN) channel, an all-optical demultiplexer, an optical buffer, an optical receiver, a matched filter and a detector. The transmitter, which consists of a continuous wave laser source, M modulators and several lengths of fibre, is used to produce the OTDM packets. The data signals produced by the first modulator (Mod 1) are not delayed and are used for packet delimiting purpose. The reader is asked to refer to Chapter 1 (section 4) for details about the operation of the transmitter. The AWGN channel is used to

account for the effect of noise on the OTDM signal as it traverses an optical path that is littered with optical amplifiers. The all-optical demultiplexer is an array architecture based on the terahertz optical asymmetric demultiplexer (TOAD), which was presented in Chapter 3. Each TOAD within the array is responsible for switching the incident data

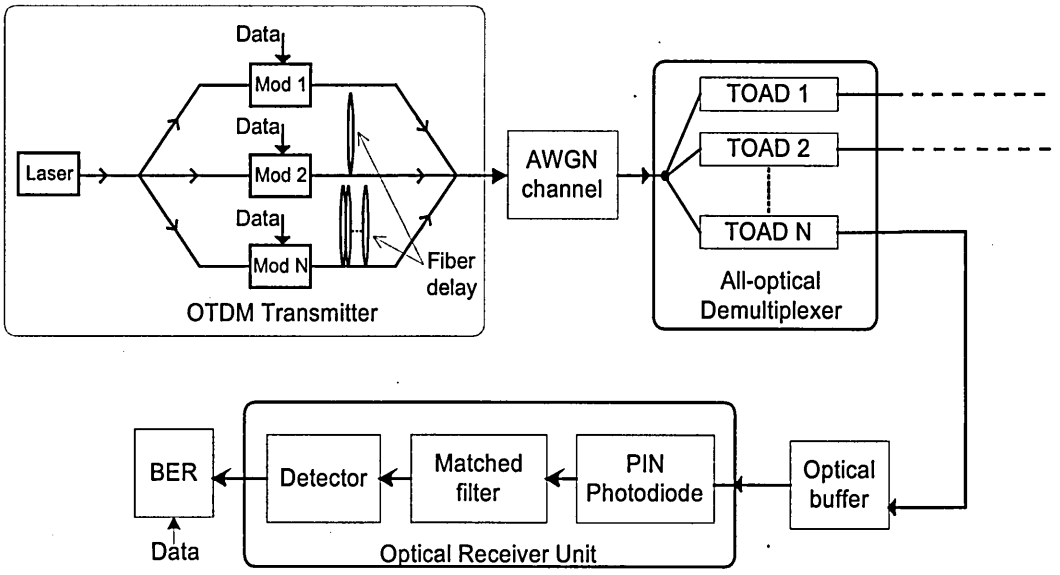

Figure 5.7 Block diagram of OTDM system. Mod *i* represents modulator *i*, *i* = 1,2,..,*N*

signals to the correct output port. The optical buffer, which provides an interface between the incident data signals and the receiver unit, acts as a flow control device to reduce the packet loss probability.

The optical receiver unit consists of a PIN photodiode, a matched filter and a detector. If the received voltage is above (/below) a predetermined threshold level, then the detector determines the logical identity of the received bit to be one (/zero). Finally, the BER unit compares the identity of the received bit stream with the associated data bit stream used to modulate the optical signal in the OTDM transmitter, to determine the ratio of incorrectly received bits to the number of bits transmitted.

The profiles of the pulses at various points within the OTDM system are presented in the next subsection. Thereafter, the BER performance of the buffer when placed within the OTDM system is examined as a function of the threshold detection level, input pulse profile, and delay. These results are considered over a range of SNRs. Finally, the effects of both the bit rate and buffer length on buffer capacity are highlighted. It is assumed that the photodetector is ideal with unity responsivity and that the noise added is representative of cumulative effects of the amplifier noise and other noise sources. Table 5.1 lists all the adopted simulation parameters. Under these conditions, $T_{loop} = 2.5$ μs and $M = 6250$ bits and $B = 2.5$ Gbit/s. This date rate is used throughout this section, unless otherwise stated.

5.4.1 Results

The proposed system shown in Figure 5.7 is simulated using the combination of an optical simulation software package and Matlab. Figure 5.8 shows the OTDM soliton waveform for a two-channel system. The data, in chronological order, for the first and second channel (i.e. '1,1' and '0'1') are shown in Figures 5.8(a) and 5.8(b), respectively.

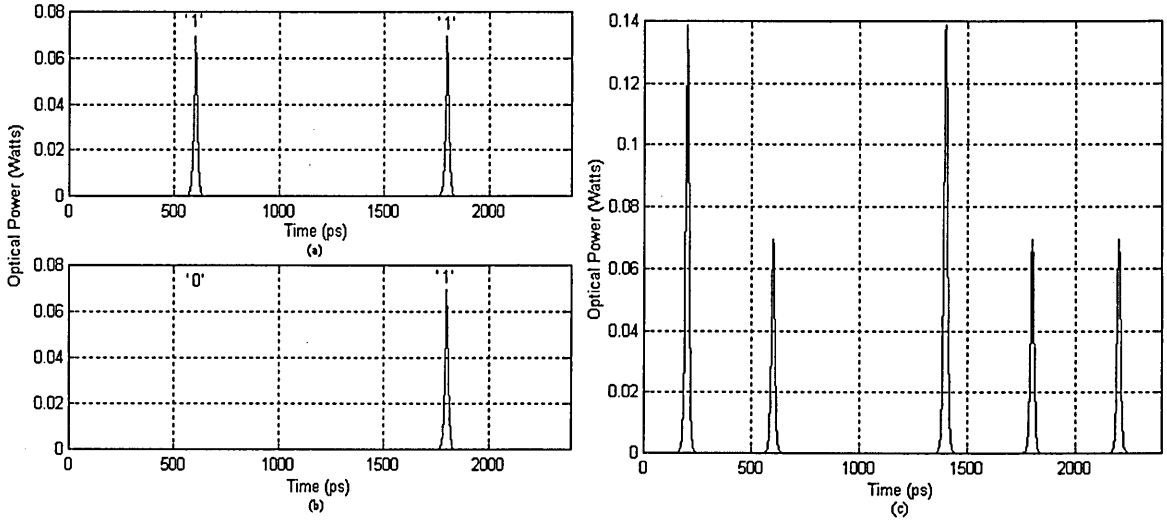

Figure 5.8 Waveforms associated with OTDM source: (a) modulated data train for first channel, (b) modulated data train for second channel, and (c) transmitted OTDM waveforms

Note that each frame in the OTDM signal is initiated with a high intensity clock pulse in order to provide the necessary frame synchronisation (see Figure 5.8 (c)).

The intensity of the clock pulses was heuristically chosen to be twice that of the payload to highlight the frame boundaries. The data and frame rates that result from the multiplexing of the lower bit rate channels are 2.5 Gbit/s and 833 Mbit/s, respectively.

After the AWGN channel, the OTDM signal is demultiplexed using a TOAD array and the waveforms observed are shown in Figure 5.9. As expected the waveforms have the same profile as that of the transmitter, but suffer from attenuation, dispersion and noise. Making minor modifications to the function generator within the modulators at the transmitter generates Gaussian shaped pulse train.

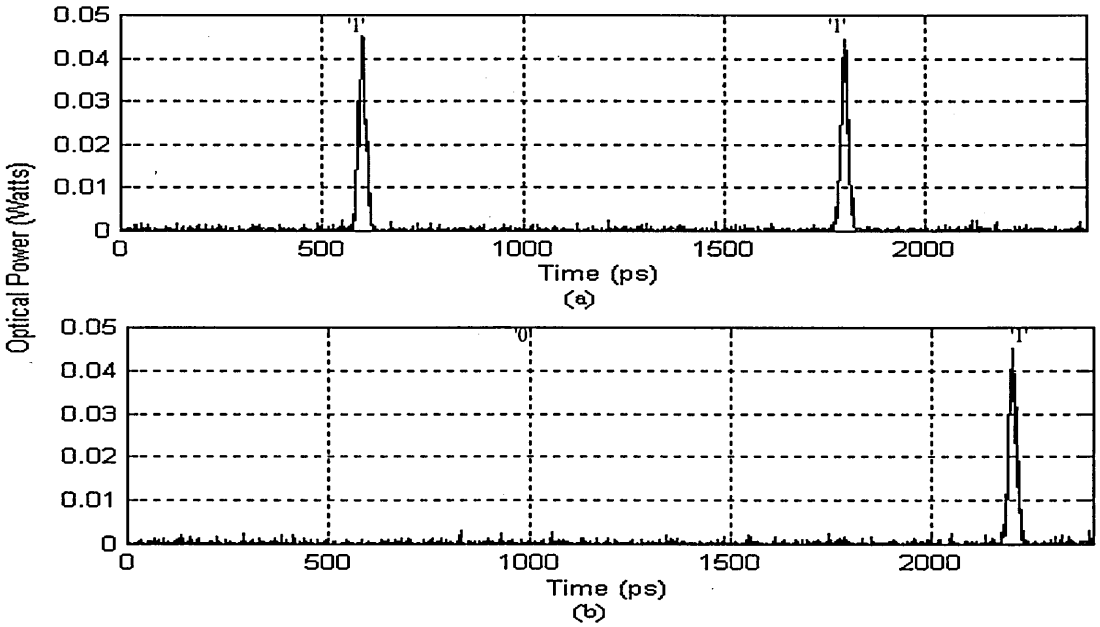

Figure 5.9 Received waveforms: (a) first channel, and (b) second channel

Figure 5.10 shows the BER versus signal-to-noise ratio (SNR) at different detector threshold levels for unbuffered soliton transmission. As can be seen, the best performance is achieved at an optimum threshold level, set midway (50%) between the maximum and minimum signal level at the output of the matched filter. At BER of

$1x10^{-3}$, an additional ~0.4 dB and ~1 dB are required if the threshold value is set 5% and 10% below or above the optimum level, respectively. Due to limited computational resources the lowest BER performance is approximately $1x10^{-4}$. The performance for the optimum threshold case is similar to the predicted result for the on-off-keying (OOK) system.

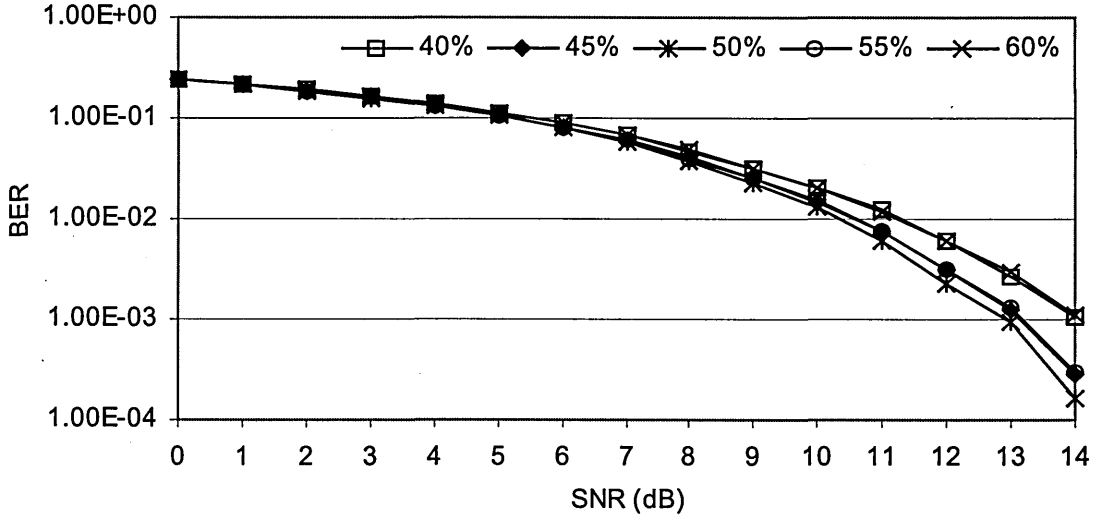

Figure 5.10 BER against the SNR for un-buffered soliton transmission at different threshold levels

Figure 5.11 shows the eye diagrams of the received data signals for a buffered and unbuffered soliton pulse (T_0 = 10 ps) at SNR of 10 dB, respectively. In Figure 5.11 (a), the number of loop circulation is 20, which results in a reduced SNR and therefore a reduced eye opening compared with Figure 5.11 (b).

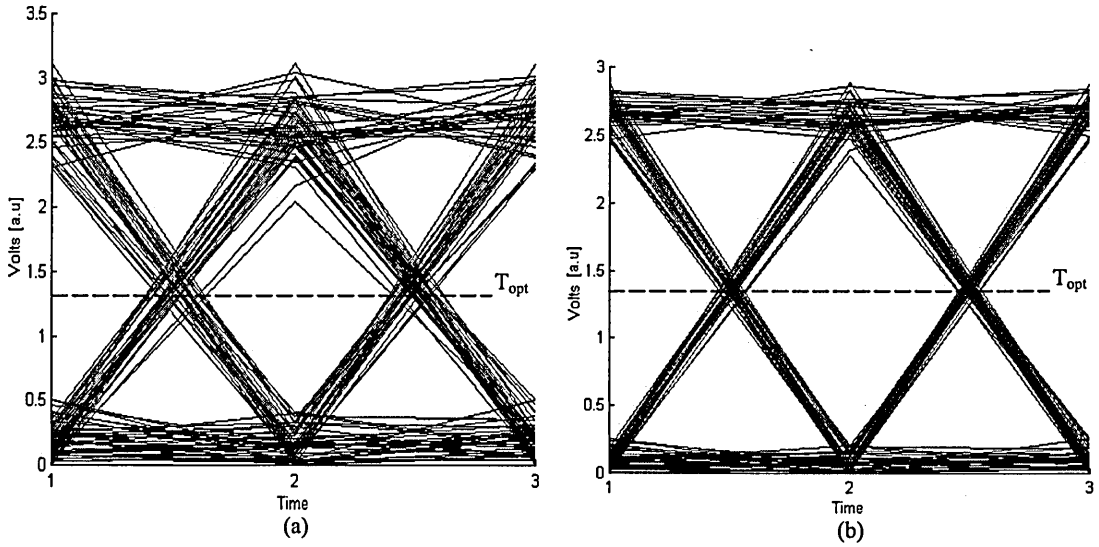

Figure 5.11 Eye diagrams for received voltage: (a) buffered, and (b) unbuffered

An important feature of the eye diagram is that it may be employed as a tool to gauge the optimal threshold level setting. Careful examination of these diagrams confirms T_{opt} to be half of the maximum eye opening for both cases. Note that this value is expected to shift slightly in the presence of thermal and shot noise [125]. In particular, as shot noise is more prominent on 1-bits, T_{opt} will generally be lower than half of the maximum eye opening

5.4.2 BER performance

For B = 2.5 Gbit/s, the BER performance versus the SNR for different buffer circulation loop numbers for soliton and Gaussian-soliton shaped pulses are shown in Figures 5.12 and 5.13, respectively. In each case, both 10 and 40 ps pulse widths are considered.

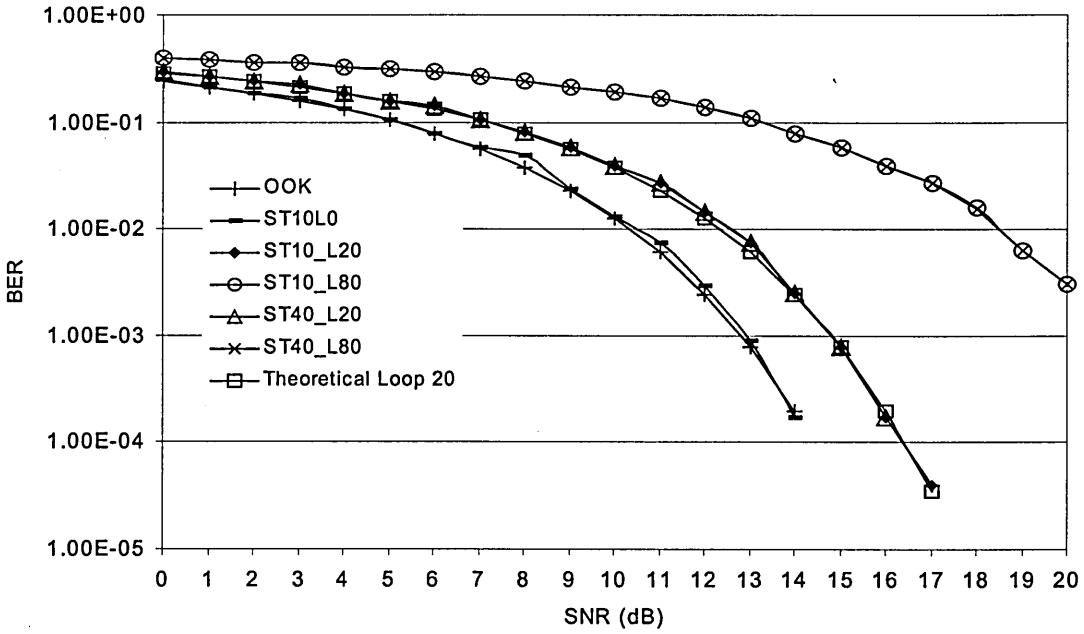

Figure 5.12 BER against the SNR for soliton transmission over a range of loop traversals

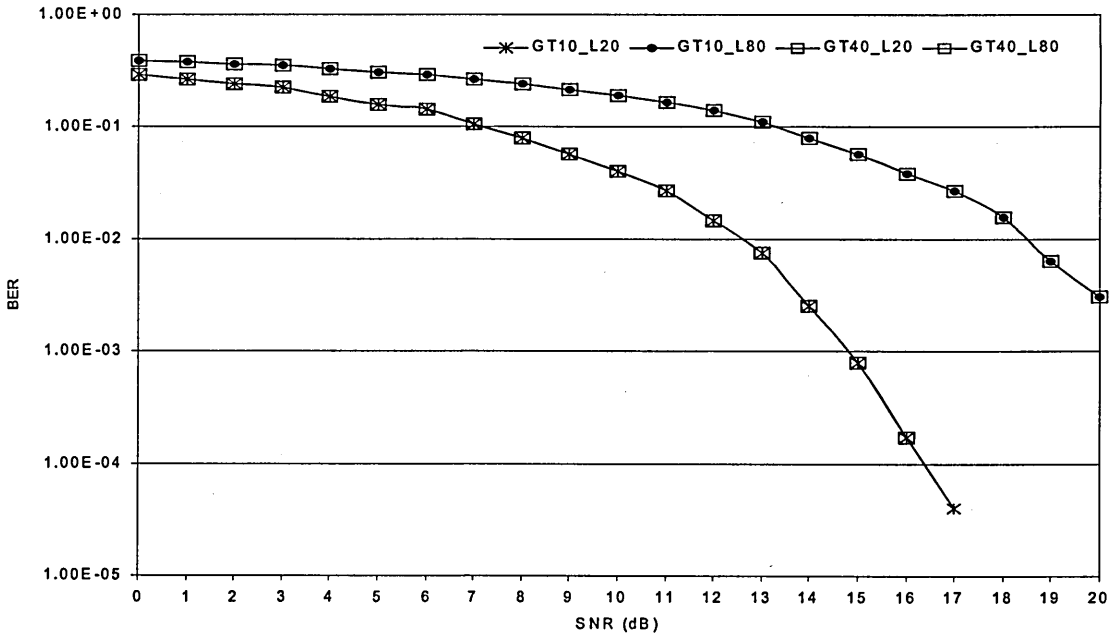

Figure 5.13 BER against the SNR for Gaussian-soliton transmission over a range of loop traversals

For comparison, the theoretical BER performance for unbuffered and buffered (loop number = 20) OOK is also shown. Note that for convenience, the longer delay instances are taken relative to the unbuffered OOK case to highlight the performance degradation with increasing loop number. For a clear description of the curve legends refer to Table 5.2.

Table 5.2 Key for legends in Figures 5.12 and 5.13

Legend	Meaning
OOK	On-Off-Keying
ST10L0	Soliton Shaped Pulse (T_0=10ps), (unbuffered)
ST10L20	Soliton Shaped Pulse (T_0=10ps), Loop number 20
GT10L20	Gaussian Shaped Pulse (T_0=10ps), Loop number 20
ST10L80	Soliton Shaped Pulse (T_0=10ps), Loop number 80
GT10L80	Gaussian Shaped Pulse (T_0=10ps), Loop number 80
ST40L20	Soliton Shaped Pulse (T_0=40ps), Loop number 20
GT40L20	Gaussian Shaped Pulse (T_0=40ps), Loop number 20
ST40L80	Soliton Shaped Pulse (T_0=40ps), Loop number 80
GT40L80	Gaussian Shaped Pulse (T_0=40ps), Loop number 80

For the unbuffered case in Figure 5.12, the 10 ps soliton pulse displays a performance that is identical to OOK. However, the BER performance degrades significantly as the number of loop circulation increases. For example, for BER of 10^{-4}, the SNR penalty for 20 loop traversals is about 2 dB compared with the unbuffered case. Moreover, there is a 6 dB power penalty between loop circulation numbers 20 and 80.

It can be shown (see Appendix C) that the BER for a given loop number may be defined as:

$$P_b(l_n) = Q\left(\sqrt{\frac{E_0 e^{-\alpha_l l_n}}{2N_0}}\right), \tag{5.7}$$

where E_0 is the signal energy of the received unbuffered pulse and N_0 is the noise power spectral density. Note that when the number of loop traversals is zero (i.e. $l_n = 0$), the expression is identical to that for OOK [126]. Comparing Figures 5.12 and 5.13 reveals that the performance of the soliton pulse is virtually the same as the Gaussian-soliton shaped pulse. In addition, the performance at a given loop circulation number is the same for the 10 and 40 ps pulse widths regardless of the input shape pulse. While larger pulse widths facilitate less complex synchronisation procedures, they become a limiting factor when the data rate is increased. That is, as the data rate is increased the shorter pulse widths would be a definite asset, as this would minimise the crosstalk between neighbouring pulses, which degrades the overall system performance.

Figure 5.14 shows the BER as a function of loop number for SNR = 15 dB and 40 ps pulse width for both soliton and Gaussian-soliton pulses. Due to limited computational resources the performance for loop numbers 0-4 could not be obtained. As can be seen, the BER performance is the same for both cases; they increase exponentially as the loop number increases.

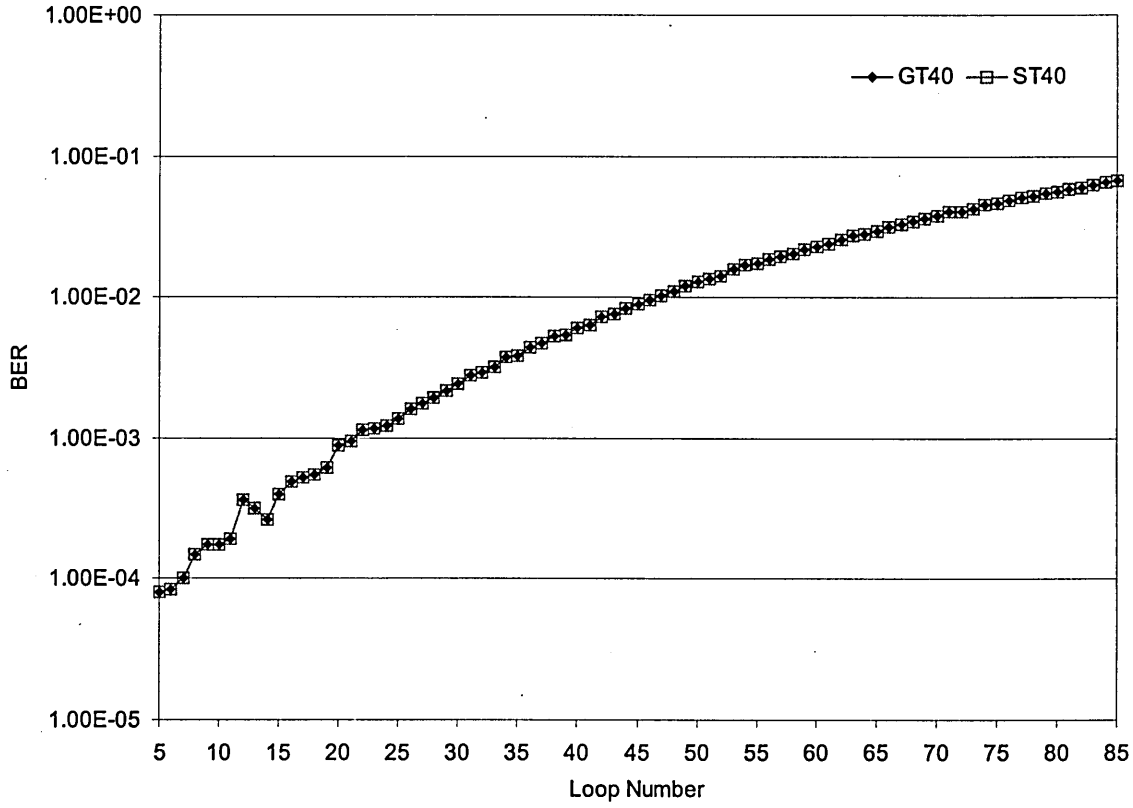

Figure 5.14 Buffer performance as a function of loop number for SNR = 15 dB, and pulse width of 40 ps

Lastly, for soliton pulse of 40 ps width, the BER versus SNR for 20 loop iterations at different data rates is shown in Figure 5.15. Notice that BER performance is the same for 2.5 Gbit/s and 5 Gbit/s, whereas at 10 Gbit/s, there is deterioration, due to intersymbol interference. For example, at BER of $1x10^{-3}$, 10 Gbit/s data rate requires an additional ~2 dB of SNR.

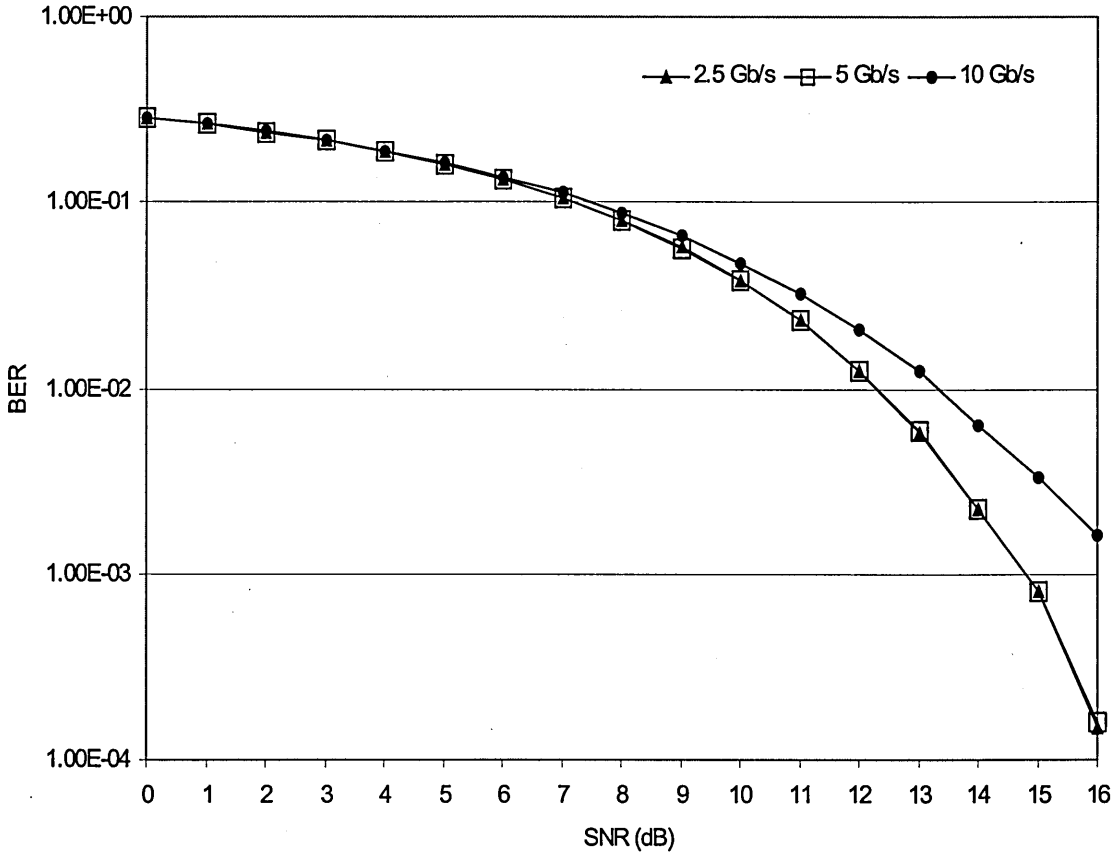

Figure 5.15 Buffer performance at different data rates using 40 ps soliton pulses

The case where the switch within the buffer is non-ideal with loss and crosstalk values of 1dB and 30 dB, respectively, has also been considered. Figure 5.16 shows the BER performance versus SNR for different unit loop lengths (L) at 2.5 Gbit/s. In each instance a total buffer delay of 10 μs is established by controlling the number of packet circulations.

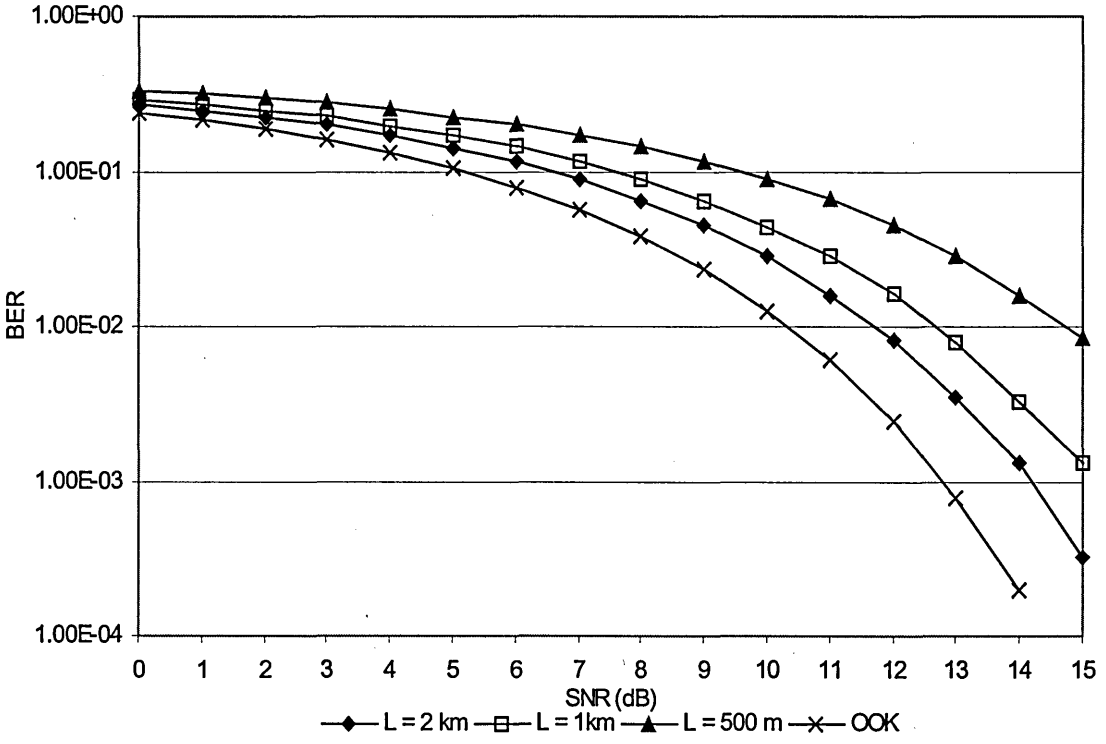

Figure 5.16 BER performance versus SNR for different unit buffer lengths (L)

The total buffer delay for each fibre lengh (i.e. $l_n \cdot T_{Loop}$) is 10 μs. For a given BER, the shorter buffer length (L = 500 m) requires higher SNR. This is because of the increased number of loop traversals (in this case it is 4). As the loop length increases the number of times the signal passes through the switch reduces, thus resulting in improved performance.

According to (5.2), increasing the data rate and fibre length results in a greater buffer capacity. This is shown in Figure 5.17 where the size of the packet was arbitrarily chosen to be 3 bits long; one bit each of the header, address and payload. Moreover, for a data rate of 10 Gbit/s; increasing the buffer length from 500 m to 2 km results in the quadrupling of the buffer capacity. However, it is not always advisable to increase

buffer capacity by increasing the data rate alone, as pulse interactions and crosstalk degrade performance and impose an additional penalty, about 2 dB in the case of Figure 5.16.

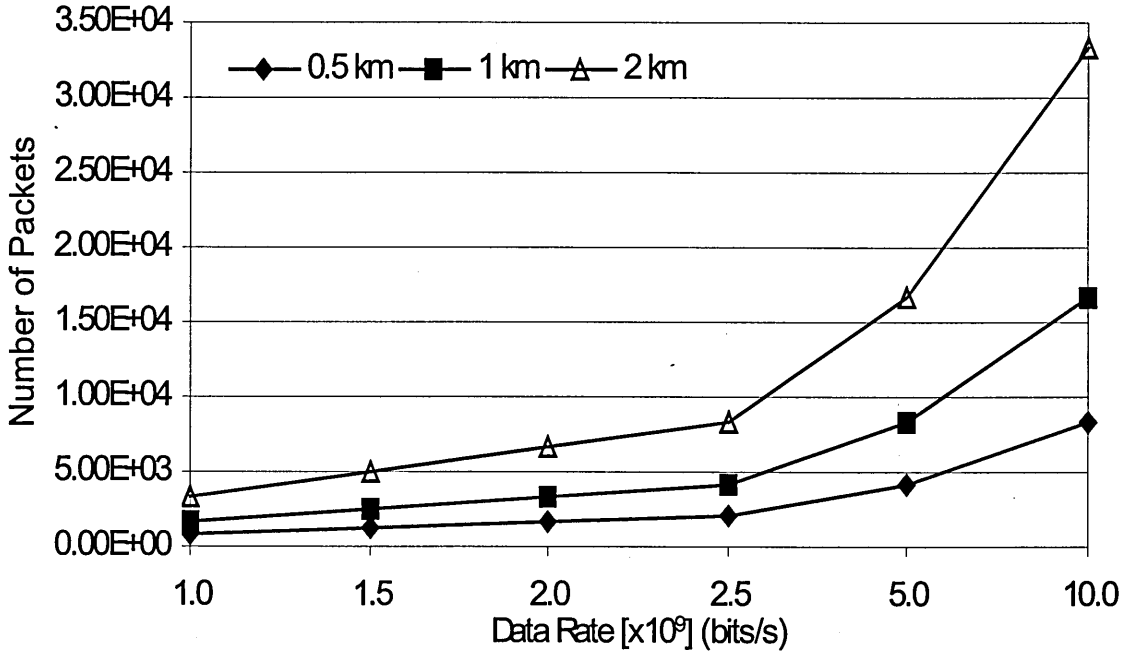

Figure 5.17 Number of packets vs. Data rate for buffer lengths of 0.5 km, 1 km and 2 km. Packet size is three bits.

5.5 Performance Dependence on the Dispersive Fibre Property

In Chapter 4 we noted the relationship between the peak power of the launched soliton pulses, the soliton number, the pulse width and the first order dispersion parameter. For convenience equation 4.42 is rearranged and reproduced below:

$$P_0 = \frac{3.108 \cdot \overline{N}^2 \cdot |\beta_2|}{\gamma \cdot T_{FWHM}^2} \tag{5.8}$$

It is evident that employing dispersion-shifted fibre (DSF), which has a lower dispersion parameter value, reduces the required peak power. For example, if $|\beta_2|$ in Table 5.1 is reduced to -1 ps^2 km^{-1} then the peak power changes from 69.4 mW to 3.86 mW given that the calculated non-linear coefficient is 2.59 W^{-1} Km^{-1}, $\overline{N} = 1$ and $T_{FWHM} = 17.63$ ps.

To investigate the inherent effect of using DSF the communication system model shown in Figure 5.18 was simulated using the VPI simulation software package, with the key parameters listed in Table 5.3. The simulation package uses proven mathematical models to define the operations of each of the devices employed within the transmission system. Consequently, for practical input parameters matching the physical characteristics of each device, the simulated results are accurate and experimentally reproducible. However, as the chosen soliton source and clock recovery unit parameters reflect ideal devices, the simulated results are generally expected to be better than those produced experimentally.

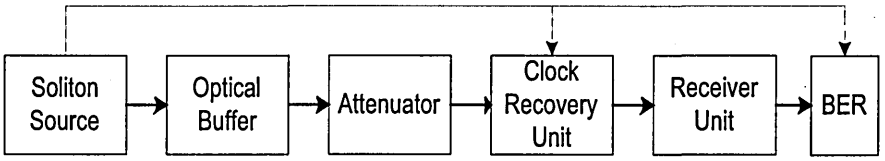

Figure 5.18 Block diagram of passive RFLB system model

The model consists of an optical source, which generates fundamental soliton pulses ($\overline{N} = 1$), a passive optical buffer, an attenuator, a clock recovery unit, an optical receiver unit, a detector and finally a BER module. The attenuator is used to obtain the BER performance over a range of receiver sensitivity values. The clock extractor determines the timing delay between transmitting and received signals for

synchronisation purposes. The receiver unit consists of an ideal PIN photodetector (i.e. unity responsivity), followed by a third order electrical low-pass Bessel filter. The order and type of filter is chosen to avoid pulse shape and phase distortions. The transfer function of the filter is defined by [126]:

$$H(p) = \frac{15}{15p^3 + 6p^2 + 15p + 15}, \tag{5.9}$$

with $p = i \cdot f / f_{3\mathrm{dB}}$, where f_{3dB} is the cut off frequency of the filter. These filter types are inherently linear, and consequently preservation of the wave shape of the filtered signal in the pass-band is possible.

Table 5.3 Simulation parameters for the passive RFLB fibre type investigation

Parameter	**Values**
Wavelength of signal (λ_s)	1.55 μm
Speed of light (c)	3×10^8 ms^{-1}
Effective fibre core area (A_{eff})	50 μm^2
Loop unit length (L)	500 m
First order dispersion coeff. (β_2) (Normal fibre)	-18 ps^2 km^{-1}
First order dispersion coeff. (β_2) (DSF fibre)	-1 ps^2 km^{-1}
Fibre loss parameter (α_{dB})	0.2 dB km^{-1}
Packet size	500 bits
Non-linear coeff. (γ)	2.59 W^{-1} km^{-1}
Data rate	20 Gb/s
Pulse shape	Soliton
Pulse width (T_0)	5
Switch insertion loss	1 dB
Switch Crosstalk	30 dB

First, note that from this point onwards the BER performance curves for the buffered instances are no longer relative to the unbuffered case. This allows for easier observation of the deterioration effects by visual inspection when they are not induced

solely by the intrinsic fibre loss. Second, the SNR reference criteria (i.e. x-axis) is now replaced by the receiver sensitivity. This is due to the nature of the simulation package.

Figures 5.19(a) and 5.19(b) show the BER performance versus the receiver sensitivity over a range of loop numbers for the passive RFLB employing both standard and DSF fibres, respectively. In the case of normal fibre, for a BER of 10^{-9}, a power penalty of ~0.8 dB, ~1.6dB, and ~2.6 dB is observed at loop numbers 15, 20 and 25, respectively.

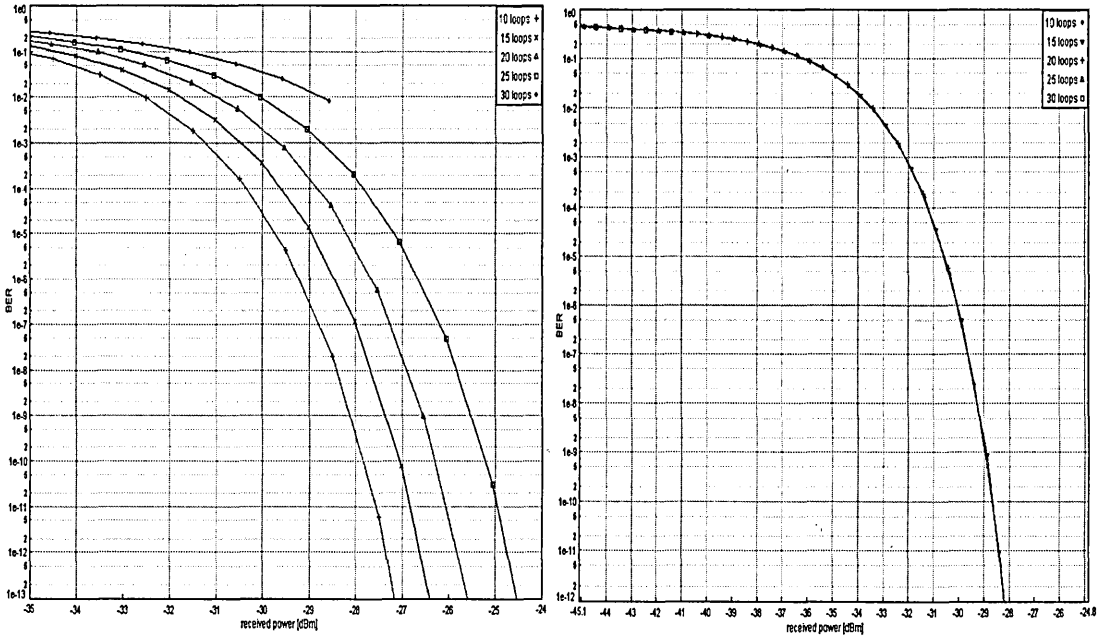

(a) (b)

Figure 5.19 BER against the received power for various loop traversals of the passive RFLB using (a) normal fibre, and (b) DSF fibre

Conversely, when DSF fibre is employed for the same BER the receiver sensitivity is -29 dBm, which is 0.8 dB better than the best case in Figure 5.19 (a), and it shows no observable power penalty over the same loop numbers as in Figure 5.19(a). The relatively poorer BER performance of the buffer employing normal fibre can be traced to the ISI caused by the broadening of the soliton pulse as it traverses the loop. For soliton transmission the dispersion length for buffers employing normal and the DSF

fibres are ~1.39 km and 25 km, respectively. As the rate of pulse broadening is related to the reciprocal of the dispersion length, pulses with lower dispersion lengths experience faster broadening rates [126]. This is evident from the eye diagrams, shown in Figure 5.20 for 15 loop traversals using normal fibre and DSF fibre. Observe that the ISI, which manifests itself as the pulse spreading outside of the bit period, is significantly reduced when DSF fibre is employed.

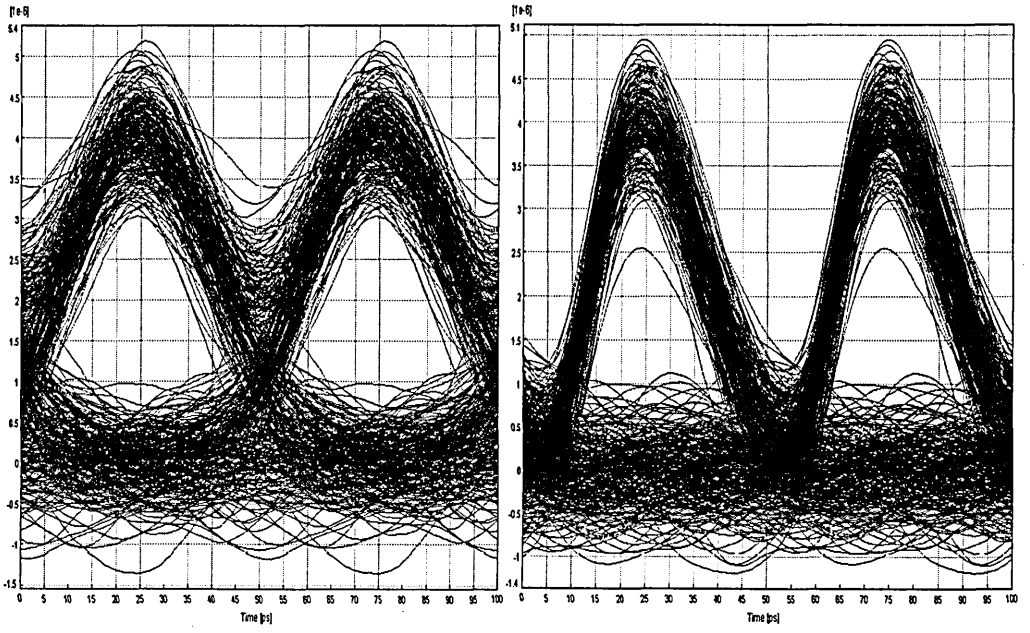

Figure 5.20 Eye diagrams for the passive RFLB after 15 loop traversals for (a) normal fibre, and (b) DSF fibre

5.6 Performance Dependence on the Data Rate

The investigation of the effect of data rate on the BER performance employs the same system model identified in Figure 5.18 and the parameters listed in Table 5.3. In this instance, the switch is again assumed to be ideal with negligible insertion and crosstalk losses. This ensures that the BER performance characteristics are due to the variation of

the data rate alone as it excludes any external factors. This assumption is removed in the subsequent chapters.

For the passive RFLB with loop numbers of 20 and 40, the BER performance versus the receiver sensitivity for different data rates is shown in Figure 5.21. For comparison purposes, the ratio of bit period to pulse width (T_B/T_0) of the launched pulses is kept at 10%. As expected, the BER performance deteriorates as the loop number increases. For example, at BER = 10^{-9} for the data rate of 20 Gbit/s, there is a power penalty of ~1.1 dBm when increasing the loop number from 20 to 40. More specifically, at BER of 10^{-9} the power penalty changes from being insignificant at 5 Gbit/s, to ~0.3 and ~1.1 dBm for the data rates of 10 and 20 Gbit/s, respectively. This is because dispersion becomes the critical limiting factor at higher data rates and higher loop numbers.

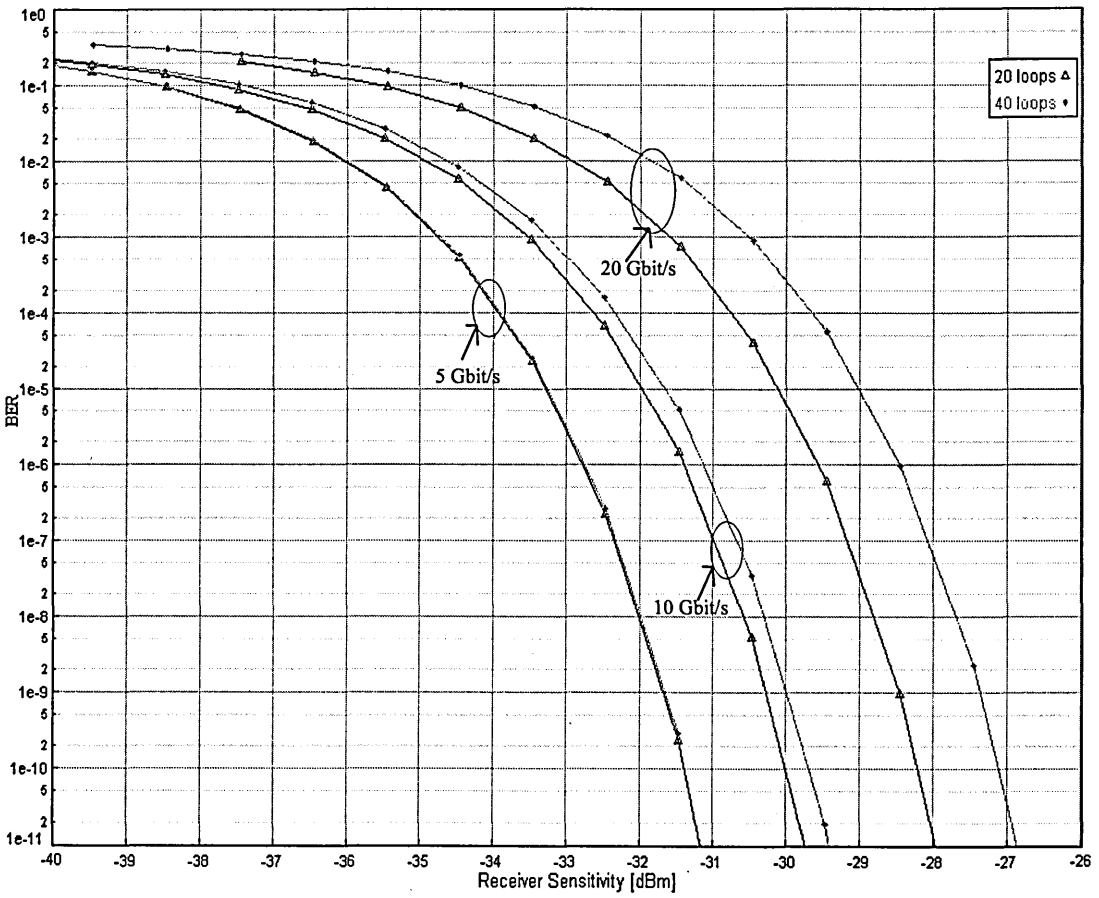

Figure 5.21 BER against the receiver sensitivity at different data rates

5.7 Summary

In this chapter, the propagation of both standard soliton and the Gaussian-soliton shaped pulses within a recirculating fibre loop buffer were examined. It is believed that this is the first time Gaussian-soliton pulses are considered for the transmission of OTDM signals within a communication system. The simulation model is based on the non-linear Schrödinger equation (NLSE) and accounts for fibre loss within the communications channel. Simulation results for BER performance at different buffer loop numbers and eye diagrams for buffered and unbuffered cases were presented. The simulation results indicated that in high-speed soliton transmission it is not necessary to

lunch soliton shaped pulse, defined by the *sech* function, into the fibre. Employing a Gaussian shaped pulse with the $\overline{N} = 1$ would give the same performance as that of the soliton case. This is because the Gaussian pulse evolves asymptotically into a fundamental soliton. Moreover, for a given delay the buffer could be engineered such that optimal performance is achieved. For the buffer architecture with an ideal switching, simulation results showed that the system imposes a 1 dB penalty for every 10 loop traversals. Further investigations also highlighted the relationships between the BER performance and both fibre type and system data rate.

The inclusion of an active element within the loop to extend the delay storage times is the emphasis of the next chapter

Chapter 6

The Active Recirculating Fibre Loop Buffer (RFLB)

6.1 Introduction

In the previous chapter, chromatic dispersion and intrinsic fibre loss were identified as the main BER performance delimiters for the passive RFLB. To counter the latter, an amplifying element may be introduced into to loop to compensate for the inherent losses within the system, thereby increasing the buffer storage time. In this chapter such a buffering architecture is investigated and its BER performance is mathematically characterised for several storage times. An application for such a buffer and the buffer model are presented in section 6.2, where the inherent performance inhibitors are also considered. The effects of storage time, amplification period and fibre-type on the BER are investigated in sections 6.3 and 6.4, respectively. Thereafter, the mathematical model is then developed in section 6.5. The effects of switch loss, and in-loop filtering to reduce amplifier spontaneous emission (ASE) accumulation are considered in sections 6.6 and 6.7, respectively. Finally, the chapter concludes with a summary in section 6.8.

6.2 The Active Recirculating Fibre Loop Buffer

Photonic networks are viewed as excellent candidates for supplying the required bandwidth as the signal remains in the optical domain during propagation thereby. The Manhattan Street Network, shown in Figure 6.1, is a popular example of a symmetric photonic network topology, which employs a simple self-routing scheme. This facilitates the use of a simple addressing scheme resulting in low packet processing overheads, making it ideal for an all-optical buffering solution. Traditionally, such networks use 'hot potato routing', which is a special case of deflection routing with no buffering, to handle contention resolution. In essence, when a contention occurs, all but one of the offending packets is misrouted resulting in an increase in their propagation time. Hence for each source-destination pair the number of hops is not fixed and the entire networks essentially acts as a large optical buffer. Consider the case were two packets A and B destined for node '01' simultaneously arrive at node '00'. Packet A, may be forwarded to its destination but packet B must at least traverse a minimum path distance of four hops, (e.g. nodes '10', '20', '30'and finally '00'), before it can be routed to the desired destination node.

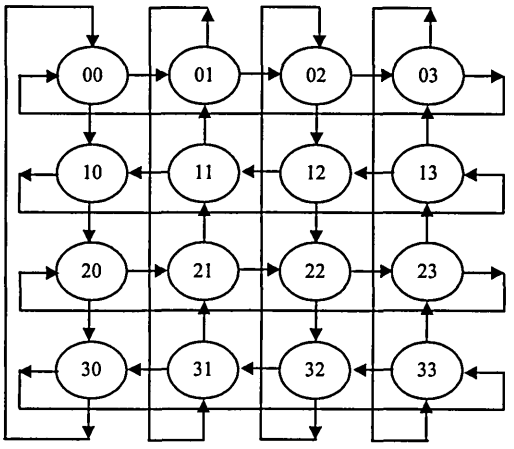

Figure 6.1 4x4 Manhattan street network photonic network topology

The introducing of limited buffering capacity locally at each node, has been shown to increase the throughput of the system [39]. Moreover, packets have a higher probability of traversing between the source-destination pair using minimum number of hops. While increasing the buffer depth beyond a critical value does not improve the throughput performance [39], it would allow for limited priority routing capability.

In contrast to [40], [127] where a length of fibre is used as the buffer, the use of an active recirculating fibre loop buffer, see Figure 6.2, may be employed to increase the flexibility. Again, pulses entering the buffer via path AB will continue to circulate until the time that they are ready to be switched out via path BC.

Conversely, unbuffered pulses travel along the path AC. As in the case of the passive RFLB, the maximum delay per loop traversal T_{loop} for a given length of fibre L, is as given by equation (5.1) in the previous chapter.

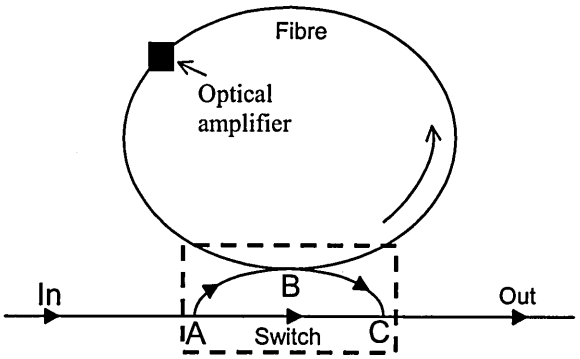

Figure 6.2 Active RFLB

The optical amplifier is employed to compensate for any system losses and to maintain the peak intensity necessary for soliton propagation [128]. Note however, that infinite storage times are not achievable in such a buffer structure primarily because the

amplified spontaneous emission noise that accumulates on each circulation serves to degrade the SNR. Furthermore, Gordon and Haus showed that the continual amplification of optical pulses within a long-haul communication link results in a pulse delay variance or oscillatory random walk behaviour, which directly affects the system performance [129]. More specifically, the generated ASE induces a random jitter of the central optical frequencies among individual soliton pulses, which is then transformed into timing jitter.

Filtering is the most common soliton-control technique employed to extend the Gordon-Haus limit. In essence, a band pass filter appropriately centred on the soliton spectrum effectively excludes the 'excess' noise outside the filter pass-band, thereby reducing ASE noise and timing jitter. However, the eventual ASE noise accumulation within the pass-band still becomes a BER performance-limiting factor. Moreover, bandwidth limited amplification with fixed centre frequency filters eventually leads to the soliton instability because the excess gain that must now be provided for the loss at the wings of the soliton spectrum also amplifies the co-existent linear waves. These unstable background linear waves serve to degrade the SNR and may destroy the soliton if their powers become comparable [130]. Sliding frequency filters are employed within some long-haul amplified communication links to account for the self induced Raman shift in the soliton centre frequency. The centre frequency of each post amplifier filter is progressively offset from the previous filter instance so that each filter effectively tracks the continual shift in the soliton central frequency [131-132]. In this scenario, the linear waves eventually become attenuated, as they do not track the centre frequency of the filter. Although this prevents the eventual filtering of the soliton signal itself due to misalignments, ASE noise still accumulates within the 'tracking' pass-band and continues to be primary performance delimiter.

Another jitter reduction technique involves the use of dispersion management systems [133-135] as described in Chapter 3. In essence, this technique diminishes the accumulated effect of fibre dispersion by making the average dispersion value as close to zero as possible. This mitigates the Gordon-Haus effect as chromatic dispersion is now minimised thereby reducing the relative group velocity spread of the propagating pulses within the soliton trains.

The final alternative is the use of more efficient optical amplification elements. More specifically, the Raman amplifiers, which have a lower noise figure than erbium doped fibre amplifiers (EDFAs) are known to produce much less ASE noise. Consequently, this translates into a corresponding decrease in timing jitter [136-137].

In [138], Marcuse extends the original work done by Gordon and Haus to derive an expression for the pulse delay variance in real as opposed to soliton units. For a periodically amplified communication link, the delay variance is defined by [138]:

$$\left\langle \delta t_{N_A}^2 \right\rangle = \frac{2\pi n_2 |\beta_2| n_{sp} hc(G-1)L_{Tot}^3}{9T_0 \lambda_s^2 A_{eff} L_A Q}, \tag{6.1}$$

where n_{sp}, and G correspond to the spontaneous emission noise factor, and gain of the amplifier, respectively. L_{tot} and L_A are the total distance and amplification period, respectively. Finally, N_A, λ, h are the number of amplifiers, the carrier wavelength and Planck's constant, respectively. The Q term is a measure of the effective length and is defined by [138]:

$$Q = \frac{\alpha \cdot L_A}{1 - e^{-\alpha \cdot L_A}}. \tag{6.2}$$

Figure 6.3 shows the normalised root-mean-squared timing jitter and the jitter tolerance for the active RFLB as a function of loop number for the conditions listed in Table 6-1. The jitter tolerance is defined as the product of the RMS timing jitter, the normalised pulse width T_0 and the data rate (B = 20 Gbit/s) [11]. For comparison, two different fibre types, namely normal and dispersion-shifted fibre, and several pulse widths are considered. Note that in each case L_A is taken to be 500 m, and G exactly compensates for the fibre loss as well as the insertion and crosstalk switch losses.

Table 6-1 Numerical parameters for timing jitter

Parameter	Values
Wavelength of signal (λ_s)	1.55 μm
Speed of light (c)	3×10^8 ms^{-1}
Planck's constant (h)	6.626×10^{-34} Js
Effective fibre core area (A_{eff})	50 μm^2
Amplification period (L_A)	500 m
First order dispersion coeff. (β_2) (Normal fibre)	-18 ps^2 km^{-1}
First order dispersion coeff. (β_2) (DSF fibre)	-1 ps^2 km^{-1}
Fibre loss parameter (α_{dB})	0.2 dB km^{-1}
Non-linear coeff. (γ)	2.59 W^{-1} km^{-1}
Pulse width (T_{FWHM})	8.82, 4.41, 1 ps
Switch insertion loss	1 dB
Switch crosstalk	30 dB

Figure 6.3(a) highlights that the RMS timing jitter is more prominent when the pulse width is very narrow (i.e. 1 ps). Additionally, DSF systems experience less timing jitter

than those employing normal fibre. In Figure 6.3(b), the worse case jitter tolerance for the normal fibre is ~55% of the bit period at $l_n = 400$ when the pulse width is 1 ps. This would result in severe BER performance degradation.

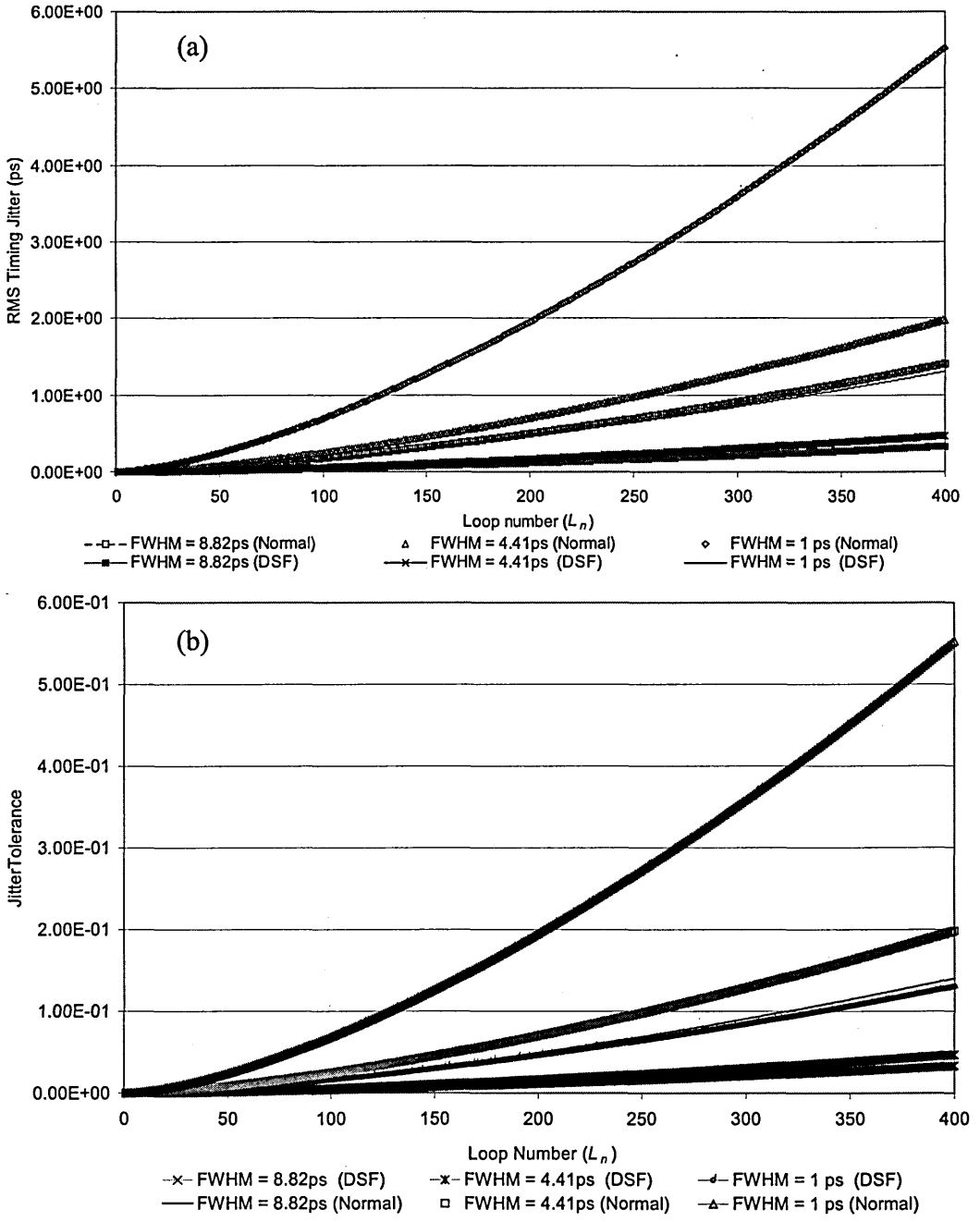

Figure 6.3 (a) RMS timing jitter and (b) jitter tolerance against the loop number for normal (($\beta_2 = -18$ ps^{2}km^{-1}) and DSF ($\beta_2 = -1$ ps^{2}km^{-1})

For an acceptable jitter tolerance of ~10% [129], the system is limited to ~125 loops. Conversely, ~332 loops are possible for systems employing DSF for an equivalent 10% jitter tolerance. For our buffer simulations (T_{FWHM} =8.82 ps (DSF)), the timing jitter is less that 3.4% at $l_n = 400$, and is therefore negligible.

After each amplification stage, the soliton pulses undergo an adjustment period where the pulse width adapts itself to regain a fundamental soliton profile. During this period the solitons lose some of their energy as linear dispersive waves. The effect of these potentially hazardous waves critically relies on the relationship between the loss per dispersion length αL_D and the amplifier period L_A. Where the dispersion length L_D is given as:

$$L_D = T_0^2 / |\beta_2| \tag{6.3}$$

If both $\alpha L_D << 1$ and $L_A >> L_D$, the amplification regime is termed quasi-adiabatic. In this regime the soliton is capable of adjusting itself to the energy loss adiabatically (i.e. without a temperature change). Conversely, when $L_A << L_D$, the modus operandi is referred to as the average soliton regime. Here the soliton shape is not distorted significantly despite the energy loss and the pulses may consequently be amplified hundreds of times. The main disadvantage is that the relatively close amplifier spacing makes it unsuitable for long-haul high-bit rate (≥ 20 Gbit/s) communications. Note that in the quasi-adiabatic regime, continuous amplification of the soliton pulse stream eventually leads to signal degradation. This is due, to the interaction between the soliton pulse stream and the accumulation of the amplified dispersive waves formed when the solitons shed some of their energy. In this work both regimes will be considered, as the BER performance of the buffer will be compared for several amplification periods, when normal and DSF fibre are employed within the buffer architecture.

6.3 Effect of Amplification Period on BER Performance of Active RFLB

In this section, the increased storage times and lower power penalties achievable when in-loop amplification is employed is illustrated when the BER performance of passive and active buffering are compared. Additionally, the effect of amplification period on BER performance of Active RFLB will be highlighted. For easy comparison between the passive and active schemes the switch within the buffer architecture is initially assumed to have no insertion losses. The effect of the switch on soliton propagation is considered in section 6.4 and onwards.

Figure 6.4a shows the system model block diagram. Note that the internal configuration of the active optical buffer is shown in Figure 6.2. A description highlighting the function of each component is given in Chapter 5. The proposed system was simulated using the VPI Photonic simulation software (see Figure 6.4b) employing the key parameters are listed in Table 6-2. These parameters are chosen to first, match the physical device characteristics, and second, to ensure that the pulse width and data rate parameters allow for suitably spaced data pulses thereby avoiding soliton interactions during the high-speed communication. By default, quasi-adiabatic amplification is assumed under these conditions, as $\alpha L_D < 1$. However, the case where $L_A > L_D$ is also considered.

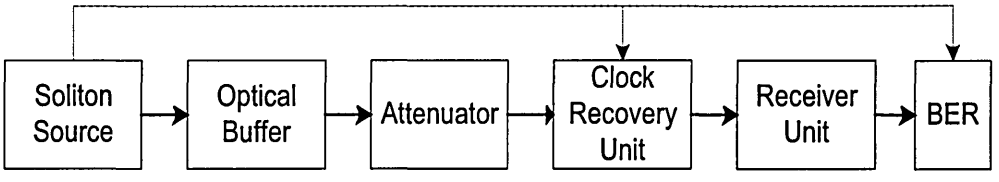

Figure 6.4a Block diagram of active RFLB system model

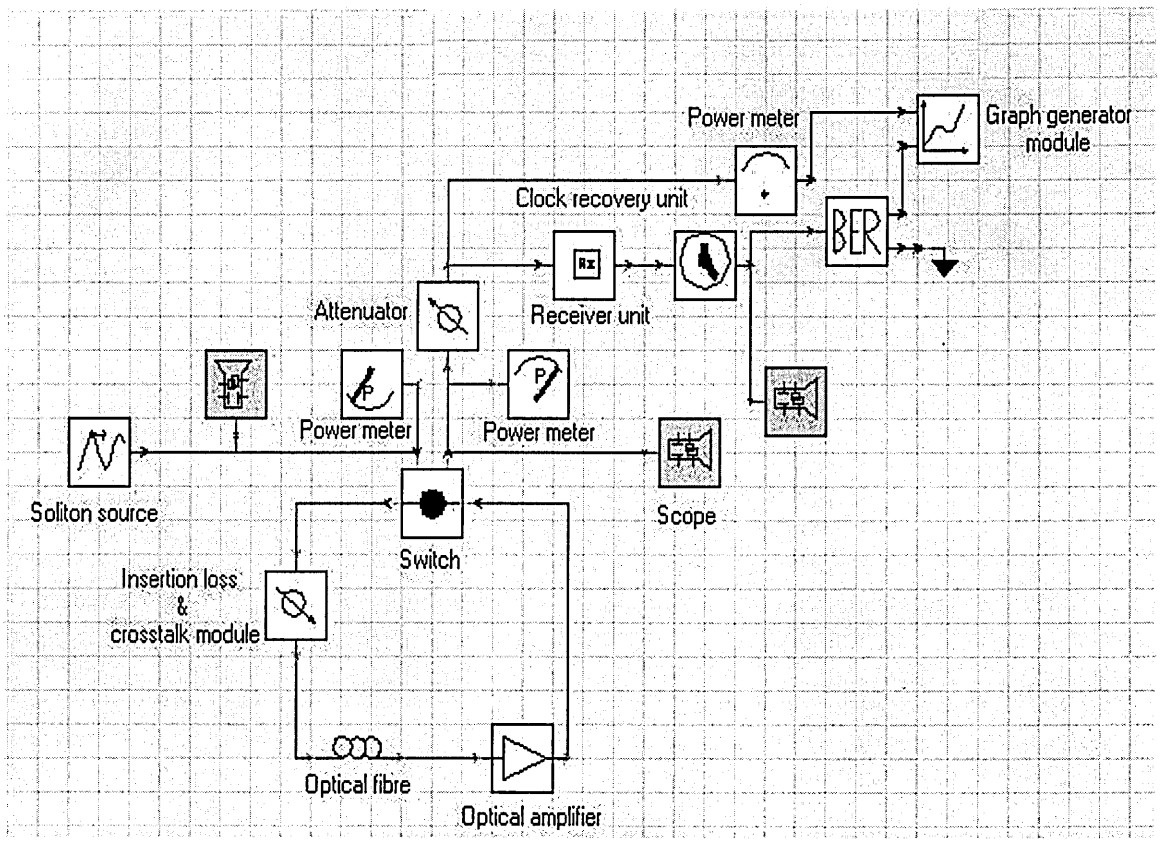

Figure 6.4b VPI Syetem design for active RFLB system model

Table 6-2 Simulation parameters for the active RFLB amplification period investigation

Parameter	Values
Wavelength of signal (λ_s)	1.55 μm
Speed of light (c)	$3x10^8$ ms^{-1}
Effective fibre core area (A_{eff})	50 μm^2
Loop unit length (L)	500 m
First order dispersion coeff. (β_2)	-18 ps^2 km^{-1}
Fibre loss parameter (α_{dB})	0.2 dB/km
Packet size	512 bits
Non-linear coeff. (γ)	2.59 W^{-1} km^{-1}
Data rate (s)	20 Gbit/s
Pulse shape	Soliton
Pulse width (T_0)	5 ps

For comparison, Figures 6.5(a) and (b) show the profile of the soliton waveform as it propagates within the passive and active RFLB, respectively. As established previously, the waveform within the passive RFLB attenuates exponentially and disperses as the number of circulations (loop number l_n) increases. Conversely, the peak amplitude within the active RFLB is maintained throughout the propagation period and the presence of ASE noise is also observed.

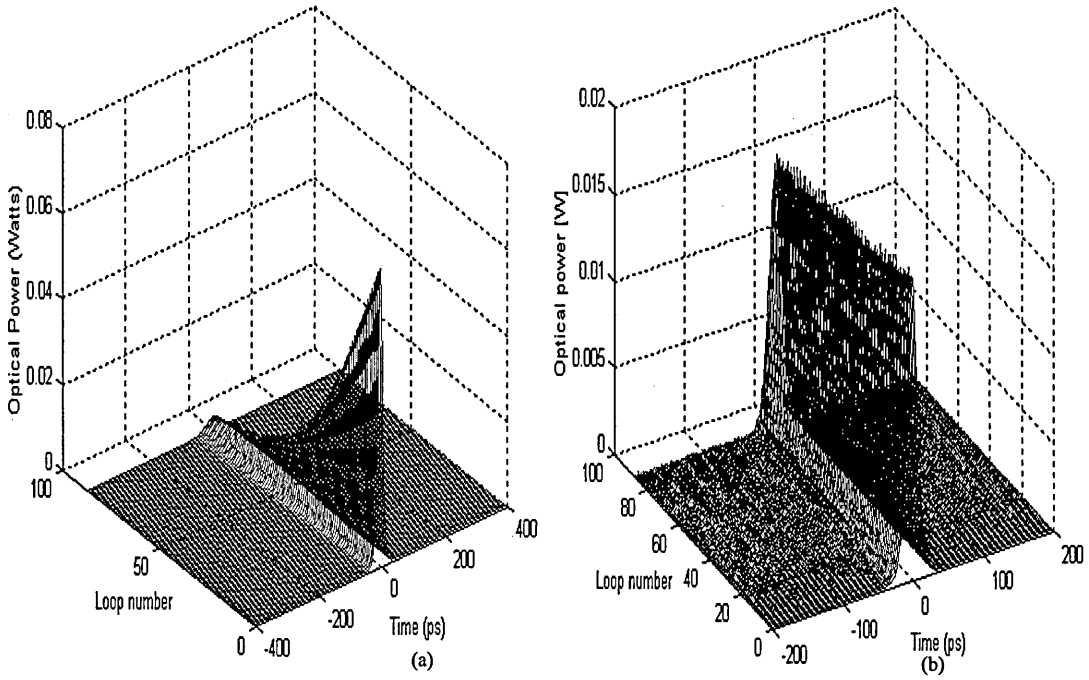

Figure 6.5 Power profile of soliton pulse (T_0=10 ps) , (a) in passive RFLB and (b) in active RFLB

For the passive RFLB operating data rate of 20 Gbit/s, the BER performance over a range of receiver sensitivities for different buffer circulation numbers (i.e. delay) is shown in Figure 6.6. As expected, the BER performance deteriorates as the loop number increases. For example, at BER of 10^{-9} there is a power penalty of ~1.1 dBm when increasing the loop number from 20 to 40.

Later the Figure 6.6 will be used to provide evidence of the advantage in employing active buffering.

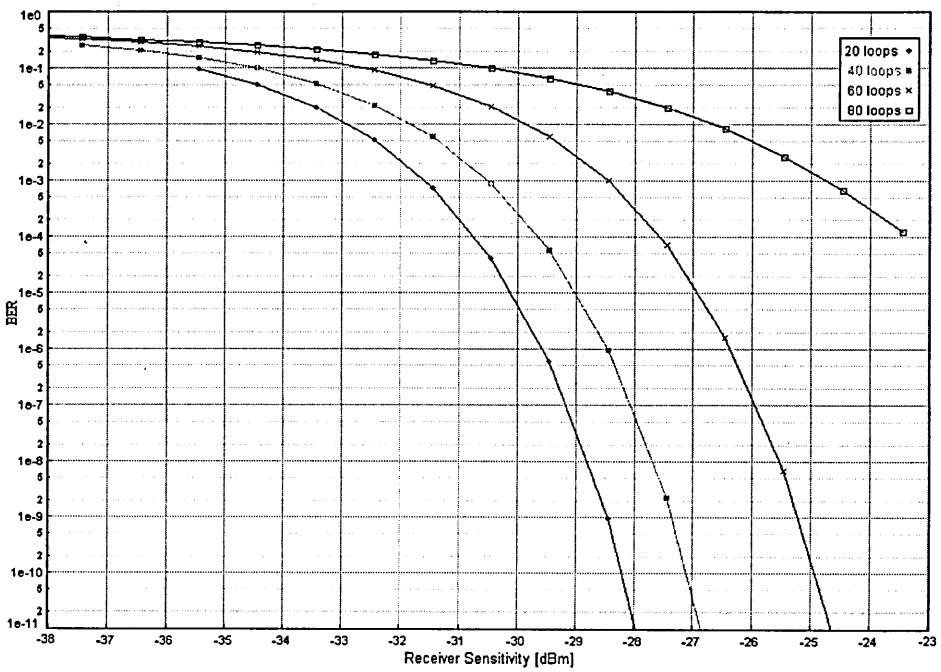

Figure 6.6 BER against the receiver sensitivity for different values of loop number and for a data rate of 20 Gbit/s

Figure 6.7 shows the BER performance of an active RFLB for different amplification periods L_A. Also shown for comparison is the result for the unbuffered case, which provides the best performance. This is as expected as the unbuffered pulses do not suffer from the inter-symbol-interference (ISI) and cumulative effects of ASE noise experiences by the buffered pulses as they circulate the buffer.

The results indicate that with active buffering, the best performance, compared with unbuffered, is achieved when the upper limit of the amplification period is L_A = 6 loops and the circulation time is 300 μs (20 passes). This is equivalent to 3 km, which is far less than the 22 km suggested in [11], [96]. Increasing the number of passes to 60, results in a significant deterioration of the BER performance. Observe that the relatively poor performance for the cases when L_A = 10 and 20 loops is caused by the crosstalk arising from ISI due to the pulse broadening before amplification. For these relatively large amplifications periods the performance degraded significantly due to ISI.

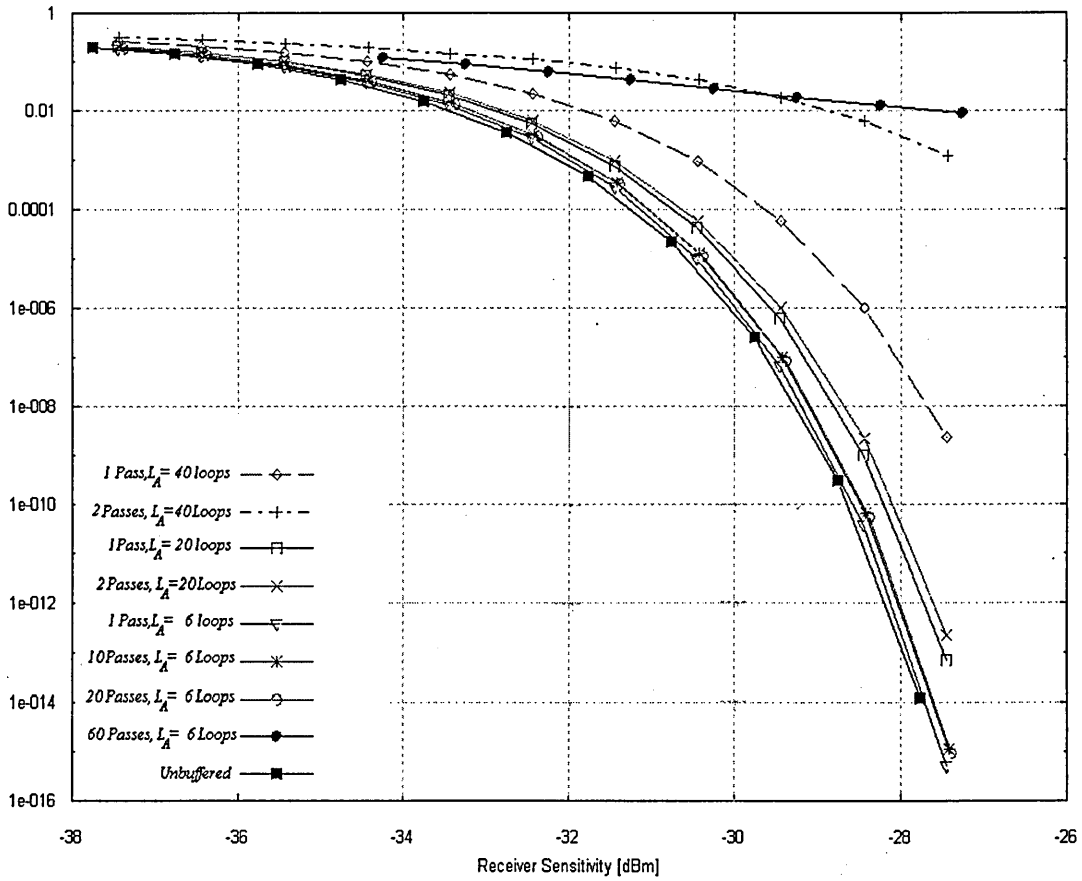

Figure 6.7 BER against the receiver sensitivity for buffered (active) and unbuffered cases

The benefit of employing active buffering can be observed by comparing Figures 6.6 and 6.7. The delay time for l_n = 60 loops in the passive RFLB is equivalent to the delay

time for 10 passes with L_A = 6 loops in the active RFLB, therefore these two plots are used to make a direct comparison. At BER of 10^{-9} the active buffer offers a ~3.4 dBm performance gain over the passive buffer. The additional gain can be utilised by increasing the buffered storage time.

6.4 Improving BER Performance Within Active RFLBs

In this section the focus is on improving the performances by employing dispersion-shifted fibre to reduce GVD. This will lead to an increase in the dispersion length such that $L_A << L_D$ therein effecting the transition to the average soliton regime. The system model and parameters described in section 6.3 are employed, with β_2 = -1 ps^2km^{-1} for DSF. Consequently, L_D is now 100 km. In this investigation, L_A is taken to be equivalent to 1-loop traversal (500 m), which is well below the upper 6-loop traversal limit determined in the previous section. Note that here the switch has an insertion loss of ~1 dB.

Figures 6.8 and 6.9 show the BER results of the active RFLB against the receiver sensitivity over a range of loop numbers for normal and DSF type fibres, respectively. For the active RFLB employing normal fibre, a power penalty of ~0.1 dB, 0.2 dB, and 0.3 dB is observed at BER of 10^{-9} for loop numbers 15, 20 and 25, respectively. These power penalties may be attributed to the continual amplification of the crosstalk due to ISI as the packet circulates within the buffer. Moreover, the relatively high powers required for soliton propagation within the normal fibre results in greater power penalties incurred from ASE noise induced fluctuations. For the active RFLB

employing DSF fibre, there is no noticeable power penalty at lower loop numbers, which suggest lower ASE noise penalties and reduced ISI. However, when the loop number is increased to 100 and 400, there is a ~0.25 and ~1.15 dB power penalty (at BER of 10^{-9}), respectively. This increase in power penalty is attributed to the build up of ASE noise and the switch altering the soliton dynamics due to its inherent insertion loss property. These two factors are the subjects of the section 6.5 and 6.6, respectively.

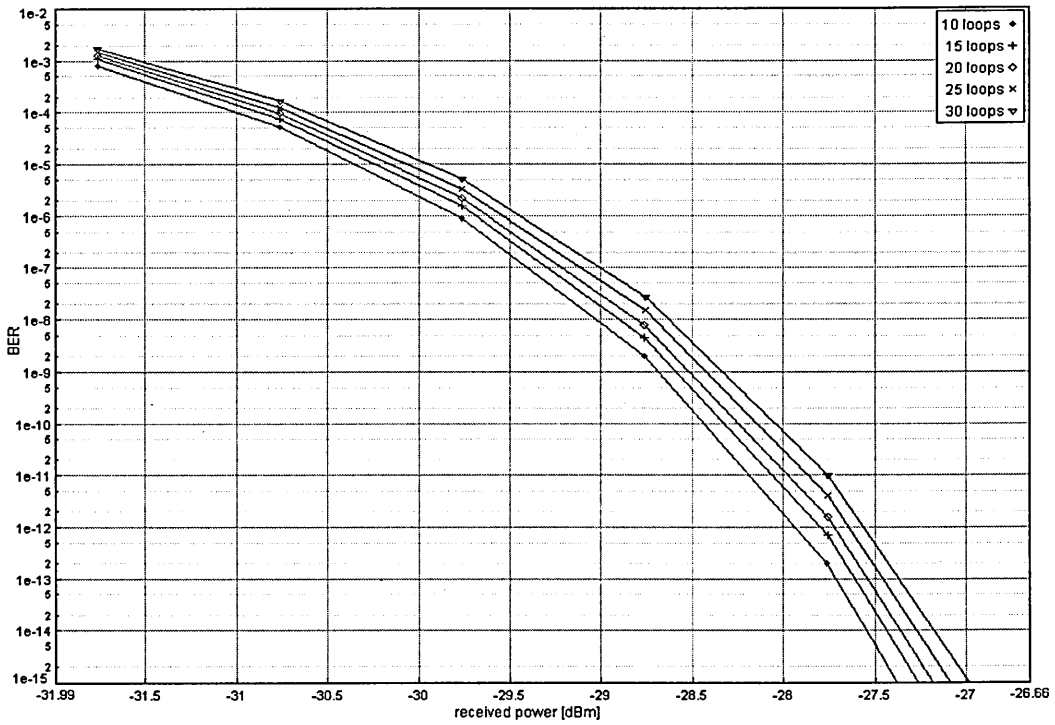

Figure 6.8 BER against the received power for various loop traversals of the active RFLB using normal fibre

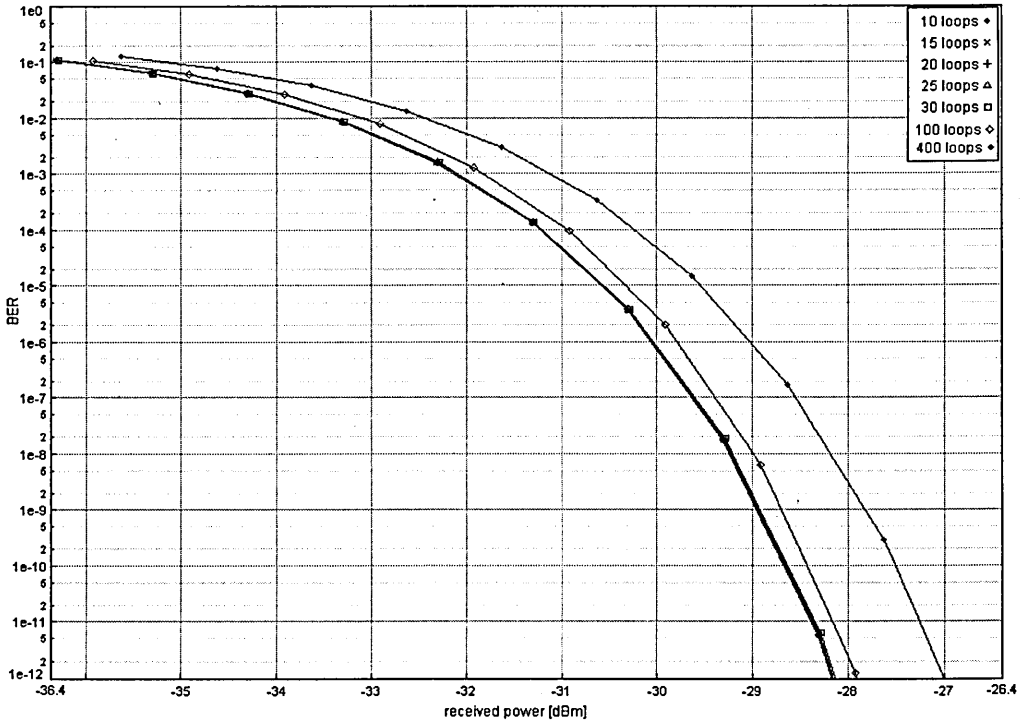

Figure 6.9 BER against the received power for various loop traversals of the active RFLB using DSF fibre

6.5 Mathematical Model of Active RFLB

Figure 6.10 shows the detailed system model employed by VPI highlighting the receiver structure and synchronisation (/timing) mechanisms. Thus, in defining the mathematical model of the active RFLB there is also an account for the noise sources associated with the receiver (see Table 6-3). Furthermore, in determining the BER performance characteristics the following assumptions are introduced. First, no additional timing jitter has been introduced at the transmitter. Second, the optical amplifier is characterised by a frequency- and wavelength-independent gain. Last, the low gain and the delay times under consideration are chosen so that amplifier saturation does not occur. Note that the optical amplifier preceding the active RFLB is employed to compensate for the initial switch insertion loss.

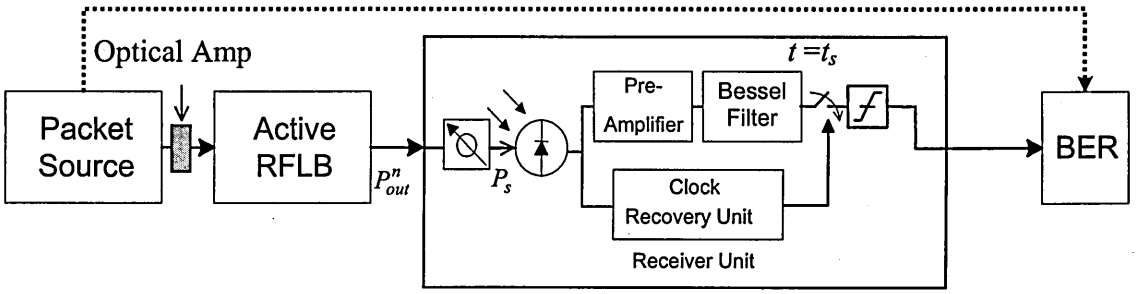

Figure 6.10 System model highlighting the receiver unit

Table 6-3 Active RFLB global simulation parameters

Parameter	Values
Switch insertion loss	1 dB
Switch crosstalk	30 dB
Data rate	20 Gbit/s
Optical Amplifier Gain (G)	~1.1 dB
Temperature (T)	293 K

Load resistance (R_L)	1820 kΩ
Electrical bandwidth (B_e)	0.7 * Data rate Hz
Optical bandwidth (B_o)	1.28 x 10^{12} Hz
Attenuation (κ)	30-40 dB

Let P_{in}^0 be the average peak power of the incoming soliton pulse train and P_{out}^i the average output power at the output of the active RFLB after the i^{th} loop circulation. After one loop circulation, the average output power can be written as:

$$P_{out}^1 = G\left(\left[P_{in}^0 \exp(-\alpha L)\right]\alpha_s\right) + P_{sp}, \tag{6.4}$$

where α is the intrinsic fibre loss, α_s the switch insertion loss including the crosstalk leakage, and L the unit buffer length. Additionally, G and P_{sp} are the gain and total spontaneous signal power of the optical amplifier, respectively. By recursively substituting the average output power (6.4) from the prior circulation for the average incident peak power at the subsequent buffer circulation, it can be shown that after l_n circulations the output power is given by:

$$P_{out}^{l_n} = \left[G \exp(-\alpha L)\,\alpha_s\right]^{l_n} P_{in}^0 + P_{sp} \sum_{i=0}^{l_n-1} \left[G \exp(-\alpha L)\,\alpha_s\right]^i, \tag{6.5}$$

Equation 6.5 highlights the independence between the signal and noise contributions. As depicted in Figure 6.10, the average power of the κ-dB attenuated data signal at the detector input is given by $P_s = P_{out}^{l_n} 10^{\frac{-\kappa}{10}}$. The variance equations for the receiver noise [11], [135], [139] and spontaneous beat noise terms associated with the preamplifier [11], [139], [140] are, respectively,

$$\sigma_{rec}^2 = \left[2qR\left(G_{pre}P_s + P_{sp}\right) + \frac{4K_BT}{R_L} \right] B_e, \tag{6.6}$$

$$\sigma_{pre}^2 = \left(4R^2 G_{pre} P_s S_{sp} + 4R^2 S_{sp}^2 B_o + 4qRS_{sp}B_o\right) B_e, \tag{6.7}$$

where B_e is the noise equivalent electrical bandwidth of the receiver, G_{pre} the unity preamplifier gain, B_o the optical bandwidth of the receiver, q the electron charge, K_B the Boltzmann constant, R the photodiode responsitivity, and R_L the load resistance of the photodetector. The noise spectral density of the optical amplifier $S_{sp} = n_{sp}(G-1)hB_0$, where h is Planck's constant. It can be shown that the inversion population factor n_{sp} of the optical amplifier is related to the noise figure F_n according to the expression $n_{sp} = 0.5\left(F_n G - 1\right)/\left(G-1\right)$ [141]. In (6.6) the first and second terms represent the shot and thermal noise variances, respectively. In (6.7) the three terms represent the signal-spontaneous, spontaneous-spontaneous and shot-spontaneous beat noise contributions, respectively.

Equation 6.8 accounts for the intensity fluctuations that arise from ASE noise to amplitude coupling [10].

$$\sigma_\eta^2 = S_n \xi, \tag{6.8}$$

where S_n is the ASE spectral density, η and ξ are the amplitude and propagation distance in soliton units, respectively. Furthermore, note that $\xi = z/L_D$ and $S_n = n_{sp}hf(G-1)\gamma L_D^2/L_A T_0$. Substituting S_n and ξ into (6.8) and using the

transformation $\sigma_\eta = \left(\sigma_P / \overline{P_{in}}\right)^{1/2}$ the variance in the power fluctuations in physical is given by:

$$\sigma_P^2 = \left(n_{sp} hf(G-1)\frac{\gamma L_D}{T_0} \cdot R \cdot \overline{P_{in}} \cdot l_n \right)^2, \tag{6.9}$$

where $\overline{P_{in}}$, z and γ, represent the average power of the incident soliton pulse train, the distance in real units and nonlinear coefficient, respectively. Moreover, the loop number $l_n = z/L_A$ and $L_D = T_0^2/\beta_2$ where β_2 is the group velocity dispersion parameter.

Adopting the same approach as in [142], [96]and [97], the BER can be given as:

$$BER = \frac{1}{2} erfc\left[\frac{RP_s}{(\sigma_1 + \sigma_0)\sqrt{2}} \right], \tag{6.10}$$

Note that σ_0 and σ_1 in (6.10) are readily obtained form (6.6), (6.7) and (6.9) by substituting $P_s = 0$ for σ_0 and $P_s = P_{out}^{l_n} 10^{\frac{-\kappa}{10}}$ for σ_1. Furthermore, the attenuator also reduces σ^2_p by κ-dB.

The proposed system was simulated using VPI and the results obtained for the BER performance were compared with predicted data. At each of the simulated loop circulation instances, the BER performance is averaged over 100 buffered packets to increase the statistical validity of the results.

As shown in Figure 6.11 there is a good agreement between the simulated (dotted curves) and theoretical (solid curves) models. For 100 loop circulations the power penalty incurred at a BER of 10^{-9} is ~0.2 dB. Extrapolation of the results to 400 circulations (T_{Loop} = 1 ms), well exceeds the forecasted storage time requirement [143] and results in a power penalty of ~0.77 dB.

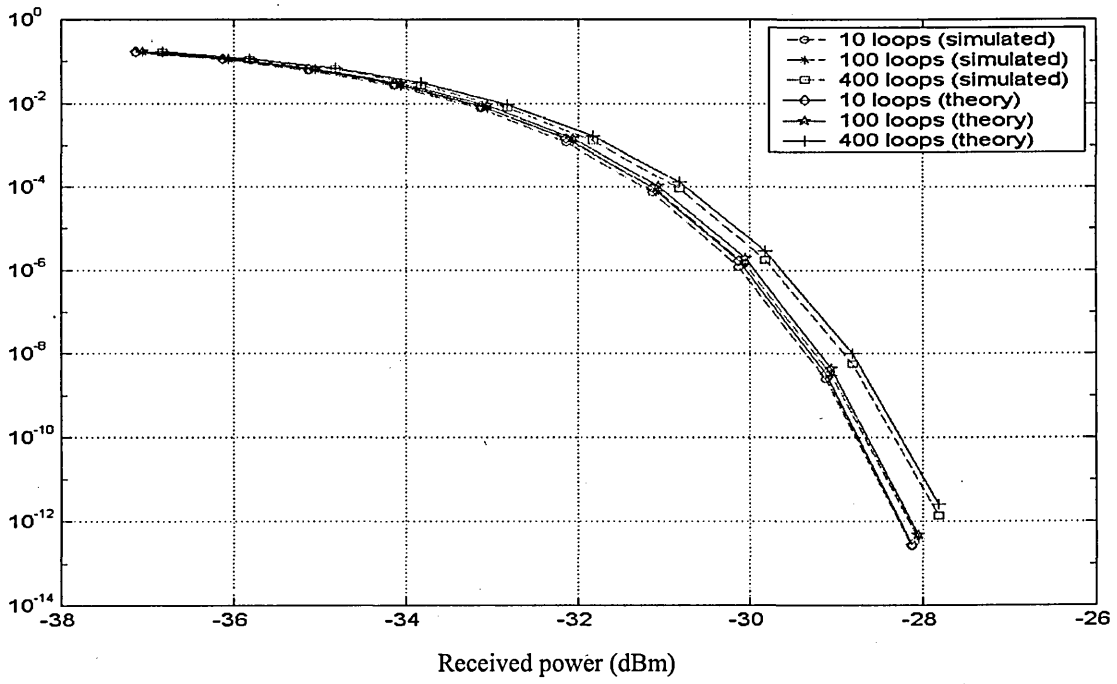

Figure. 6.11 Theoretical and simulated results of BER against the receiver sensitivity

On comparing Figures 6.9 and 6.11 it is evident that without the pre-buffer amplifier there is a 0.41 dB difference between the theoretical and simulated results. This is due to the assumption that the average peak power of the pulses within the packet remains constant as it traverses the loop. However, this approximation is only valid if the effect induced by the switch is negligible and if soliton interactions are marginal. The influence of the switch and ASE noise on the BER performance is highlighted in the following section.

6.6 Effect of ASE and Switch Losses on BER Performance

Lets consider the case where there is no pre-buffer amplifier to compensate for the switching loss. In this scenario, fundamental solitons are transmitted by the packet source. Under these conditions the dispersion length L_D and the non-linear length $L_{NL} = 1/\gamma P_0$ are equal and $\overline{N} = \sqrt{L_D / L_{NL}} = 1$ ensures that the delicate balance between GVD and SPM over the distance $L_D = L_{NL}$. On passing through the switch, the insertion loss (~ 1 dB) reduces the optical peak power required to maintain exact $\overline{N} = 1$ propagation, which ensures that the pulse envelope is constant over the dispersion (or non-linear) distance. However, $\overline{N}$ remains in the acceptable range for first order soliton propagation (i.e. $0.5 \leq \overline{N} \leq 1.5$). The decrease in power results in a reduced $\overline{N}$ parameter and an increase in the non-linear distance making it greater than the dispersion distance. Consequently, the effect of SPM now has a longer influence on the propagating pulses as the non-linear limit is increased. The propagation of the pulse now becomes similar in many aspects to the Gaussian-soliton pulses considered in the previous chapter where the pulses try to regain a pure $\overline{N} = 1$ profile.

The inverse relationship between the peak power and pulse width results in the pulses initially expanding to compensate for the power loss. This behaviour repeats itself on subsequent amplification instances until the lower peak power boundary required for soliton propagation is reached. At this stage the pulses contract and their average peak power increases until an upper boundary is reached. Evidence of this cycle is borne out in Figures 6.12 through 6.15, which show the evolution of the average peak power of the pulses within the packet with increasing loop traversal number. For each of the cases

presented DSF was used and three main scenarios have been considered: i) an ideal switch with no ASE noise being generated by the SOA (i.e. loss-less legend), ii) a non-ideal switch without ASE noise (i.e. no noise legend) and iii) a non-ideal switch with ASE noise (i.e. noise legend). Results are presented for different pulse widths and data rates B and the effect of pattern dependence on the cycle period is examined by considering scenarios where both an all '1' (All ones) and a pseudorandom (PRBS) bit pattern sequence is employed. Note that the all '1' sequence is not typical for an actual communication scenario and is only used here to allow for easy comparison of the test cases.

Figure 6.12 shows the average peak power versus loop number for B = 40 Gbit/s and T_{FWHM} = 8.82 ps, where an all '1' sequence is considered. As expected there is little variation in the average peak power when the system is loss-less. The slight variations are primarily due to the optical amplifier not exactly compensating for the inherent fibre loss. Evidence of the oscillations described above is observed in the scenario where the switch loss is included and ASE noise is excluded. Here the average peak oscillates with a period of approximately 450 loops. The periodicity remains unchanged with the inclusion of ASE noise, but results in a divergence of the average peak powers with increasing loop number. The difference which is negligible at l_n = 10, becomes 1.14, 1.52 and 2.67 mW where l_n = 210, 150 and 670, respectively.

A similar trend is observed in Figure 6.13 which shows the average peak power versus the loop number for B = 40 Gbit/s and T_{FWHM} = 4.41 ps. Again, an all '1' sequence is considered for the cases where the system is assumed to be both ideal (i.e. loss-less) and non-ideal (i.e. with and with out noise).

Note that as there is little variation in the average peak power in the loss-less scenario the trend is only presented for up to $l_n = 410$. Moreover, as the peak power divergence trend between the cases with and without ASE noise is repeated, only values of l_n over the same range for the case with noise are considered. This divergent trend is not present for $l_n \leq 50$ loops, and is negligible for $50\ l_n \leq 330$. Beyond this value of l_n the divergence becomes more apparent and is ~1 mW at $l_n = 410$ loops. In comparison with Figure 6.12, the smaller pulse width results in the decreased periodicity of the oscillations (~300 loops). This is expected, as the soliton period is directly proportional to the square of the normalised FWHM pulse width (see equation 4.43).

Figure 6.14 shows the average peak power verses the loop number for $B = 10$ Gbit/s, with the pulse width remaining at 4.41 ps. The loss-less case is as expected with the average peak power remaining relatively constant over the range of loop numbers considered. The scenario where both all '1' and pseudorandom sequences are considered is investigated for the first time. Note that ASE noise is present in both cases. The results show that the periodicity is not bit pattern dependent when the pulses are widely spaced.

Finally, Figure 6.15 shows the average peak power versus the loop number for $B = 20$ Gbit/s and $T_{FWHM} = 8.82$ ps. On comparison with Figure 6.12, note that average peak powers for the all-ones loss-less cases are similar, and that the all-one (noise) and all one (no noise) scenarios follow the similar previous divergence trends. The periodicity could not be determined for the Figure 6.15, as the average power does not return to its initial value over the range of l_n considered. However, the undulating variation of the average power is still observed. Moreover, nature of the undulating pattern is observed

to be also bit-pattern dependent. This may result in situations where the BER of a given packet may be better at longer storage times. For example, lets consider the case where the PRBS packet is examined at $l_n = 250$ and 400, respectively. Figure 6.15 confirms the average peak power at 400 loops is greater than that at 250. Furthermore the noise contributions are similar in both instances. The plot of BER versus the received power, shown in Figure 6.16, confirms that $l_n = 400$ provides better performance with a gain of 0.34 dB over $l_n = 250$ at BER = $1x10^{-9}$.

To avoid this type of scenario, a pre-buffer amplifier is employed to compensate for the initial switch loss. This scenario is highlighted in Figure 6.15 (*PRBS Pre-buffer (noise)). Here the increase in average peak power is attributed to the accumulation of ASE noise. For comparison, the case where no pre-buffer amplifier is employed and ASE noise accounted for within the in-loop amplifier is also considered for a PRBS sequence (*PRBS No Pre-buffer (noise)). Comparison with the all ones (noise) case then provides further evidence that the variation of average peak power with l_n is bit pattern dependent.

In the next section the introduction of in-loop filtering to reduce the ASE noise contribution and improve the buffer performance is presented.

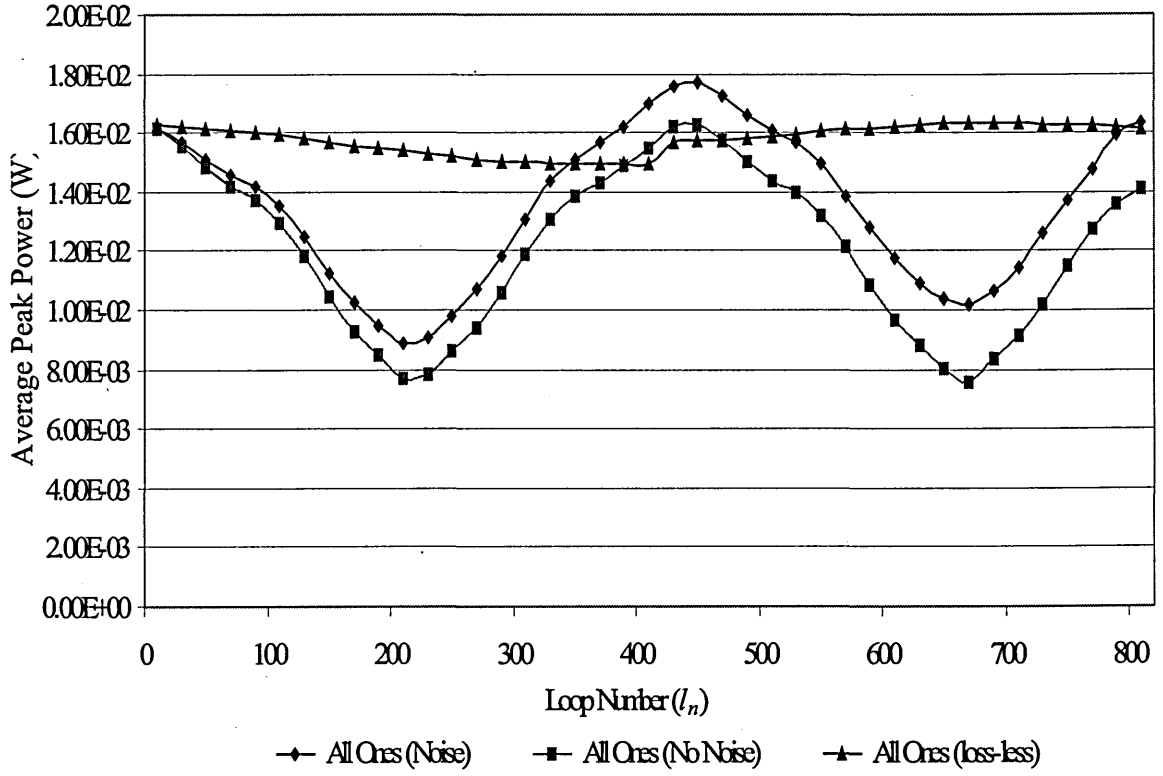

Figure 6.12 Average peak power against the loop number (B = 40 Gbit/s, T_{FWHM} = 8.82 ps)

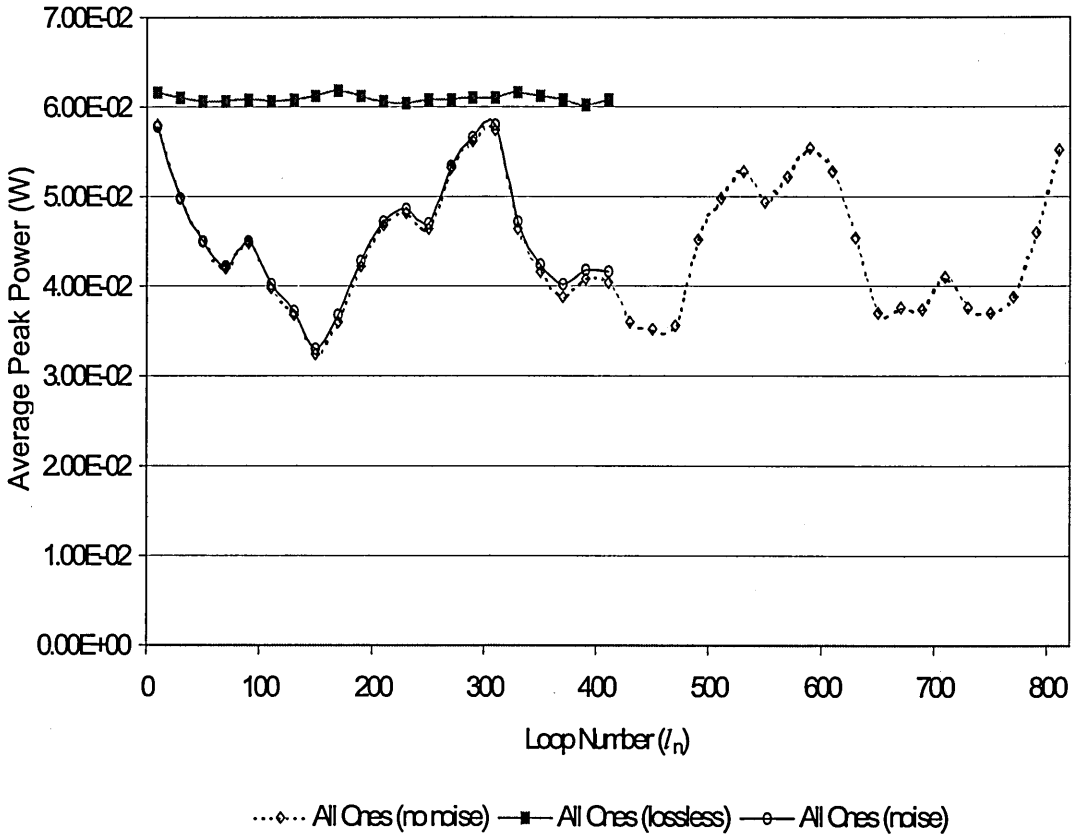

Figure 6.13 Average peak power against the loop number (B = 40 Gbit/s, T_{FWHM} = 4.41 ps)

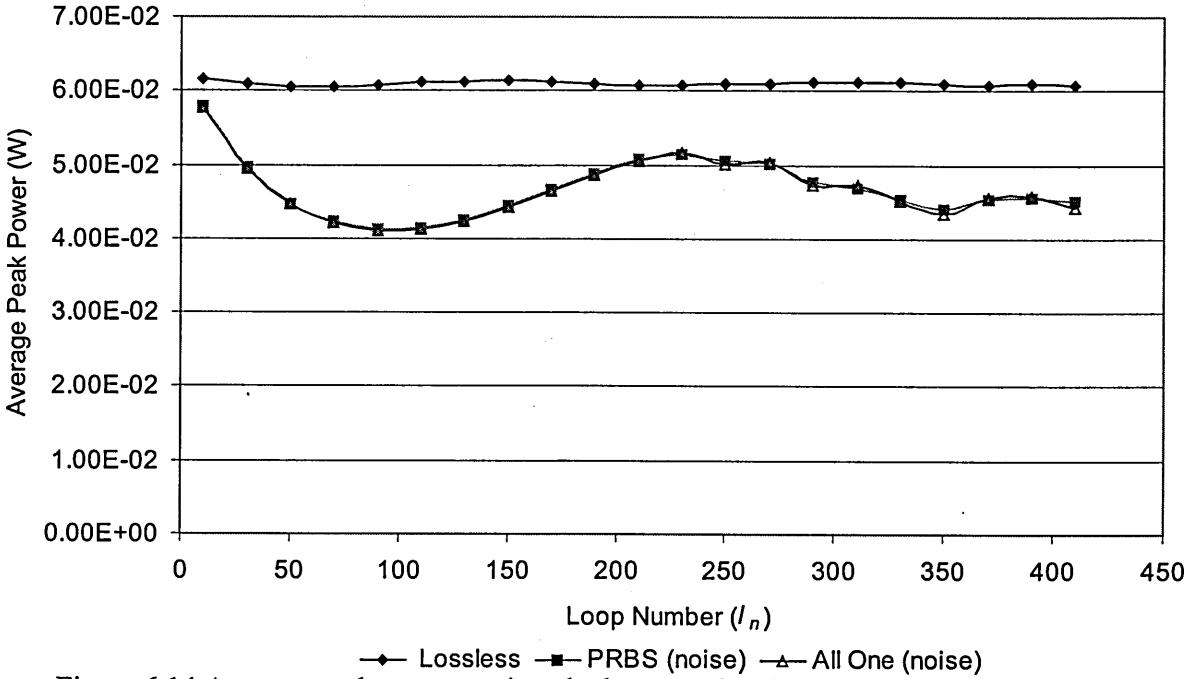

Figure 6.14 Average peak power against the loop number (B = 10 Gbit/s, T_{FWHM} = 4.41 ps)

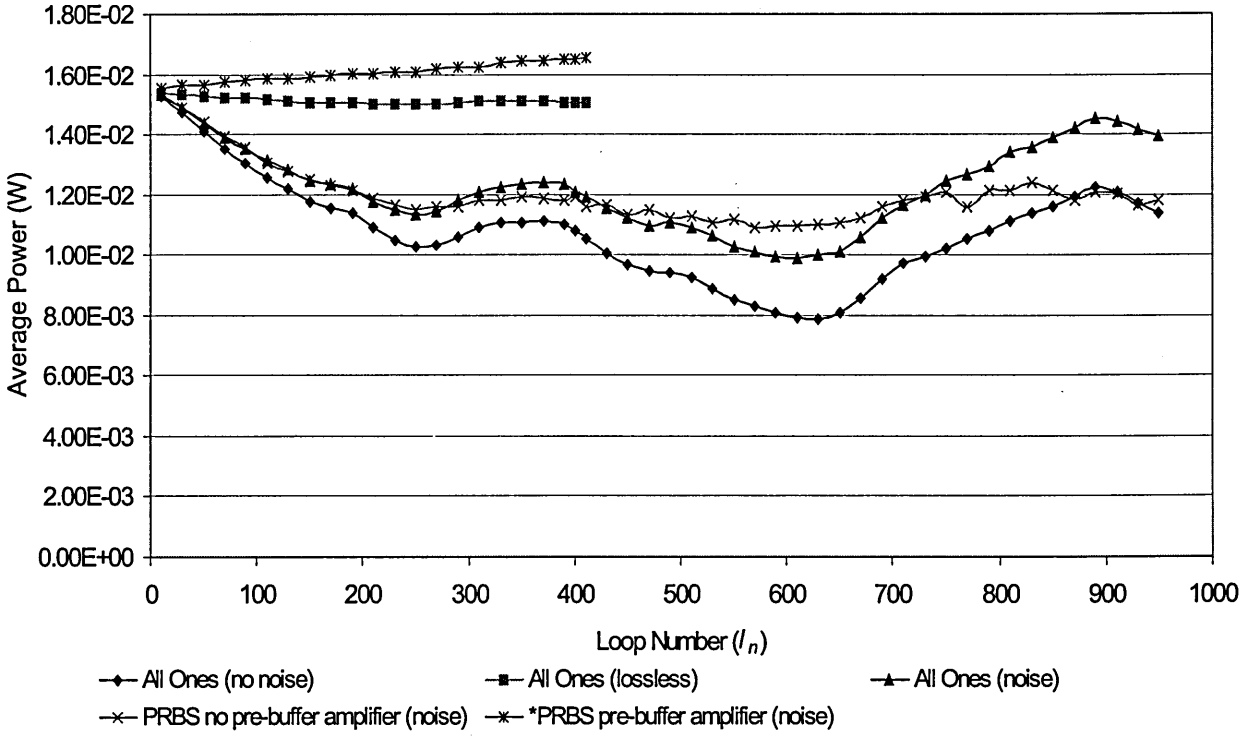

Figure 6.15 Average peak power against the loop number (B = 20 Gbit/s, T_{FWHM} = 8.82 ps)

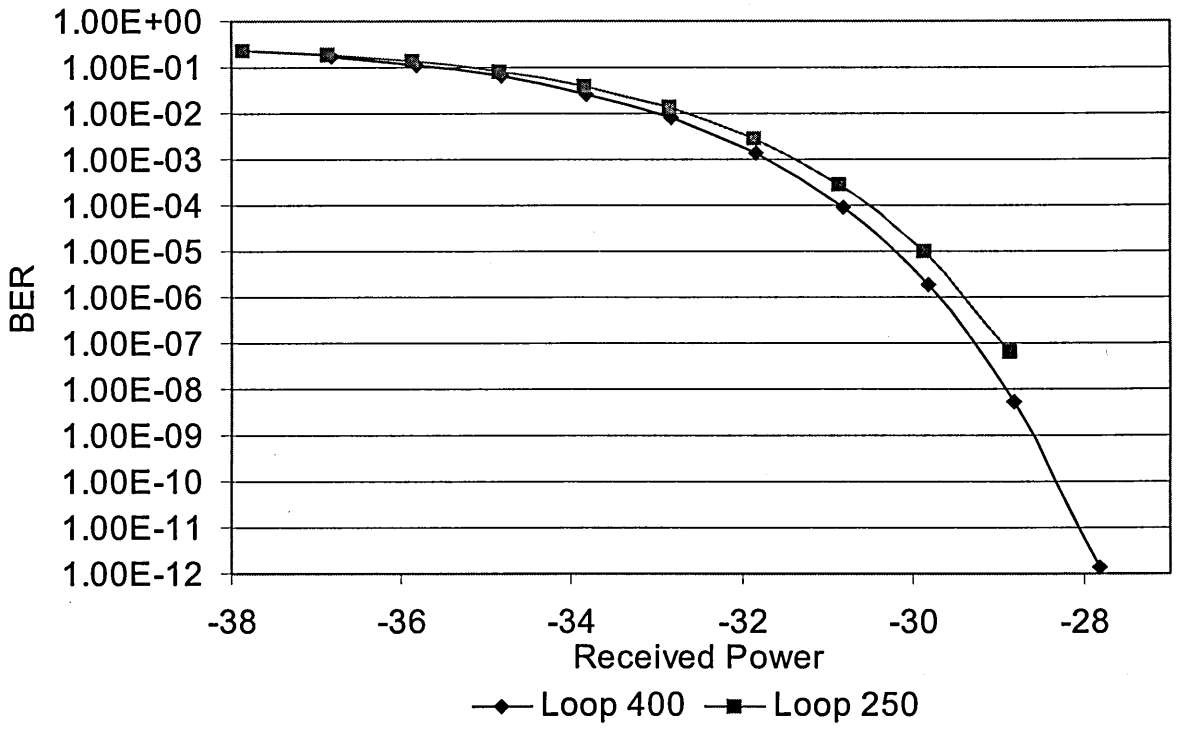

Figure 6.16 BER against the received power for loop numbers 250 and 400

6.7 Soliton Control by In-loop Filtering

In the Section 6.5, the BER performance of the buffer with respect to the loop number was observed to be optimised once the fundamental soliton property (i.e. peak power remained constant) was maintained over loop successive traversals. Moreover, the linear growth of the intensity variations due to the accumulation of ASE was highlighted. In this section in-loop filtering, common within loop experiments to reduce the amplifier noise contributions [144-147] will be investigated, as a technique for further improvement of the BER performance.

The simulation model is as given in Figure 6.10 with the exception that an optical third-order band-pass filter has been placed after the optical amplifier the loop.
The transfer function of the filter is given as [148]:

$$H(p) = \frac{15}{15p^3 \cdot (f - f_c)^3 + 6p^3 \cdot (f - f_c)^2 + 15p \cdot (f - f_c) + 15} \cdot \exp(i2\pi f_c t), \tag{6.11}$$

where $p = i \cdot 2/f_{3\mathrm{dB}}$, where f_c and f_{3dB} are the optical carrier frequency and the cut off frequency of the filter, respectively. The simulation parameters are as listed in Table 6-2. Additionally, the filter cut-off frequency is set to ~$20\text{x}10^{11}$ Hz, which is five times greater than the first harmonic frequency, as the solitons are transformed limited. A bandwidth that is too narrow should be avoided as this causes significant reduction in the power of the soliton pulses thus requiring excess optical gain. Furthermore, in

severe cases, this results in the same type of peak power fluctuations induced by the switch insertion loss.

Figure 6.17 shows simulation results for the BER against the receiver power for a buffered system with and without the optical filter. Loop numbers 10 and 100 show no marked improvement in performance when the filter is introduced. However, there is an ~0.21dB improvement in the power penalty at BER of 10^{-9} when the loop number is increased to 400.

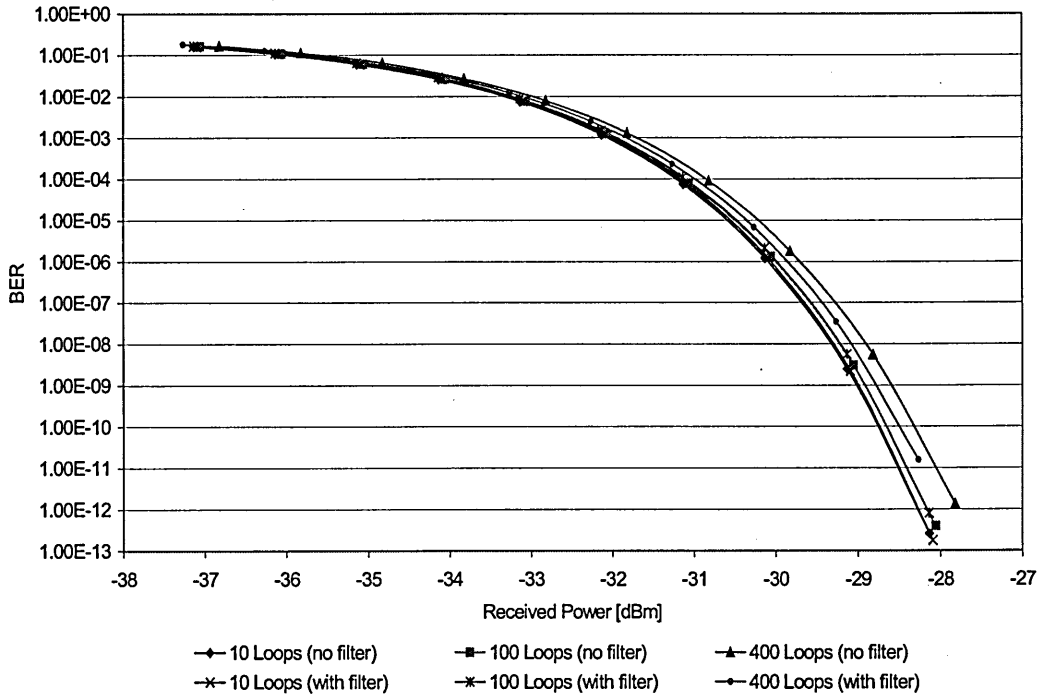

Figure 6.17 BER against receiver power for system employing filter

6.8 Summary

In this chapter, the performance of the active RFLB was examined both theoretically and through simulations. The effect of different fibre types with different first order dispersion parameters was investigated and it was found that DSF fibre performed better

than normal fibre. In addition, both the effect of the soliton amplification regime on BER performance of the buffer and the influence of the Gordon-Haus timing jitter were examined. The maximum soliton amplification period was found to be 6-loop traversals, and the Gordon-Haus jitter was determined to be negligible over the delay times considered. The theoretical results highlight the noise accumulation effect, which is responsible for the degradation of BER performance on each loop circulation. This accumulation, along with its associated spontaneous beating noise dynamics, and the thermal and shot noises at the receiver is the main performance degrading factors. In-loop filtering was shown to reduce the accumulation of ASE noise providing a gain of 0.21 dB over the unfiltered case at BER of 10^{-9} for $l_n = 400$.

In the next chapter, the generic switch employed within the RFLBs thus far is replaced with a more practical switching architecture. Moreover, the performance of the amended buffer model is investigated.

Chapter 7

Active RFLB Employing SMZ Switch

7.1 Introduction

In the previous chapter, the performance characteristics of an active all-optical buffer under varying conditions were examined when the switch and amplification elements were taken to be generic. Since the performance inherently depends on the characteristics of these core components, a more practical device model is developed where the SMZ is employed to provide a gain-switching action. First, the theoretical concepts and mathematical model of the SOA are presented in section 7.2. In the next section, the mathematical model is then employed to optimise the SOA parameters used in the SMZ switch. In section 7.4, novel operational modes for the SMZ switch used within the buffering architecture are presented, and the associated theory describing these modes is presented in section 7.5. The buffer performance is monitored using eye diagrams to investigate the effect of these operational modes in section 7.6. Finally, this chapter concludes with a summary in section 7.7.

7.2 Semiconductor Amplifier Concepts and Numerical Model

As illustrated in Figure 7.1, amplification within semiconductors is two-stage process. First, the atoms within the valence band absorb the photonic energy contained within the incident light. Subsequently, these energised atoms are temporarily promoted to the conduction band in the process is known as stimulated absorption. In the second or emission stage, the excited atoms return to the ground state releasing the stored photonic energy as light. These emissions may either be stimulated or spontaneous, with the difference being that the former is initiated by another incident photon, whilst the latter occurs randomly. Both types of emissions are realised in practical devices; however, in an ideal amplification scenario it is desirable for the stimulated emissions to be the dominant. This is due to the stimulated emission photons having the same energy (E_p = hf) and propagation direction as that of the incident light, thereby effecting amplification. In contrast, spontaneously emitted photons have a random propagation direction and lack any phase relationship. Consequently, they are responsible for the noise produced by the amplifier.

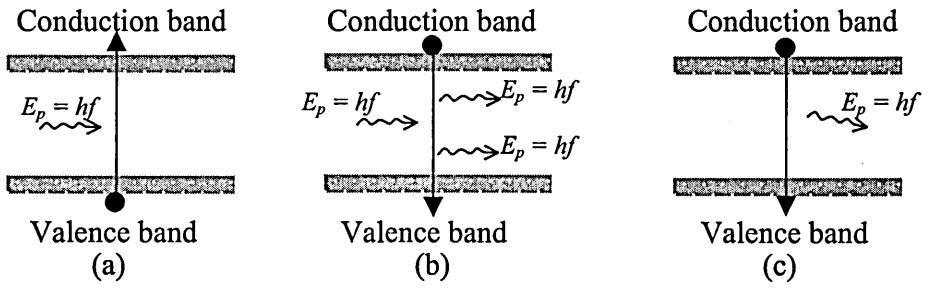

Figure 7.1 Amplification process; (a) stimulated absorption, (b) stimulated emission, and (c) spontaneous emission

This amplification process is further illustrated in Figure 7.2 where the length of the amplifier has been divided into segments. Moreover, population inversion, where the

number of carriers in the conduction band is greater than the number of carriers in the valence band is assumed. This is achieved by applying a bias current I_B to the device. Observe that the incident pulse is effectively amplified within each segment and stimulated emission is dominant.

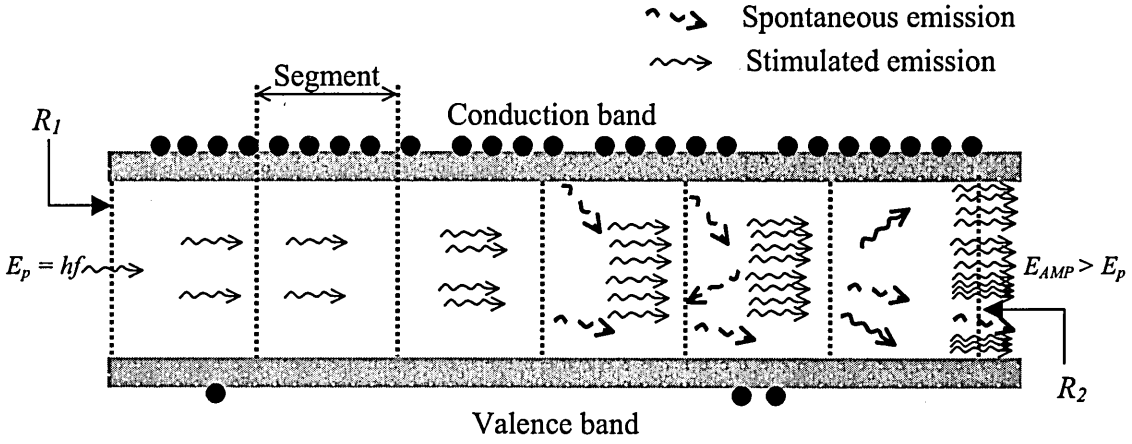

Figure 7.2 Amplification process within a TWA

Here the schematic is based on the travelling wave amplifier (TWA) where the facet reflectivities R_1 and R_2 are such that $G\sqrt{R_1 R_2} < 0.17$ [149]. For an ideal TWA, $R_1 = R_2 \cong 0$ and the incident signal only travels in the forward direction through the active medium. Conversely, for $R_1 > 0, R_2 > 0$, the incident signal resonates within the amplifier cavity. On each oscillation the gain of the signal is increased until a steady state is reached where the stimulated emission is equal to the rate of photon loss. Due to the inherent multi-pass gain, these so-called Fabry-Perot (FP) semiconductor laser amplifiers (FP-SLAs) require less bias current than their TWA counterparts to provide the same high output gain. Additionally, they require a lower carrier density to attain a high internal gain and introduce less ASE noise due to its narrower bandwidth [97]. However, the TWAs exhibit many desirable characteristics thus making them more appropriate for the switching functions required. Namely, they have a low sensitivity to

signal polarisation, high tolerance to bias current and temperature fluctuations. Moreover, their wider bandwidth capability permits amplification of narrower pulses with reduced distortion [97].

The numerical model for such a device is based on a system of rate equations that relate the amplifier gain to the carrier density. Moreover, the physical quantities, such as light power, are averaged over the amplifier's length L_{AMP}. The gain per unit length or material gain coefficient $g(N)$ is defined as [149-154]:

$$g(N) = \frac{dg}{dN}(N - N_{tr}), \tag{7.1}$$

where N and N_{tr} represent the carrier density and the carrier density at transparency, respectively. dg/dN is referred to as the differential modal gain and characterises the slope dependence of $g(N)$. More specifically the net gain $g_{tot}(N)$ coefficient is defined by [141], [155]:

$$g_{tot}(N) = \Gamma \cdot g(N) - \alpha_{AMP}, \tag{7.2}$$

where α_{AMP} is the internal waveguide scattering loss, and Γ is the confinement factor, which is defined as the ratio between the cross-sectional area of the active medium and the transverse area of the optical waveguide. In essence, Γ accounts for the fact that

only a portion of the optical distribution travels within the active medium and therefore experiences a gain.

Using (7.2), and assuming a constant carrier density at any given location z within the amplifier, the total gain experienced by an the optical wave at z is then given by:

$$G(N,z) = e^{g_{tot}(N)\cdot z}. \tag{7.3}$$

Consequently, the average output power P_{avg} over the length of the amplifier becomes,

$$P_{avg} = \frac{1}{L_{AMP}} \int_0^{L_{AMP}} P_{in} G(N,z)\, dz. \tag{7.4}$$

Note that P_{avg} is a function of time as the input signal power $P_{in}(t)$ and the carrier density $N(t)$ are both time-dependent. Moreover, the rate equation which defines the $N(t)$ is given by [141]:

$$\frac{dN}{dt} = \frac{I_B}{qV} - \frac{N}{\tau_c} - \frac{\Gamma \cdot g(N) \cdot P_{avg}(N,t) \cdot L_{AMP}}{V \cdot h \cdot f}. \tag{7.5}$$

where q, τ_c and V represent the electron charge, recombination time and volume of the active medium, respectively.

The first term on the right hand side of (7.5) represents the stimulated absorption process, where the biased current is applied to promote carriers from the valence to the

conduction band. Conversely, the final term denotes the decrease in the carrier density due to the stimulated emission and consequently represents the amplification process. Finally, the second term denotes the decrease in the carrier density due to the spontaneous emissions. To account for both radiative and nonradiative recombination this term is rewritten as: [141], [151-152], [155]

$$R(N) = \frac{N}{\tau_c} = AN + BN^2 + CN^3 \tag{7.6}$$

with A, B and C representing the surface and defect recombination, the radiative recombination and the Auger recombination coefficients, respectively. Both definitions of the spontaneous recombination rate are popular within the literature, however the latter will be employed in this work. This sacrifices a small amount of computational power for increased flexibility and is consistent with the VPI model.

7.3 Semiconductor Amplifying Characteristics

The physical amplifier properties listed in Table 7.1 were employed in conjunction with equations 7.1–7.6 to investigate the amplifier gain characteristics under various operating conditions. Namely the effect of optical carrier frequency, biased current and amplifier dimensions on the gain of the device are examined. These results will be used as a precursor in determining the optimal parameters for amplifier employed within the SMZ architecture.

Table 7.1 Global SOA parameters

Parameter description	Value (units)
SOA width	8×10^{-6} (m)
SOA depth	0.4×10^{-6} (m)
Confinement factor	0.15
Differential gain	2.78×10^{-20} (m^2)
Transparent carrier density	1.4×10^{24} (m^{-3})
Linewidth enhancement factor	5.0
Internal losses	40×10^{-2} (m^{-1})
Recombination constant A	1.43×10^{8} (s^{-1})
Recombination constant B	1.0×10^{-16} (m^3s^{-2})
Recombination constant C	3.0×10^{-41} (m^3s^{-6})

Figure 7.3 shows the plot of amplifier gain against the average incident power for three optical carrier frequencies. Note that in this case the SOA length is 1 mm and the bias currents are 100 and 150 mA.

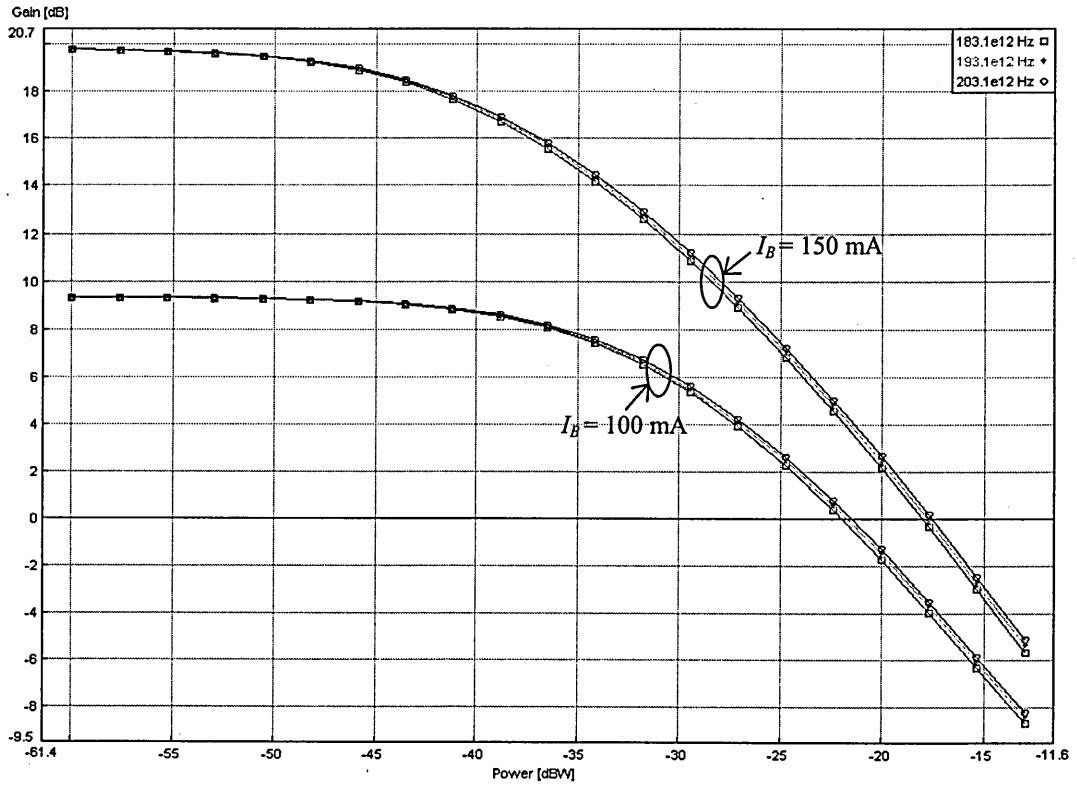

Figure 7.3 Amplifier gain against the incident power for different carrier frequency

The results show that there is little difference in the gain characteristics over the range of frequencies considered. However 193.1×10^{12} Hz is chosen for future results as this corresponds to the 1500 nm window range where the intrinsic fibre loss is lowest.

Figure 7.4 shows the amplifier gain against the average incident optical power for different bias currents and amplifier lengths. The numerical legend below the figure indicates the SOA length for the given simulation scenario. The results show that for a given fixed SOA length, increasing the bias current generally results in a greater initial gain. Moreover, for a fixed bias current, an increase in the device length affects both the gain saturation and roll-off dynamics.

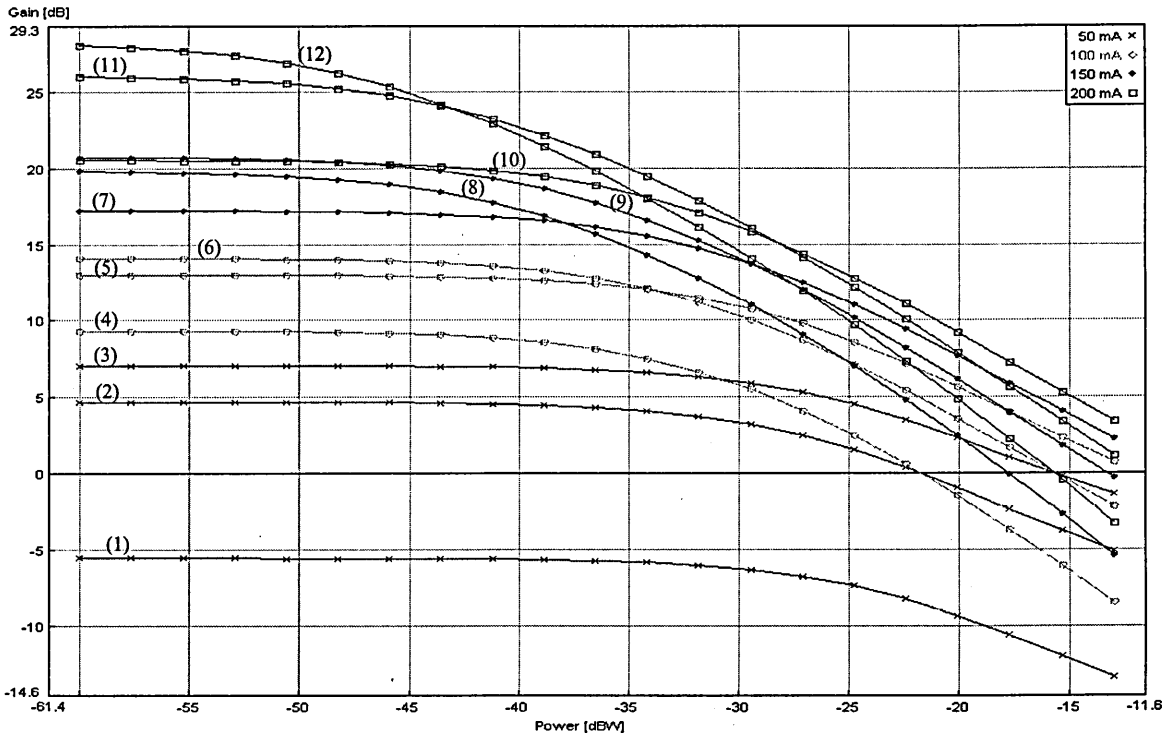

Figure 7.4 Amplifier gain against the incident power for physical SOA characteristics

(1) 1 mm	(2) 500 μm	(3) 250 μm	(4) 1 mm	(5) 250 μm	(6) 500 μm
(7) 1 mm	(8) 250 μm	(9) 500 μm	(10) 1 mm	(11) 250 μm	(12) 500 μm

The challenge to the buffer designer in using this device in the switching architecture is to employ the appropriate dynamics such that firstly, there is a large gain for the pulses that are to be switched. Secondly, the roll-off is relatively steep. Thirdly, the incident power, and by extension the average input energy, required to drive the device into an absorption mode is feasible and finally, that the device parameters are indeed not impractical. The curve labelled '9' showed the most promise with regard to meeting these criteria.

7.4 Model of RFLB Employing SMZ Switch

Previous investigations carried out in this work on soliton propagation, all optical switches and RFLBs have produced results that the buffer designer may use to optimise the BER performance for a given delay storage time. In this section, the design considerations are amalgamated and the best specifications to produce what is considered to be the optimal buffer architecture are chose.

This revised architecture presented in Figure 7.5, employs a dispersion shifted fibre loop and accounts for the new switching mechanism. Note that in this case, packets entering via the path connecting ports A and B circulate around the loop for a delay time, $T_{loop} = nL/c$, before exiting via path 'AC'. Accordingly, unbuffered packets travel along the path connecting ports A and C.

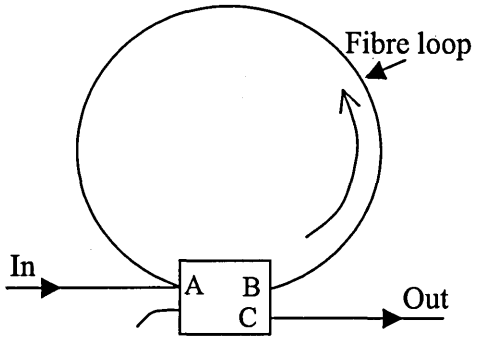

Figure 7.5 Revised block diagram of RFLB

Figure 7.6 shows the detailed configuration of the SMZ switch as it relates to the buffering architecture. A length of fibre L connects output port B of the switch back to the input port A. An inherent advantage of this switching architecture is that the switching speed and the symmetric property of the switch window profile is not dependent on the carrier dynamics of the semiconductor amplifier (SOA) [67], [156-157]. Additionally this device has the capability to vary the amount of data bits (packet length) that can be switched (i.e. switching window Δt), without physical changes to the device, by simply controlling the relative delay between the control pulses in the two arms of the device.

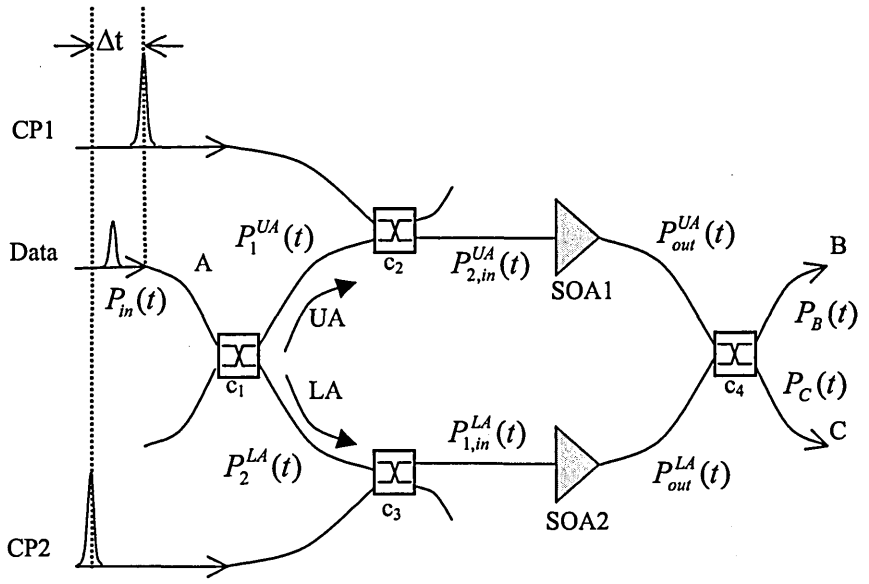

Figure 7.6 Symmetric Mach-Zehnder (SMZ) switch

Switching packets of different sizes in other non-linear switching devices such as the terahertz optical asymmetric multiplexer (TOAD), where the size of switching window depends on the spatial location of the non-linear device would present quite a challenge. As illustrated in Figure 7.6, packets entering the SMZ at port 'A' travel along the upper (UA) and lower arms (LA) after being split by the 50/50 coupler c_1. The first control pulse *CP*1 arrives at the semiconductor optical amplifier (SOA1) ahead of the packet thereby inducing saturation. This results in a relative phase change in the pulse(s) that immediately follow *CP*1. Concurrently, the data packet travelling along LA emerges from SOA2 with a different amplitude profile. On recombining at the coupler c4 the induced relative phase and amplitude changes cause the data to be transmitted to port B. In the absence of control pulses, the packet exits via port C, thus this condition is used to clear the loop and for unbuffered pulse operation. The delayed control pulse *CP*2 effectively serves as a switch-off mechanism closing the switching window, avoiding

the reliance on the relatively slow recovery times of the SOAs. This operation enables the SMZ to demultiplex at data rates in the sub-picosecond range [158]. Not shown in Figure 7.6 are the orthogonally polarised control pulses, which are removed using polarisation splitters located before c_4 in each of the device's arms. Switching packets however introduces another complexity whereby much wider switching windows need to be produced. Multiple control pulses can be employed to extend the width of the switching window profile but maintaining the required relative π-phase shift becomes very challenging.

To overcome this problem, a novel approach has been adopted where the control pulses CP1 are used to reduce the gain of the data pulses (/packet) in the UA that are to be switched. Concurrently, the gain-enhanced pulses along LA emerge from SOA2. The delayed CP2 pulses trailing the packet along LA once again act to close the switching window. In essence on recombining at the 50/50 coupler the UA packet will have little contribution, where as the LA packet is transmitted at ports B and C (at half the intensity). Such an operation where the packet is unperturbed, as it propagated is particularly desirable in broadcast networks where a copy of the packet is required at each node. More importantly, there is no bottleneck introduced by O/E and E/O conversions. Note that in the buffering scenario, the output from port B is attenuated just before it is reinserted to the system via port A. This is necessary because of the gain switching nature of the SMZ switch.

7.5 Analysis for Buffering

The approach adopted here builds on the work done by Eiselt [68] and Agrawal [11]. Assuming ultra-short pulses such that $T_{FHMM} << \tau_c$, it can be shown that the device's gain characteristic is given by [11], [150], [159]:

$$G(t) = \frac{G_0}{G_0 - (G_0 - 1) \cdot \exp\left(\frac{E_{in}(t)}{E_{sat}}\right)}, \tag{7.7}$$

where G_0, $E_{in}(t)$ and E_{sat} denotes small signal gain, the time variant energy of the input pulse and the saturation energy of the amplifier, respectively.

Moreover, the momentary gain during the recovery stage is given by [68]:

$$G(t) = G_0 \cdot \left(\frac{G(t_{sat})}{G_0}\right)^{\exp[(t_{sat}-t)/\tau_c]}, \qquad \text{for } t \geq t_{sat}, \tag{7.8}$$

where t_{sat} denotes the time at which saturation occurred. Note that the derivations of (7.7) and (7.8) can be found in Appendix D.

To account for the Δt_{cp}-spaced control pulses, and the dual operation modes of the device, the generalised form of the above equations become:

$$G_{cp}(t)=\begin{cases}\dfrac{G_0}{G_0-(G_0-1)\cdot\exp\left(\dfrac{E_{in}(t)}{E_{sat}}\right)} & \text{for } (m-1)\cdot(t_m+\Delta t_{cp})\le t\le m\cdot(t_m+\Delta t_{cp})-\Delta t_{cp}\\ G_0\cdot\left(\dfrac{G(t_{sat})}{G_0}\right)^{\exp[(t_{sat}-t)/\tau_c]} & \text{for } m\cdot(t_m+\Delta t_{cp})-\Delta t_{cp}\le t\le m\cdot(t_m+\Delta t_{cp})\end{cases} \tag{7.9}$$

where the gain due to the control pulse saturation is denoted as $G_{cp}(t)$. Additionally, m, and t_m represent the control pulse number and its temporal duration, respectively. Note that in (7.9) $t_{sat}\approx m\cdot(t_m+\Delta t_{cp})-\Delta t_{cp}$ for narrow, high intensity control pulses. Moreover, for closely spaced pulses (Δt_{cp} ~= 0), the gain of the device does not recover. The phase change associated with the changing gain profile between the arbitrary times t_1 and t_2 is given by [68]:

$$\Delta\varphi(t)=\varphi(t_2)-\varphi(t_1)=-\frac{\psi_{lef}}{2}\cdot\ln\left(\frac{G(t_1)}{G(t_2)}\right). \tag{7.10}$$

where ψ_{lef} is the line enhancement factor of the device.

For the upper arm of the device, the output power is then defined as:

$$P_{out}^{UA}(t_n)=P_{2,in}^{UA}(t_n)\cdot G_{cp}^{UA}(t_n). \tag{7.11}$$

Conversely, the output power within the lower arm depends on the time-lag Δt between the control pulses in the upper- and lower arms and is defined as:

$$P_{out}^{LA}(t_n) = \begin{cases} P_{1,in}^{LA}(t_n) \cdot G_{cp}^{LA}(t_n) & t_n \le \Delta t \\ P_{1,in}^{LA}(t_n) \cdot G_{cp}^{LA}(t_n + \Delta t) & t_n > \Delta t \quad \text{(joint mode)} \\ P_{1,in}^{LA}(t_n) \cdot G_{cp}^{LA}(t_n + \Delta t) & (t_{pre} + t_{packet}) \le t_n \le t_{total} \quad \text{(independent mode)} \end{cases} \tag{7.12}$$

With t_{pre} and t_{total} representing the initial guard band time and the total switching time inducing the pre- and post guard band times, respectively.

Given that $P_{in}(t)$ represents the power profile on the incident pulses then the power coupled into UA and LA by C_1 are defined by the transmission matrix defined by:

$$\begin{pmatrix} P_1^{UA}(t) \\ P_2^{LA}(t) \end{pmatrix} = \begin{pmatrix} 1-\vartheta_{cf} & -\vartheta_{cf} \\ -\vartheta_{cf} & 1-\vartheta_{cf} \end{pmatrix} \cdot \begin{pmatrix} P_{in}(t) \\ 0 \end{pmatrix}. \tag{7.13}$$

Similarly, $P_{2,in}^{UA}(t)$ and $P_{1,in}^{LA}(t)$ may be inferred from (7.13) as shown below.

$$\begin{pmatrix} P_{1,in}^{UA}(t) \\ P_{2,UA}^{UA}(t) \end{pmatrix} = \begin{pmatrix} 1-\vartheta_{cf} & -\vartheta_{cf} \\ -\vartheta_{cf} & 1-\vartheta_{cf} \end{pmatrix} \cdot \begin{pmatrix} 0 \\ P_1^{UA}(t) \end{pmatrix} \tag{7.14}$$

$$\begin{pmatrix} P_{1,in}^{LA}(t) \\ P_{2,UA}^{LA}(t) \end{pmatrix} = \begin{pmatrix} 1-\vartheta_{cf} & -\vartheta_{cf} \\ -\vartheta_{cf} & 1-\vartheta_{cf} \end{pmatrix} \cdot \begin{pmatrix} P_2^{LA}(t) \\ 0 \end{pmatrix} \tag{7.15}$$

where the coupling factor, ϑ_{cf}, is bounded by $0 \leq \vartheta_{cf} \leq 1$.

The final output power at B and C of coupler c_4 depends on the relative gain and phase of the incident pulses within the upper and lower arms. Thus, using the coupling transmission matrix, $P_B(t)$ and $P_C(t)$ may be expressed as:

$$\begin{pmatrix} P_B(t) \\ P_C(t) \end{pmatrix} = \begin{pmatrix} 1-\vartheta_{cf} & -\vartheta_{cf} \\ -\vartheta_{cf} & 1-\vartheta_{cf} \end{pmatrix} \cdot \begin{pmatrix} P_{out}^{UA}(t) \\ P_{out}^{LA}(t) \end{pmatrix} \tag{7.16}$$

Equation (7.16) may then be expanded using (7.13) – (7.15) to yield:

$$P_B(t) = (1-\vartheta_{cf})^3 \cdot P_{in}(t) \cdot G_{cp}^{UA}(t) - \vartheta_{cf} \cdot (1-\vartheta_{cf})^2 \cdot P_{in}(t) \cdot G_{cp}^{LA}(t) \tag{7.17a}$$

$$P_C(t) = (1-\vartheta_{cf})^2 \cdot \vartheta_{cf} \cdot P_{in}(t) \cdot G_{cp}^{LA}(t) - \vartheta_{cf}^{\,2} \cdot (1-\vartheta_{cf}) \cdot P_{in}(t) \cdot G_{cp}^{UA}(t) \tag{7.17b}$$

Furthermore, to highlight role of the dynamic gain-induced phase shift of the amplified pulse profile, it is instructive to express the pulse power and power gain as the complex electric field intensity and electric field gain equivalents. Consequently, equations 7.17(a) and 7.17(b) become:

$$P_B(t) = P_{in}(t) \cdot \left[\begin{array}{l} (1-\vartheta_{cf})^3 \cdot G_{cp}^{UA}(t) + \vartheta_{cf}^{\,2} \cdot (1-\vartheta_{cf}) \cdot G_{cp}^{LA}(t) \\ -2 \cdot \sqrt{(1-\vartheta_{cf})^4 \cdot \vartheta_{cf}^{\,2} \cdot G_{cp}^{UA}(t) \cdot G_{cp}^{LA}(t)} \cdot \cos[\varphi_{UA}(t) - \varphi_{LA}(t)] \end{array} \right] \tag{7.18a}$$

$$P_C(t) = P_{in}(t) \cdot \left[\begin{array}{l} (1-\vartheta_{cf})^2 \cdot \vartheta_{cf} \cdot G_{cp}^{LA}(t) + \vartheta_{cf}^{\,2} \cdot (1-\vartheta_{cf}) \cdot G_{cp}^{UA}(t) \\ -2 \cdot \sqrt{(1-\vartheta_{cf})^3 \cdot \vartheta_{cf}^{\,3} \cdot G_{cp}^{UA}(t) \cdot G_{cp}^{LA}(t)} \cdot \cos[\varphi_{UA}(t) - \varphi_{LA}(t)] \end{array} \right] \quad (7.18b)$$

where $\cos(\Delta\varphi)$ is related to the gain ratio and line enhancement factor as shown in (7.10). The device is defined as balanced when $G_{cp}^{UA}(t) = G_{cp}^{LA}(t)$ as there are equal contributions at the switched output for the upper and lower arms of the device. In this work $\vartheta_{cf} = 0.5$, resulting in $\left|P_{2,in}^{UA}(t)\right| = \left|P_{1,in}^{LA}(t)\right|$ and a relative phase difference of $\pi/2$ rad. Consequently, the final derived equations that describes the switched output are:

$$P_B(t) = \frac{1}{8} P_{in}(t) \cdot \left[G_{cp}^{UA}(t) + G_{cp}^{LA}(t) - 2 \cdot \sqrt{G_{cp}^{UA}(t) \cdot G_{cp}^{LA}(t)} \cdot \cos[\varphi_{LA}(t) - \varphi_{UA}(t)] \right] \quad (7.19a)$$

$$P_C(t) = \frac{1}{8} P_{in}(t) \cdot \left[G_{cp}^{LA}(t) + G_{cp}^{UA}(t) - 2 \cdot \sqrt{G_{cp}^{UA}(t) \cdot G_{cp}^{LA}(t)} \cdot \cos[\varphi_{LA}(t) - \varphi_{UA}(t)] \right] \quad (7.19b)$$

The numerical model derived above was simulated using the parameters listed in Table 7.1 along with the optimised parameters determined in the previous section, and the output for the key stages of the switching function catalogued in Figures 7.7 through 7.12.

Figure 7.7 shows the power profile $P_{in}(t)$ of the all-one pulse train incident to the SMZ switch. The peak power of each pulse, the associated FWHM pulse width and data rate are 1 μW, 4 ps and 40 Gbit/s, respectively. The control pulses injected to both arms of the switch, see Figure 7.8, have peak power of 5 W and have the same FWHM pulse width and data rate as the signal, resulting in an average control pulse energy of ~23 pJ. The 0.1 ns offset between the start of the control pulses in each arm effectively determines that four out of the 512 bits are to be switched at the output of the device.

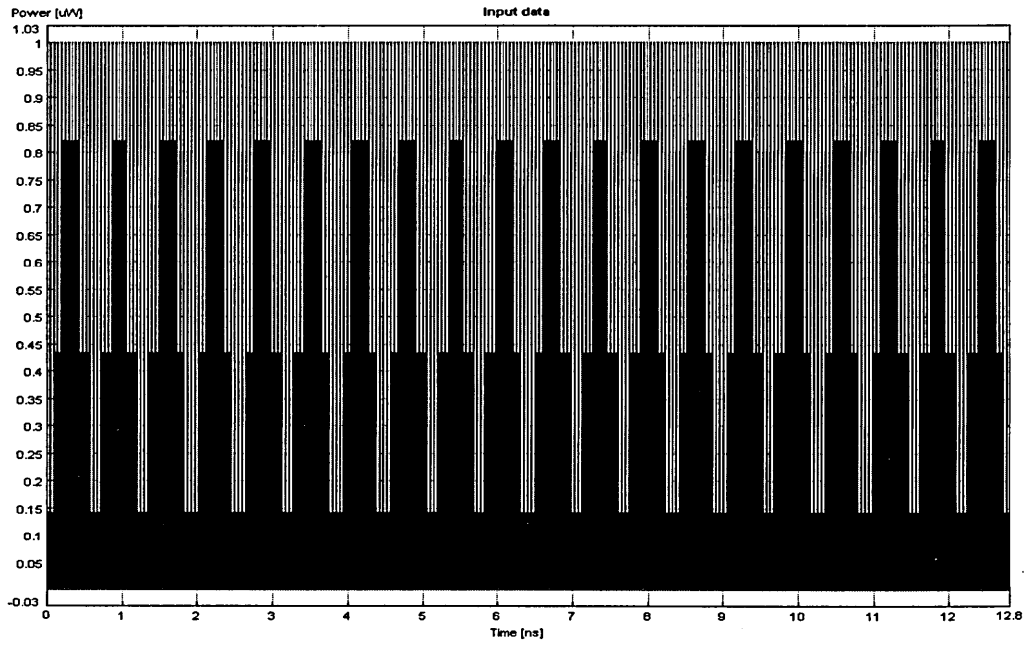

Figure 7.7 Incident power $P_{in}(t)$ to SMZ switch

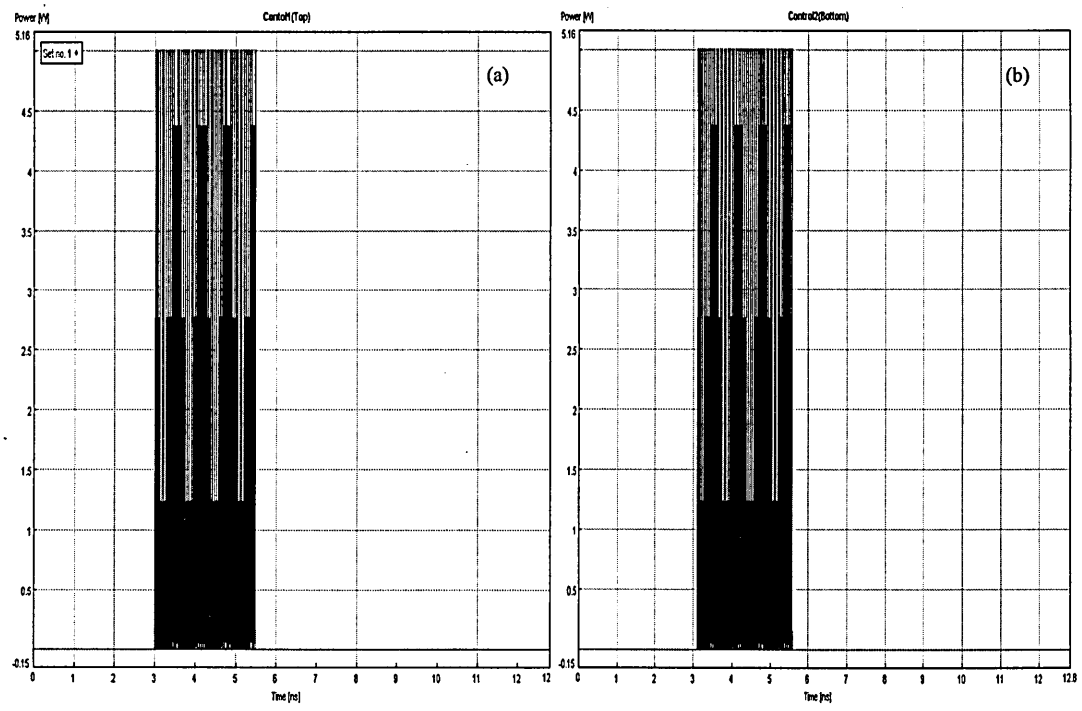

Figure 7.8 Control pulses at the input of the; (a) upper arm, and (b) lower arm of the SMZ switch

Figures 7.9 and 7.10 show the power and phase profiles after SOA1 ($P_{out}^{UA}(t)$) and SOA2 ($P_{out}^{LA}(t)$), respectively. Firstly, observe that the power depletion in each arm coincides with the onset of the control pulses. Secondly, note the inherent phase difference of 90° between each arm (directly observable at the peak phase values), is a result of the coupling action. Lastly, observe that the power and relative phase in both arms and are identical until the onset of the control pulses. Furthermore, the 0.1 ns delay in the lower arm results in an equivalent phase change delay. These key factors are responsible for the switched output observed at port B (Figure. 7.11) and port C (Figure. 7.12), respectively. More specifically, there is no information present at port B prior to the control pulses, as the phase relationship dictates that everything is reflected to the output port C. Furthermore the output at port C is doubled as is inferred by the first two terms in (7.19). The switched output at port B occurs in the time window between the control pulses. Observe that the same pulses are also present at port C with similar peak intensities as the 50:50 couplers split the switched data. Finally observe that the sum of the peak intensities for the 4-bit switched window target at both ports B and C is only 30 mW, which is half of the reflected output. This is due to the third term within the square brackets of equation(s) 7.19. In the next section, crosstalk at the closing end of the switching window will be investigated.

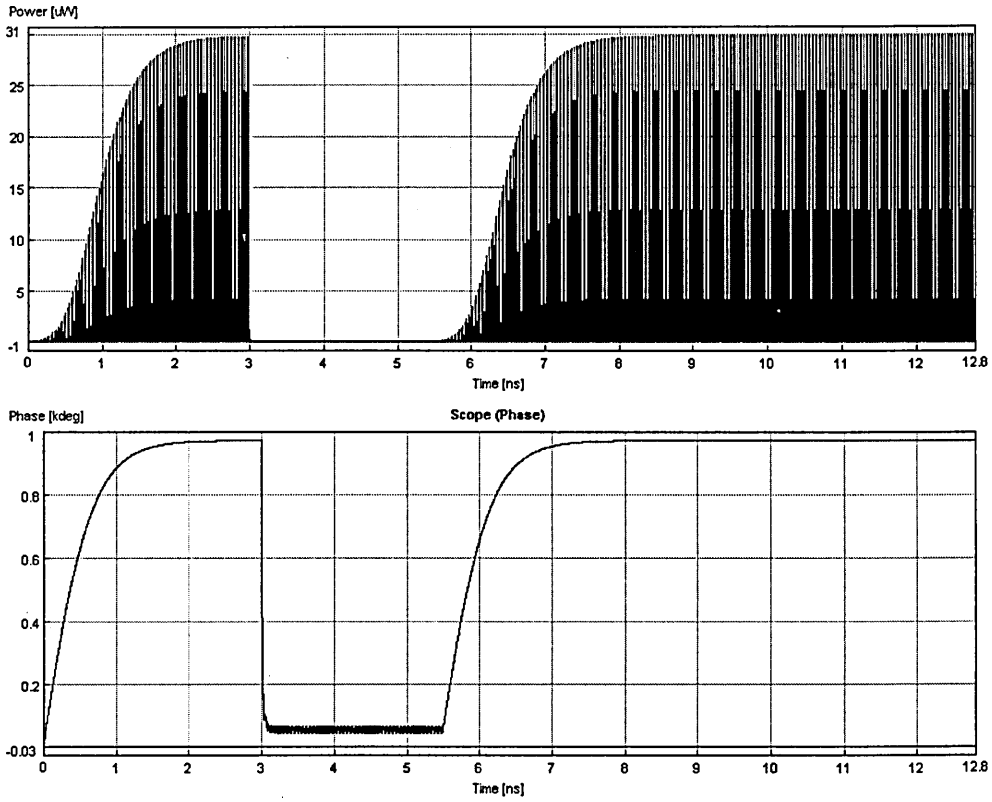

Figure 7.9 Output power $P_{out}^{UA}(t)$, and the phase of pulses after SOA1

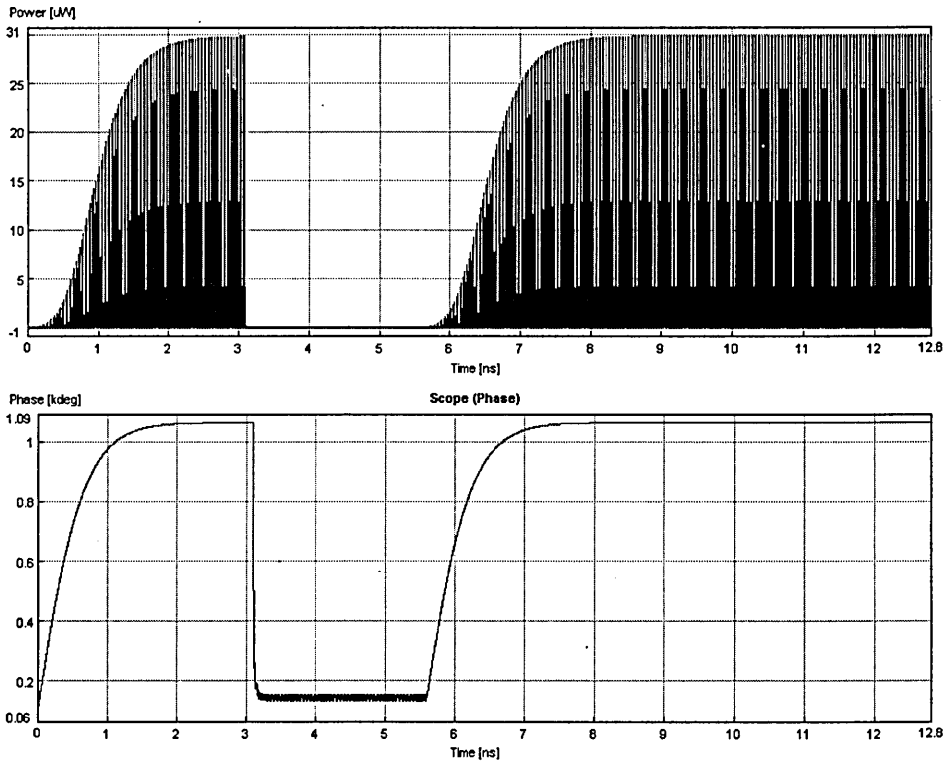

Figure 7.10 Output power $P_{out}^{LA}(t)$, and the phase of pulses after SOA2

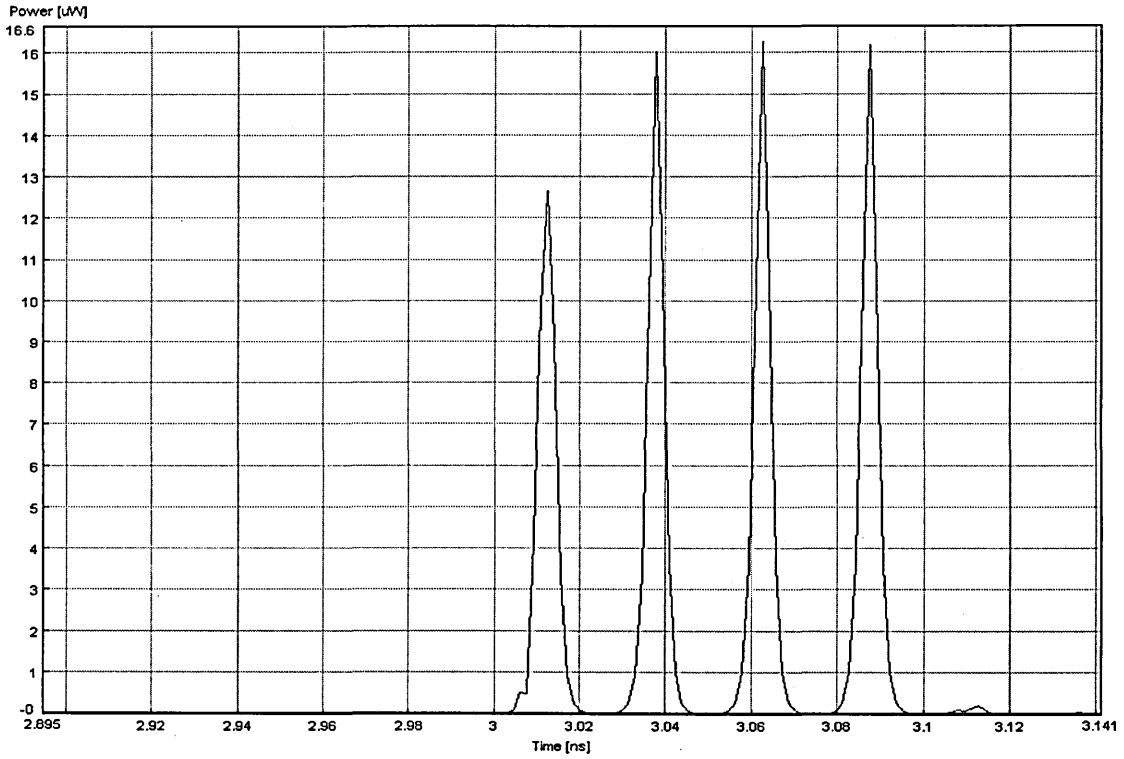

Figure 7.11 Output power at port B $P_B(t)$

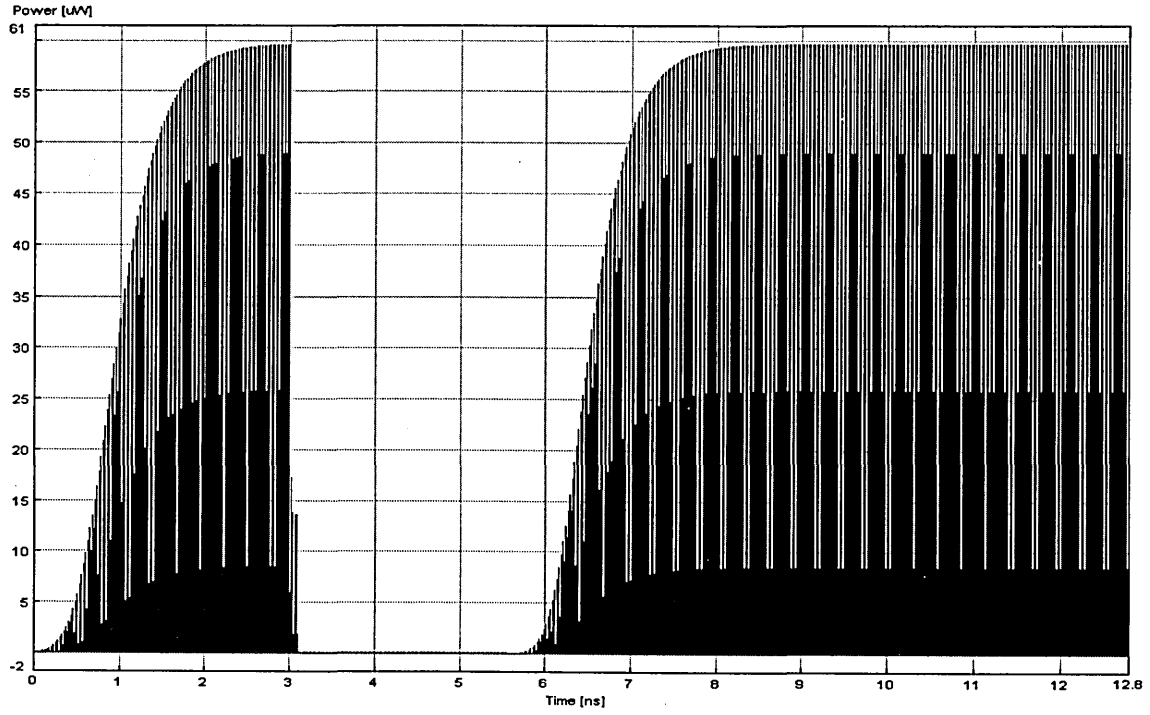

Figure 7.12 Output power at port C $P_C(t)$

7.6 Simulated Buffer Characteristics

The system model illustrated in Figures.7.5 and 7.6 was simulated using the VPI Virtual Photonics™ software package. The major system parameters used for the simulation are listed in Table 7.2. Using these parameter settings the time taken for one loop traversal (i.e. unit delay) is 100 ns.

Table 7.2 Simulation parameters for the recirculating buffer employing a SMZ switch

Parameter	Value	SOA Parameters	Value
Fibre length	20 m	Injection current	0.15 A
Fibre dispersion	0.7846×10^{-6} sm^{-2}	SOA Length	500.0×10^{-6} m
Non-linear index	3.2×10^{-20} $m^e W^{-1}$	Active area	3.2×10^{-13} m^2
Fibre core area	50.0×10^{-12} m^2	Confinement factor	0.15
Data pulse duration (FWHM)	4×10^{-12} s	Differential gain	2.78×10^{-20} m^2
Control pulse duration (FWHM)	4×10^{-12} s	Transparent carrier density	1.4×10^{24} m^{-3}
Control pulse Peak power	5 W	Linewidth enhancement factor	5.0
Data pulse peak power	1e-6 W	Recombination const A	1.43×10^{8} s^{-1}
Couple factor	0.5	Recombination const B	1.0e-16 $m^3 s^{-1}$
Bit Rate	40×10^{9} bit/s	Recombination const C	3.0e-41 $m^6 s^{-1}$

Initially, two simulation scenarios investigating switching properties of the SMZ were undertaken. First, a single laser source was used to generate a train of control pulses. A Y-splitter was then employed to produce the CP1 and CP2 pulses. Secondly, two separate laser sources were employed to produce the control pulse trains. The operating conditions of the first and second scenarios will now be referred to as the joint- and independent- source modes, respectively. Note that in both cases, a train of '1' bits

logically representing a series of closely spaced N-bit (N = 2,3,...) packets (see Figure. 7.7) was initially input to the switch.

Figure 7.13 shows a 4-bit data packet switched to port B using the joint mode operation. Observe that the first bit of the packet is slightly attenuated with respect to the other bits within the packet. This is due to the slight gain and phase difference experienced at the edge of the switching window due to the misalignment between the control and data pulses. Subsequent realignment of the packet within the switching window prevents this from acquiring a cumulative effect on recirculating around the buffer and highlights an important point regarding synchronisation. Also observed in Figure 7.13 is a 'delayed' crosstalk contribution, which is due to the tail of the *CP*2 control pulses extending beyond that of the *CP*1 control pulses, creating different gain and phase components at coupler c4.

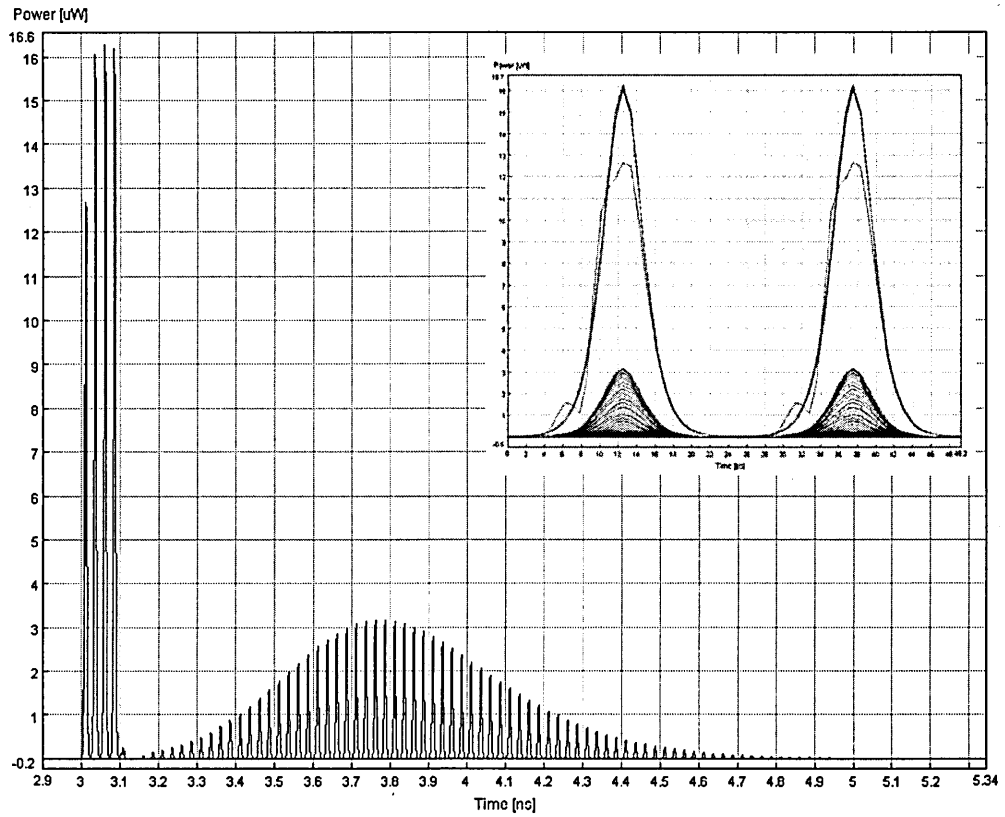

Figure 7.13 Output at SMZ port B employing the joint operation mode

The eye diagram inset in Figure 7.13 shows the effect of crosstalk on the eye opening. Here the peak crosstalk contribution is 3.1 μW. Increasing the number of control pulses from the single source only serves to delay the occurrence of the crosstalk. Moreover, the crosstalk grows rapidly with increasing the packet size, and on every loop circulation. Eventually, power levels may increase to a level that damages the integrity of the fibre. The continual crosstalk growth results in a decreased signal-to-crosstalk ratio and is illustrated in Figure 7.14 where the normalised signal-to-crosstalk energy ratio X_{ratio} is plotted as a function of loop number, where X_{ratio} is defined as:

$$X_{ratio} = \frac{1}{t_{packet}} \cdot \int_{0}^{t_{packet}} P(t)\,dt \Bigg/ \frac{1}{(t_{sw} - t_{packet})} \cdot \int_{t_{packet}}^{t_{sw}} P(t)\,dt, \qquad (7.20)$$

where the optical power, packet duration and temporal switching window width are denoted by $P(t)$, t_{packet} and t_{sw}, respectively.

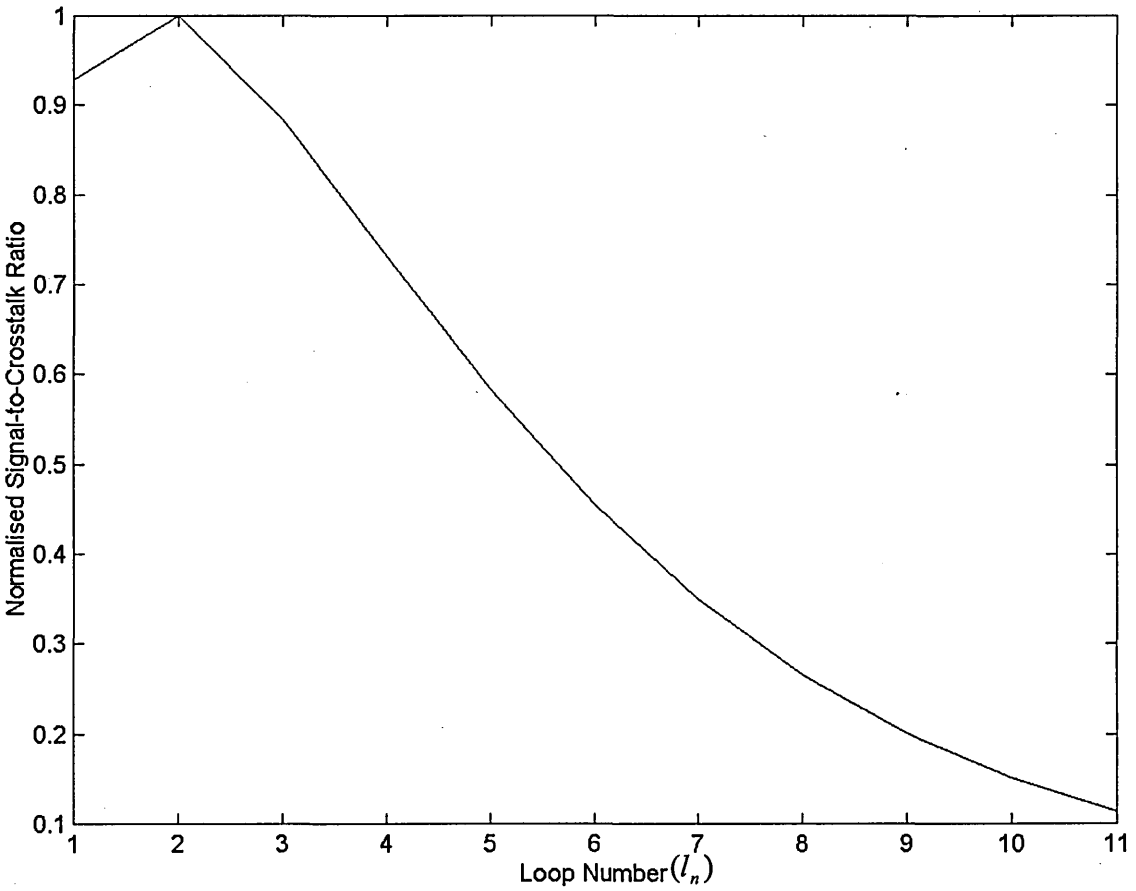

Figure 7.14 Normalised crosstalk energy ratio against the loop number (joint mode)

For loop number greater than 2, the signal-to-crosstalk ratio decreases rapidly. This is due to the rapid growth of the crosstalk within the switching window.

This mode of operation would be acceptable for switching/demultiplexing single bits from an ultra-high bit rate stream. However, in the context of a buffer, where the number of bits to be switched is greatly increased, this mode of operation is less desirable. Moreover it is only advised if the time span occupied by the intended buffered bits (i.e. excluding the delayed crosstalk) is to be considered, or if the intended buffer storage time (i.e. loop circulations) is small.

A better solution, as illustrated in Figure 7.15, encapsulates the data packet within the control pulses while ensuring that the control pulses in both arms terminate

concurrently. This method attempts to synchronise the carrier density recovery of each SOA so as to obtain a square-switching window.

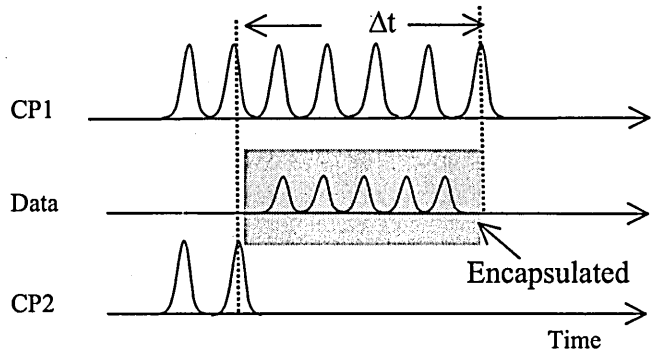

Figure 7.15 Waveform diagram showing packet encapsulation

Figure 7.16 shows a 16-bit data packet switched to port B using the joint mode operation. The peak powers of the pulses serve to indicate that the profile of the switching window is relatively square. The eye diagram inset in Figure 7.16 shows that the peak crosstalk contribution has been dramatically reduced to a value of <0.2 μW.

An investigation of the normalised X_{ratio} under this operational mode reveals that crosstalk outside the temporal packet boundary is reduced on each loop circulation. This is highlighted in Figure 7.17 where multiple loop traversals of a 16-bit packet is considered.

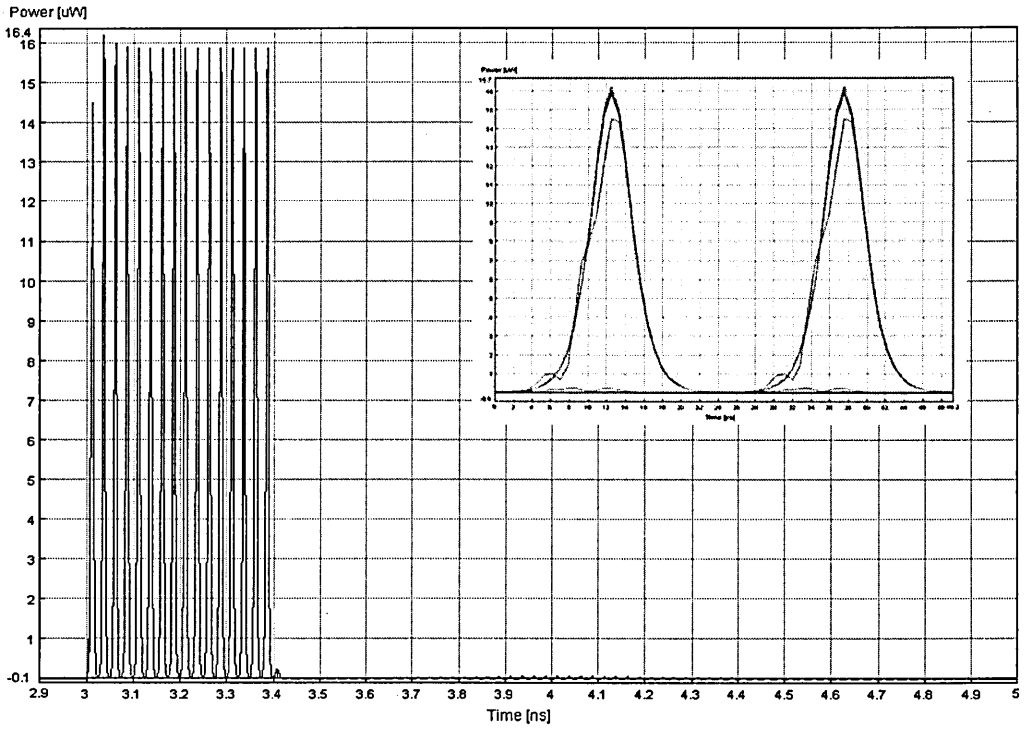

Figure 7.16 Output at SMZ port B employing the independent operation mode

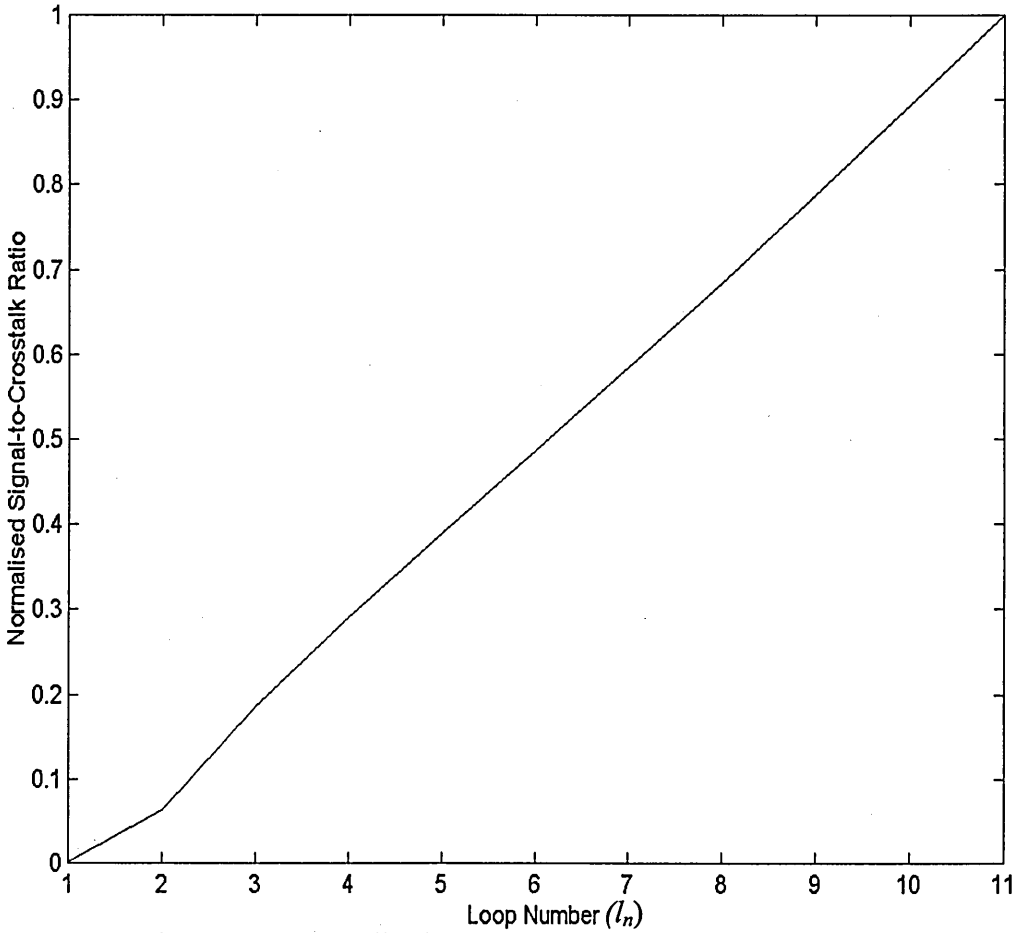

Figure 7.17 Normalised crosstalk energy ratio against the loop number (independent mode)

Figure 7.18 shows the output from the buffer after storing the 16-bit packet for 10 loop traversals (1 μs). Although the switching window profile is not completely square, simulation evidence suggests that the peak-amplitude of the constituent data pulses can be made equal by extending the switching windows and aligning the buffered packet accordingly.

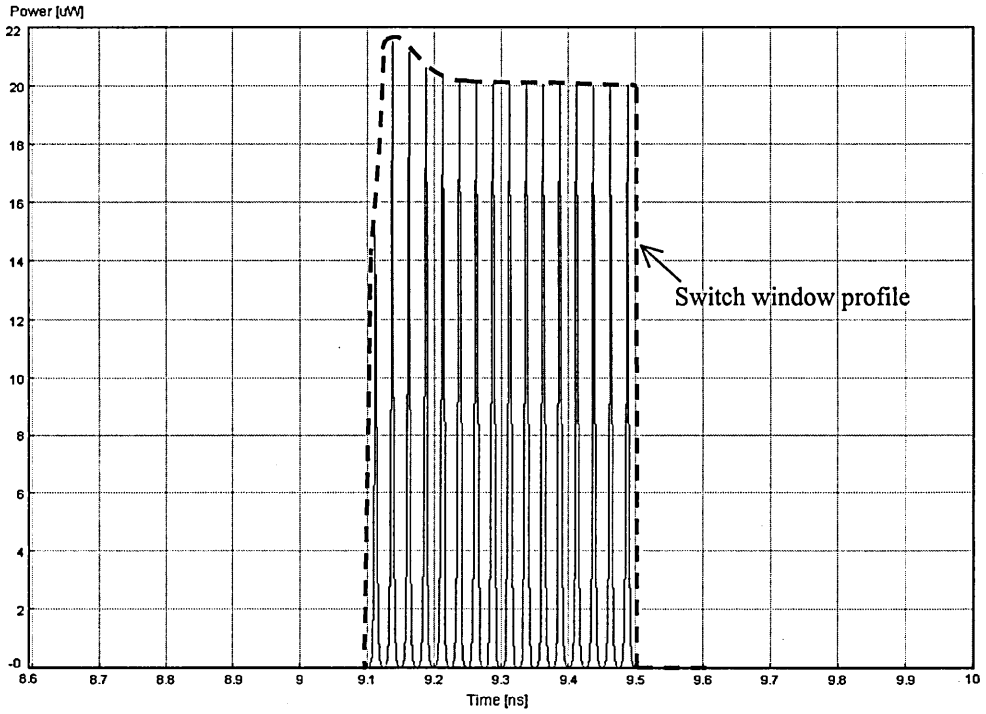

Figure 7.18 Buffer output after 10 loop circulations

7.7 Summary

In this chapter, a novel operation of the symmetric Mach-Zehnder switching architecture that does not rely on achieving a π-phase change to effect switching has been presented. The application of such a switch has wide implications especially in the

optical broadcast networks. This architecture was employed to develop an all-optical fibre loop buffer suitable for use in optical time division multiplexed networks. Simulation results showed the successful implementation of the buffer and highlighted the far-reaching benefits of buffers employing this switching technique especially as it relates to buffering packets of varying length. In addition, it is shown that the architecture can be configured in such a way to effectively reduce the inter-packet crosstalk at the edges of the switching window profile.

Chapter 8

Conclusions and Future Work

8.1 Conclusions

The primary objective of this work was to model and analyse an all-optical recirculating fibre loop buffer, which was suitable for use within high-speed all-optical networks. Such networks would remove the inherent bottlenecks associated with first- and second-generation optical networks. The literature review in Chapter 2 highlighted history of this transition and also discussed the technological advances that precipitated the transition to the third-generation optical networks in existence today. More specifically, the development of WDM and OTDM technologies and their associated implementation challenges were discussed. Although most of the research to date has concentrated on the WDM technologies, it is believed that OTDM networks are excellent candidates for meeting the bandwidth demands of future ultra-fast networks. Therefore this work has focused on the development of a buffering architecture that is suitable for OTDM communications systems.

The crucial components required to develop a basic buffering architecture include a switching mechanism and a loop of optical fibre. As the performance of the buffer critically relies on the characteristics of these components, they were the subject of chapters 3 and 4, respectively.

In Chapter 3, many optical switching device candidates were presented including several interferometric configurations. The important evaluation criteria were switching time, repetition rate, control pulse energy (where applicable) and practicality. The restriction on switching times and repetition rates automatically excluded MEMS, bubble, liquid crystal and electro-holographic switches from consideration, as they are better suited to TONs. From the review, it may be concluded that the best switching architectures are the TOAD and the SMZ, as they have similar noise figure characteristics, exhibit low control energy requirements (0.25 pJ) and are highly integratable. In addition, both architectures have fast switching times (< 1ps) and high repetition rates (100+ GHz). The operation principle of the TOAD and the SMZ is based on the non-linear properties of the SOA. However, in the former, the temporal duration of the switching window is determined by the asymmetrical offset of the SOA from the centre of the loop, whereas it is determined by the temporal duration between the two control pulses in the latter. As the size of the switching window is coupled to physical implementation of the TOAD switch, it becomes unsuitable for the cases where variable sized packets are employed by the optical network. Consequently, the SMZ switch is used within the buffering architecture in this work to provide added flexibility. The TOAD switch is better suited for routers within the network where the sizes of the packets are more likely to be static.

In Chapter 4, the equation governing the propagation of light waves within optical fibre was presented. As the exact solution to this equation is difficult to determine in the presence of the fibre loss and higher order non-linear terms, a numerical algorithm called the beam propagation method was introduced to enable the computational simulation of (data) pulses within SMF. In particular, soliton (data) pulses were

modelled to highlight their inherent properties. Namely, the collision between soliton pulses is elastic, and the profile of fundamental solitons do not change over the propagation distance making them ideal for data transmission in high-speed optical networks. However, there are limits placed on the maximum bits rates and peak powers as the integrity of the information critically relies on the relative phase and distance between adjacent soliton pulses. If the pulses are too closely, spaced then inter-soliton forces caused them to oscillate about their centre position. This has implications that can lead to an increased BER at the receiver in a communications system.

In Chapter 5, the key components of the RFLB were combined to model a passive version of the device using the MATLAB software package. Initially, the BER performance was investigated using both soliton and Gaussian-soliton wave profiles under the assumption that the switching architecture was assumed ideal. The simulation results showed that the performances of both pulses were similar. However, it should be noted that the initial contraction of the Gaussian-soliton pulse might have implications in decreasing the effects of crosstalk caused by neighbouring pulses. The theoretical equation developed to analyse the BER performance of the passive RFLB was one of the original contributions of this work. Relaxing the assumptions about the switch highlighted the need to employ a mechanism to compensate for both the intrinsic fibre and switch insertion losses in order to maintain the peak powers required for soliton propagation. This was the primary focus in Chapter 6, where an optical amplifier was introduced into the fibre loop. The VPI transmission software package was employed to model the active RFLB. This powerful package uses a graphical user interface, which makes design of complex architectures easy to implement, and is a well known and respected tool used by engineers within the optical communications industry.

Simulation results confirmed that the active RFLB was capable of providing longer storage times than the passive version. However, the performance was limited by the accumulation of the ASE noise and the timing jitter due to the amplification element. Moreover, these simulation results were found to match those predicted by the mathematical model, which was developed to determine the BER performance over several loop traversals. This work was another original contribution of this thesis.

Evidence of the importance of the pre-buffer amplifier in minimising the intensity fluctuations caused by the switch was also presented in Chapter 6. Simulation results showed that the absence of the pre-buffer amplifier resulted soliton breathing. Moreover, the associated peak power (/intensity) fluctuations are bit rate and bit pattern dependent. This has strong implication for optimising the RFLB design to achieve the best BER performance. Further optimisation of the BER performance was achieved by using an optical band-pass filter to reduce the accumulation rate of ASE noise. Simulation results showed that for low loop traversal numbers (<100) there is no marked improvement in performance, however there is a performance gain of ~0.21 dB at BER of 10^{-9} when the loop traversal number is 400.

A more comprehensive implementation of the RFLB detailing the SMZ switching architecture was presented in Chapter 7. As the operation of the SMZ critically relies on the non-linearity produced by the SOA, a mathematical model for this device was first presented. This model was then used to optimise the physical parameters of the SOA device for use in the SMZ architecture.

The numerical model developed to describe the novel approach employed to effect switching removed the reliance of a relative π-phase change and has wide implications especially in the optical broadcast networks. This new approach was based on the joint- and independent modes of operation. Simulation results showed that the latter mode is more effective at reducing inter-packet crosstalk. Furthermore, when employed within the RFLB the quantity of inter-packet crosstalk is observed to decrease with increasing loop traversals.

In summary, this thesis has presented the design, analysis, and simulation results of recirculating fibre loop buffers suitable for use in OTDM networks. The primary objective of this study was to investigate the potential and limitations of such buffers within high-speed lightwave systems. The storage times (i.e. loop traversals), noise and crosstalk characteristics of the buffer have been addressed.

8.2 Further work

In this section, the remaining outstanding issues and potential improvements that are believed to be interesting and deserve future investigation are presented.

In this study, either normal step index fibre or dispersion-shifted fibre has been employed to form the buffer loop. Future work however may extend to other fibre types, such as dispersion decreasing fibre and highly non-linear fibre to investigate their effect of the buffer performance. Moreover, a combination of the fibre types with different

contributing lengths may also be explored with a view to minimise the effects of chromatic dispersion.

The inclusion of a 3R optical regeneration unit within the RFLB architecture to avoid the pulse distortion, which is inevitable in RFLBs, presents another interesting area of study. The aim would be to improve BER performance and to extend the storage time by reducing the inherent dispersion effects caused by the fibre and the ASE noise accumulation caused by the in-loop optical amplification, which ultimately result in the destruction of the pulses. Careful design of the buffer could yield an architecture in which optical regeneration is avoided on each successive traversal of the buffered data around the loop. As optical regeneration is unnecessary at every loop traversal instance when relatively short fibre loops (500m) are used, it would be appropriate to investigate an optimal regeneration period. This would be the maximum number of times the packet can traverse the loop between regeneration instances before regeneration adversely affects the BER performance.

Extending the basic recirculating buffer architecture to include several ports, where each port is essentially a 2x2 switch would result in a multi-buffer architecture. This structure would be analogous to a traffic roundabout or ring network where incident packets can exit at different ports. Such architectures would be able to exhibit both buffering and routing capabilities. However, a detailed study would be required to determine such things as the packet header format and the necessary algorithm(s) required for effective packet control. Computer simulations could then be employed to investigate the scalability and crosstalk limitations of such a buffer design.

This thesis investigated the performance characteristics of the passive and active RFLB architectures. However, the performance of these (unit) buffers is yet to be investigated in the context of an actual optical network scenario. Performance criteria such as crosstalk, noise accumulation and the associated timing jitter, packet loss, scalability and BER would give further insights into the practicality of RFLBs.

Another avenue of exploration is packet reordering or priority buffering within optical networks. Suggestions for two network candidate types are the point-to-point distributed networks (e.g. Manhattan Street Network) and broadcasts networks (e.g. Hierarchical Local Area Network (HLAN)). The logical topologies of MSNs and HLANs are suitable test candidates as they are relatively simple to simulate and are readily suitable for different buffering schemes. Such alternative buffering strategies may include input-, output- and shared buffering where RFLBs are employed as the unit buffer type. Results from such a study would highlight where, and under which schemes RFLBs are best deployed. This work will require the development of routing and scheduling algorithms that are best suited for the network topology, buffer architecture and buffering scheme employed.

Moreover, schemes which utilise combinations of optical buffering, wavelength conversion, store-and-forward and deflection routing, may be used to extend the RFLB's applicability to WDM networks. An area for future study would be to investigate which schemes offer low implementation complexity, low packet loss ratio, low packet delay and high network throughput, depending on the requirements of several network topologies. In this investigation consideration should be given to different traffic dynamics, (i.e. uniform, normal, bursty, etc) as this may influence the performance of the schemes under consideration [160;161].

An alternative RFLB design consisting of a 3-port circulator and two (tuneable) fibre Bragg gratings (FBG) all interconnected with optical fibre may provide a buffer with increased flexibility. Conceptually, the first port of the circulator would provide for input (/output) to (/from) the buffer, whereas the remaining ports are connected to fibre pigtails with FBGs at each end, effectively forming an optical mirror. That is, pulses entering the buffer would continually be reflected between the FBGs until they are allowed to exit via the circulator. The advantages of such a design would be that the FBGs provide better scalability in the WDM domain than the original RFLB proposed in this thesis. Moreover, the FBGs would reduce the amount of ASE noise when optical amplifiers are introduced to the architecture. Extending the basic FBG-based recirculating buffer architecture to form a multi-buffer architecture would also be deserving of further investigation.

It was not a requirement of this work to implement all-optical buffer architecture in hardware. However, it is recommended that future research work should undertake a hardware design and implementation so that measurements can be taken for comparison with the simulated and theoretical contributions of this thesis. For systems using the same parameters, these comparisons are expected to agree closely. The added advantage(s) of a hardware implementation would be the ability to easily investigate the physical effects, such as temperature, on the system BER performance.

The future solution to the optical buffering problem must avoid complex control mechanisms and large processing overheads. The ideal candidate solution must also be

highly scalable with respect to the buffer storage capacity and storage time. In the absence of the optical equivalent to random access memory, recirculating buffers are currently the best candidates to meet this need although they require complex control algorithms. A novel technique that manages to slow down light thereby effecting a delay, may yet revolutionalise optical buffer techniques [162]. The author ultimately believes that further study in the optical buffering should exploit these revelations to produce the next generation of optical buffers.

REFERENCES

[1] Hines, I. J., *ATM - The Key to Hige-Speed Boradband Networking* M&T Books, 1996.

[2] Tanenbaum, A. S., *Computer Networks*, 3 rd ed. Prentice Hall, 1996.

[3] Prycker, M., *Asynchronous Transfer Mode - Solution for Broadband ISDN* Prentice Hall, 1995.

[4] Hui, J. Y., *Switching and Traffic Theory for Integrated Broadband Networks* Kluwer Academic Publishers, 1990.

[5] Halsall, F., *Data Communications Computer Networks and Open Systems* Addison-Wesley, 1996.

[6] Black, U., *Emerging Communications Technologies*, 2nd ed. Prentice Hall Series in Advanced Communications Technologies, 1997.

[7] Ramaswami, R. and Sivarajan, K. N., *Optical Networks - A Practical Persoective*, Second ed. Morgan Kaufmann Publishers, 2002.

[8] Smith, D. W., *Optial Network Technology*, First ed. Chapman & Hall, 1995.

[9] Midwinter, J. E., "The start of optical fiber communications as seen from a U.K. perspective," *Selected Topics in Quantum Elèctronics, IEEE Journal on*, vol. 6, no. 6, pp. 1307-1311, 2000.

[10] Agrawal, G. P., *Applications of Nonlinear Fiber Optics* Academic Press, 2001.

[11] Agrawal, G. P., *Fiber-Optic Communication Systems*, Second ed. Wiley, 1997.

[12] Smith, R. G., "Optical Power Handling Capacity of Low Loss Optical Fibers as Determined by Stimulated Raman and Brillouin Scattering," *Applied Optics*, vol. 11, no. 68, pp. 2489-2494, 1972.

[13] Mao, X. P., Tkach, R. W., Chraplyvy, A. R., Jopson, R. M., and Derosier, R. M., "Stimulated Brillouin threshold dependence on fiber type and uniformity," *IEEE Photonics Technology Letters*, vol. 4, no. 1, pp. 66-69, 1992.

[14] Okuno, T. and Nishimura, M., "Effects of stimulated Raman amplification in optical fibre on stimulated Brillouin scattering threshold power," *Electronics Letters*, vol. 38, no. 1, pp. 14-16, 2002.

[15] Hansryd, J., Dross, F., Westlund, M., Andrekson, P. A., and Knudsen, S. N., "Increase of the SBS threshold in a short highly nonlinear fiber by applying a temperature distribution," *Lightwave Technology, Journal of*, vol. 19, no. 11, pp. 1691-1697, 2001.

[16] Chraplyvy, A. R. and Tkach, R. W., "What is the actual capacity of single-mode fibers in amplified lightwave systems?," *IEEE Photonics Technology Letters*, vol. 5, no. 6, pp. 666-668, 1993.

[17] Fishman, D. A. and Nagel, J. A., "Degradations due to stimulated Brillouin scattering in multigigabit intensity-modulated fiber-optic systems," *Lightwave Technology, Journal of*, vol. 11, no. 11, pp. 1721-1728, 1993.

[18] Aoki, Y., Tajima, K., and Mito, I., "Input power limits of single-mode optical fibers due to stimulated Brillouin scattering in optical communication systems," *Lightwave Technology, Journal of*, vol. 6, no. 5, pp. 710-719, 1988.

[19] Montes, C. and Rubenchik, A. M., "Information rate limit due to stimulated Brillouin scattering for transmission capacity in soliton-based optical-fibre communications," *Non-Linear Effects in Fibre Communications, IEE Colloquium on*, pp. 13-1-13/3, 1990.

[20] Hamilton, S. A., Robinson, B. S., Murphy, T. E., Savage, S. J., and Ippen, E. P., "100 Gb/s optical time-division multiplexed networks," *Lightwave Technology, Journal of*, vol. 20, no. 12, pp. 2086-2100, 2002.

[21] Mollenauer, L. F., Lichtman, E., Harvey, G. T., Neubelt, M. J., and Nyman, B. M., "Demonstration of error-free soliton transmission over more than 15000 km at 5 Gbit/s, single-channel, and over more than 11000 km at 10 Gbit/s in two-channel WDM," *Electronics Letters*, vol. 28, no. 8, pp. 792-794, 1992.

[22] Nakazawa, M., Suzuki, K., and Yamada, E., "20 Gbit/s, 1020 km penalty-free soliton data transmission using erbium-doped fibre amplifiers," *Electronics Letters*, vol. 28, no. 11, pp. 1046-1047, 1992.

[23] Kogelnik, H., "High-capacity optical communications: personal recollections," *Selected Topics in Quantum Electronics, IEEE Journal on*, vol. 6, no. 6, pp. 1279-1286, 2000.

[24] Mikkelsen, B., Raybon, G., Essiambre, R.-J., Johnson, J. E., Dreyer, K., and Nelson, L. F., "Unrepeatered transmission over 150 km of nonzero-dispersion fibre at 100 Gbit/s with semiconductor based pulse source, demultiplexer and clock recovery," *Electronics Letters*, vol. 35, no. 21, pp. 1866-1868, 1999.

[25] Kawanishi, S., Takara, H., Uchiyama, K., Saruwatari, M., and Kitoh, T., "Fully time-division-multiplexed 100 Gbit/s optical transmission experiment," *Electronics Letters*, vol. 29, no. 25, pp. 2211-2212, 1993.

[26] Morioka, T., Kawanishi, S., Takara, H., and Kamatani, O., "Penalty-free, 100 Gbit/s optical transmission of <2ps supercontinuum transform-limited pulses over 40 km," *Electronics Letters*, vol. 31, no. 2, pp. 124-125, 1995.

[27] Kawanishi, S., Takara, H., Kamatani, O., and Morioka, T., "100 Gbit/s, 500 km optical transmission experiment," *Electronics Letters*, vol. 31, no. 9, pp. 737-738, 1995.

[28] Yamamoto, T., Yamamoto, T., and Nakazawa, M., "Third- and fourth-order active dispersion compensation using a phase modulator in a terabit/s OTDM transmission," 2001, pp.WH6-1.

[29] Nakazawa, M., Yamamoto, T., and Tamura, K., "Ultra high speed OTDM transmission using femtosecond pulses," 2001, pp.I-618.

[30] Nakazawa, M., Yamamoto, T., and Tamura, K. R., "1.28 Tbit/s-70 km OTDM transmission using third- and fourth-order simultaneous dispersion compensation with a phase modulator," *Electronics Letters*, vol. 36, no. 24, pp. 2027-2029, 2000.

[31] Tucker, R. S., Eisenstein, G., and Korotky, S. K., "Optical time-division multiplexing for very high bit-rate transmission," *Lightwave Technology, Journal of*, vol. 6, no. 11, pp. 1737-1749, 1988.

[32] Furst, C., Mohs, G., Gelger, H., and Fischer, G., "Performance limits of nonlinear RZ and NRZ coded transmission at 1O and 40 Gb/s on different fibers," *Proceedings of Optical Fiber Communication Conference and Exhibit*, OFC 2000 Baltimore, Maryland USA 2000, pp.302-304.

[33] Zhu, B., Leng, L., Nelson, L. E., Qian, Y., Cowsar, L., Stulz, S., Doerr, C., Stulz, L., Chandrasekhar, S., Radic, S., Vengsarkar, D., Chen, Z., Park, J., Feder, K. S., Thiele, H., Bromage, J., Gruner-Nielsen, L., and Knudsen, S., "3.08 Tbit/s (77×42.7 Gbit/s) WDM transmission over 1200 km fibre with 100 km repeater spacing using dual C- and L-band hybrid Raman/erbium-doped inline amplifiers," *Electronics Letters*, vol. 37, no. 13, pp. 844-845, 2001.

[34] Zhu, B., Leng, L., Nelson, L. E., Qian, Y., Cowsar, L., Stulz, S., Doerr, C., Stulz, L., Chandrasekhar, S., Radic, S., Vengsarkar, D., Chen, Z., Park, J., Feder, K. S., Thiele, H., Bromage, J., Gruner-Nielsen, L., and Knudsen, S., "3.08 Tb/s (77/spl times/42.7 Gb/s) transmission over 1200 km of non-zero dispersion-shifted fiber with 100-km spans using C and L-band distributed Raman amplification," *Proceedings of Optical Fiber Communication Conference and Exhibit*, OFC '01 Anaheim, California USA 2001, pp.D23.

[35] Nuss, M. C., Knox, W. H., and Koren, U., "Scalable 32 channel chirped-pulse WDM source," *Electronics Letters*, vol. 32, no. 14, pp. 1311-1312, 1996.

[36] Boivin, L., Nuss, M. C., Knox, W. H., and Stark, J. B., "206-channel chirped-pulse wavelength-division multiplexed transmitter," *Electronics Letters*, vol. 33, no. 10, pp. 827-829, 1997.

[37] Knox, W. H., "Ultrafast technology in telecommunications," *Selected Topics in Quantum Electronics, IEEE Journal on*, vol. 6, no. 6, pp. 1273-1278, 2000.

[38] Chang, C.-C., Sardesai, H. P., and Weiner, A. M., "Code-division multiple-access encoding and decoding of femtosecond optical pulses over a 2.5-km fiber link," *IEEE Photonics Technology Letters*, vol. 10, no. 1, pp. 171-173, 1998.

[39] Maxemchuk, N. F., "Comparison of deflection and store-and-forward techniques in the Manhattan Street and Shuffle-Exchange Networks," *Proceedings of the*

Eighth Annual Joint Conference of the IEEE Computer and Communications Societies. Technology: Emerging or Converging?, INFOCOM '89 Ottawa, Ont. Canada 1989, pp.800-809.

[40] Bononi, A., Forghieri, F., and Prucnal, P. R., "Analysis of one-buffer deflection routing in ultra-fast optical mesh networks," *Proceedings.Twelfth Annual Joint Conference of the IEEE Computer and Communications Societies. Networking: Foundation for the Future*, INFOCOM '93 San Francisco, CA USA 1993, pp.303-311.

[41] Seung-Woo, Seo and Prucnal, P. R., "On the performance of a class of multihop shuffle networks," *Proceedings of IEEE International Conference on Communications: Gateway to Globalization*, ICC ' 95. Seattle, WA USA 1995, pp.1211-1215.

[42] Shabeer, M., Lucek, J. K., Smith, K., Cotter, D., and Rogers, D. C., "Self-synchronisation scheme for high-speed photonic networks," *Electronics Letters*, vol. 31, no. 17, pp. 1476-1478, 1995.

[43] Gao, R., Ghassemlooy, Z., and Ball, P., "Crosstalk analysis for all optical routers," Stafford, U.K., 15-17 July 2002, pp.173-176.

[44] Nelson, B. P., Blow, K. J., Constantine, P. D., Doran, N. J., Lucek, J. K., Marshall, I. W., and Smith, K., "All-optical Gbit/s switching using nonlinear optical loop mirror," *Electronics Letters*, vol. 27, no. 9, pp. 704-705, 1991.

[45] Ngah, R., Ghassemlooy, Z., Swift, Ahmed T., and Ball, P., "Simulation of an all optical time division multiplexing router employing TOADs," Liverpool, UK, 17-18 June 2002, pp.415-420.

[46] Yu, B. Y., Runser, R., Toliver, P., Deng, K.-L., Zhou, D., Chang, T., Seo, S. W., Kang, K. I., Glesk, I., and Prucnal, P. R., "Network demonstration of 100 Gbit/s optical packet switching with self-routing," *Electronics Letters*, vol. 33, no. 16, pp. 1401-1403, 1997.

[47] Cotter, D., Lucek, J. K., Shabeer, M., Smith, K., Rogers, D. C., Nesset, D., and Gunning, P., "Self-routing of 100 Gbit/s packets using 6 bit `keyword' address recognition," *Electronics Letters*, vol. 31, no. 25, pp. 2201-2202, 1995.

[48] Ki-Hwan Park, Mizumoto, T., Matsuura, A., and Naito, Y., "All-optical address extraction for optical routing," *Lightwave Technology, Journal of*, vol. 16, no. 7, pp. 1129-1136, 1998.

[49] Toliver, P., Glesk, I., Runser, R. J., Kung-Li Deng, Yu, B. Y., and Prucnal, P. R., "Routing of 100 Gb/s words in a packet-switched optical networking demonstration (POND) node," *Lightwave Technology, Journal of*, vol. 16, no. 12, pp. 2169-2180, 1998.

[50] Houbavlis, T., Zoiros, K., Vlachos, K., Papakyriakopoulos, T., Avramopoulos, H., Girardin, F., Guekos, G., Dall'Ara, R., Hansmann, S., and Burkhard, H.,

"All-optical XOR in a semiconductor optical amplifier-assisted fiber Sagnac gate," *IEEE Photonics Technology Letters*, vol. 11, no. 3, pp. 334-336, 1999.

[51] Hall, K. L. and Rauschenbach, K. A., "All-optical bit pattern generation and matching," *Electronics Letters*, vol. 32, no. 13, pp. 1214-1215, 1996.

[52] Bintjas, C., "20 Gb/s all-optical XOR with UNI gate," *IEEE Photonics Technology Letters*, vol. 12, no. 7, pp. 834-836, 2000.

[53] Matera, F., "Proposal of all optical soliton shuffle multihop network," *Electronics Letters*, vol. 28, no. 17, pp. 1570-1571, 1992.

[54] Webb, R. P., Manning, R. J., Maxwell, G. D., and Poustie, A. J., "40 Gbit/s all-optical XOR gate based on hybrid-integrated Mach-Zehnder interferometer," *Electronics Letters*, vol. 39, no. 1, pp. 79-81, 2003.

[55] Lattes, A., Haus, H., Leonberger, F., and Ippen, E., "An ultrafast all-optical gate," *Quantum Electronics, IEEE Journal of*, vol. 19, no. 11, pp. 1718-1723, 1983.

[56] Lee, M.-H., Kang, J.-M., and Han, S.-K., "All optical signal regeneration in cascaded Mach-Zehnder interferometer wavelength converter," *Optoelectronics, IEE Proceedings-*, vol. 148, no. 4, pp. 189-194, 2001.

[57] Janz, C., "All-active dual-order mode (DOMO) Mach-Zehnder wavelength converter for 10 Gbit/s operation," *Electronics Letters*, vol. 35, no. 21, pp. 1862-1863, 1999.

[58] Ratovelomanana, F., Vodjdani, N., Enard, A., Glastre, G., Rondi, D., Blondeau, R., Joergensen, C., Durhuus, T., Mikkelsen, B., Stubkjaer, K. E., Jourdan, A., and Soulage, G., "An all-optical wavelength-converter with semiconductor optical amplifiers monolithically integrated in an asymmetric passive Mach-Zehnder interferometer," *IEEE Photonics Technology Letters*, vol. 7, no. 9, pp. 992-994, 1995.

[59] Wooten, E. L., Stone, R. L., Miles, E. W., and Bradley, E. M., "Rapidly tunable narrowband wavelength filter using LiNbO₃ unbalanced Mach-Zehnder interferometers," *Lightwave Technology, Journal of*, vol. 14, no. 11, pp. 2530-2536, 1996.

[60] Poustie, A. J., Blow, K. J., and Manning, R. J., "Storage threshold and amplitude restoration in an all-optical regenerative memory," *Optics Communications*, vol. 146, no. 1-6, pp. 262-267, Jan.1998.

[61] Poustie, A. J., Kelly, A. E., Manning, R. J., and Blow, K. J., "All-optical regenerative memory with full write/read capability," *Optics Communications*, vol. 154, no. 5-6, pp. 277-281, Sept.1998.

[62] Poustie, A. J., Blow, K. J., and Manning, R. J., "Storage threshold and amplitude restoration in an all-optical regenerative memory," *Optics Communications*, vol. 146, no. 1-6, pp. 262-267, Jan.1998.

[63] R.Dettmer, "The 100 GHz Light Switch," *IEE Review*, no. March 1999, pp. 69-71, 1999.

[64] Glesk, I., Kang K.I., and Prucnal, P. R., "Ultrafast all-optically controlled 2x2 crossbar switch," *Proceedings of IEEE Lasers and Electro-Optics Society Annual Meeting*, LEOS '96 Boston, MA USA 1996, pp.149-150.

[65] Ngah, R., Ghassemlooy, Z., and and Swift, G., "Simulation of an all optical time division multiplexing router employing symmetric Mach-Zehnder (SMZ)," Imperial College, London, UK, Sep. 8-9 2002 2003, pp.133-139.

[66] Glesk, I., Kang K.I., and Prucnal, P. R., "Ultrafast photonic packet switching with optical control," *Optics Express*, vol. 1, no. 5, pp. 126-132, 1997.

[67] Sokoloff, J. P., Prucnal, P. R., Glesk, I., and Kane, M., "A terahertz optical asymmetric demultiplexer (TOAD)," *IEEE Photonics Technology Letters*, vol. 5, no. 7, pp. 787-790, 1993.

[68] Eiselt, M., "Optical loop mirror with semiconductor laser amplifier," *Electronics Letters*, vol. 28, no. 16, pp. 1505-1507, 1992.

[69] I.Glesk, R.J.Runser, and P.R.Prurcnal, "New Generation of Devices For All-Optical Communications," *acta physica solvaca*, vol. 51, no. 2, pp. 151-162, Apr.2001.

[70] S.Nakamura, Y.Ueno, and K.Tajima, "Ultrafast (200-fs Switching, 1.5-Tb/s Demultiplexing) and High-Repetition (10 GHz) Operations of a Polarization-Discriminating Symmetric Mach-Zehnder All-Optical Switch," *IEEE Photonics Technology Letters*, vol. 10, no. 11, pp. 1575-1577, 1998.

[71] I.Glesk, R.J.Runser, and P.R.Prurcnal, "New Generation of Devices For All-Optical Communications," *acta physica solvaca*, vol. 51, no. 2, pp. 151-162, Apr.2001.

[72] Patel, N. S., Rauschenbach, K. A., and Hall, K. L., "40-Gb/s demultiplexing using an ultrafast nonlinear interferometer (UNI)," *Photonics Technology Letters, IEEE*, vol. 8, no. 12, pp. 1695-1697, 1996.

[73] P.R.Prurcnal, R.J.Runser, and M.H.Singer, "Optical switching techniques for the next Generation Internet A Competitive Study," *White Paper*, pp. 1-14, 2000.

[74] R.Lenz, "Introduction to All Optical Switching Technologies," 2003, www.2cool4u.ch/wdm_dwdm/intro_allopticalswitching/into_allopticalswitching.pdf

[75] J.Hetch. Many Approaches Taken for All-Optical Switching. Laser Focus World 37[8], 125-160. 2003.
Ref Type: Magazine Article

[76] Kruglick, K. MEMS Crossconnects Demand Precision from Design to Delivery. WDM Solutions [March 2001], 103-106. 2001.
Ref Type: Magazine Article

[77] I.Glesk, R.J.Runser, and P.R.Prurcnal, "New Generation of Devices For All-Optical Communications," *acta physica solvaca*, vol. 51, no. 2, pp. 151-162, Apr.2001.

[78] I.Glesk, R.J.Runser, and P.R.Prurcnal, "New Generation of Devices For All-Optical Communications," *acta physica solvaca*, vol. 51, no. 2, pp. 151-162, Apr.2001.

[79] Mary Ward and Frank Briamonte, "Lucent's New All-Optical Router Uses Bell Labs Microscopic Mirrors," 2003, http://www.bell-labs.com/news/1999/november/10/1.html

[80] Agilent Laboratories, 2003, Agilent Laboratories

[81] Agilent Laboratories, 2003, Agilent Laboratories

[82] R.Lenz, "Introduction to All Optical Switching Technologies," 2003, www.2cool4u.ch/wdm_dwdm/intro_allopticalswitching/into_allopticalswitching.pdf

[83] Bregni, S., Guerra, G., and Pattavina, A., "State of the Art of Optical Switching Technology for All-Optical Networks," WSES Press 2001,

[84] R.Lenz, "Introduction to All Optical Switching Technologies," 2003, www.2cool4u.ch/wdm_dwdm/intro_allopticalswitching/into_allopticalswitching.pdf

[85] J.Hetch. Modulators and Switches are Key to All-Optical Networks. WDM Solutions [June 2001], 101-104. 2001.
Ref Type: Magazine Article

[86] I.Glesk, R.J.Runser, and P.R.Prurcnal, "New Generation of Devices For All-Optical Communications," *acta physica solvaca*, vol. 51, no. 2, pp. 151-162, Apr.2001.

[87] S.Nakamura, Y.Ueno, and K.Tajima, "Ultrafast (200-fs Switching, 1.5-Tb/s Demultiplexing) and High-Repetition (10 GHz) Operations of a Polarization-Discriminating Symmetric Mach-Zehnder All-Optical Switch," *IEEE Photonics Technology Letters*, vol. 10, no. 11, pp. 1575-1577, 1998.

[88] I.Glesk, R.J.Runser, and P.R.Prurcnal, "New Generation of Devices For All-Optical Communications," *acta physica solvaca*, vol. 51, no. 2, pp. 151-162, Apr.2001.

[89] Hall, K. L. and Rauschenbach, K. A., "100 Gb/s Bitwise Logic," *Optics Letters*, vol. 23, no. 16, pp. 1271-1273, 1998.

[90] I.Glesk, R.J.Runser, and P.R.Prurcnal, "New Generation of Devices For All-Optical Communications," *acta physica solvaca*, vol. 51, no. 2, pp. 151-162, Apr.2001.

[91] B.C.Wang, V.Baby, W.Tong, L.Xu, M.Friedman, R.J.Runser, and P.R.Prurcnal, "A Novel Fast Optical Switch Based on Two Cascaded Terahertz Optical Asymmetric Demultiplexers (TOAD)," *Optics Express*, vol. 10, no. 1, pp. 15-23, 2002.

[92] I.Glesk, R.J.Runser, and P.R.Prurcnal, "New Generation of Devices For All-Optical Communications," *acta physica solvaca*, vol. 51, no. 2, pp. 151-162, Apr.2001.

[93] Palmer, J. R. All-Optical Switches and OEO Will Share the Load. WDM Solutions March 2001, 109-112. 2001.
Ref Type: Magazine Article

[94] Pollock, C. R., *Fundamentals of Optoelectronics* Richard D. Irwin, Inc., 2003.

[95] Ramaswami, R. and Sivarajan, K. N., *Optical Networks - A Practical Perspective*, Second ed. Morgan Kaufmann Publishers, 2002.

[96] Agrawal, G. P., *Nonlinear Fiber Optics*, Second ed. Academic Press, 1999.

[97] Cheung, C. Y, "Noise and Crosstalk Analysis of All-Optical Time Division Multiplexers." PhD. Thesis Sheffield Hallam University, 2001.

[98] Hasegawa, A., *Optical Solitons in Fibers*, Second ed. Springer-Verlag, 1989.

[99] Taylor, J. R., *Optical Solitons - Theory and Experiment* Cambridge University Press, 1992.

[100] Suzuhi, K., Kubota, H., Sahara, A., and Nakazawa, M., "40-Gbit/s single-channel optical soliton transmission over 70000 km using in-line synchronous modulation and optical filtering," *Proceedings of Optical Fiber Communication Conference and Exhibit. (Technical Digest)*, OFC '98 San Jose, CA USA 1998, pp.292-294.

[101] Yamada, E., Imai, T., Komukai, T., and Nakazawa, M., "10 Gbit/s soliton transmission over 2900 km using 1.3 μm singlemode fibres and dispersion compensation using chirped fibre Bragg gratings," *Electronics Letters*, vol. 35, no. 9, pp. 728-729, 1999.

[102] Nakazawa, M., Suzuki, K., Yoshida, E., Yamada, E., Kitoh, T., and Kawachi, M., "160 Gbit/s soliton data transmission over 200 km," *Electronics Letters*, vol. 31, no. 7, pp. 565-566, 1995.

[103] Nakazawa, M., Yoshida, E., Yamada, E., Suzuki, K., Kitoh, T., and Kawachi, M., "80 Gbit/s soliton data transmission over 500 km with unequal amplitude solitons for timing clock extraction," *Electronics Letters*, vol. 30, no. 21, pp. 1777-1778, 1994.

[104] Yamada, E., Suzuhi, K., and Nakazawa, M., "10 Gbit/s single-pass soliton transmission over 1000 km," *Electronics Letters*, vol. 27, no. 14, pp. 1289-1291, 1991.

[105] Hirooka, T., Nakada, T., and Hasegawa, A., "Feasibility of densely dispersion managed soliton transmission at 160 Gb/s," *IEEE Photonics Technology Letters*, vol. 12, no. 6, pp. 633-635, 2000.

[106] Mollenauer, L. F., Lichtman, E., Harvey, G. T., Neubelt, M. J., and Nyman, B. M., "Demonstration of error-free soliton transmission over more than 15000 km at 5 Gbit/s, single-channel, and over more than 11000 km at 10 Gbit/s in two-channel WDM," *Electronics Letters*, vol. 28, no. 8, pp. 792-794, 1992.

[107] Mollenauer, L. F., Neubelt, M. J., Haner, M., Lichtman, E., Evangelides, S. G., and Nyman, B. M., "Demonstration of error-free soliton transmission at 2.5 Gbit/s over more than 14000 km," *Electronics Letters*, vol. 27, no. 22, pp. 2055-2056, 1991.

[108] Nakazawa, M., Suzuki, K., Yamada, E., and Kimura, Y., "20 Gbit/s soliton transmission over 200 km using erbium-doped fibre repeaters," *Electronics Letters*, vol. 26, no. 19, pp. 1592-1593, 1990.

[109] Suzuki, K., Nakazawa, M., Yamada, E., and Kimura, Y., "5 Gbit/s, 250 km error-free soliton transmission with Er³⁺ -doped fibre amplifiers and repeaters," *Electronics Letters*, vol. 26, no. 8, pp. 551-553, 1990.

[110] Nakazawa, M., Suzuki, K., and Kubota, H., "Single-channel 80 Gbit/s soliton transmission over 10000 km using in-line synchronous modulation," *Electronics Letters*, vol. 35, no. 2, pp. 162-164, 1999.

[111] Nakazawa, M., Kubota, H., Yamada, E., and Suzuki, K., "Infinite-distance soliton transmission with soliton controls in time and frequency domains," *Electronics Letters*, vol. 28, no. 12, pp. 1099-1100, 1992.

[112] Arnold, J. M., "Soliton pulse-position modulation," *Optoelectronics [see also IEE Proceedings-Optoelectronics], IEE Proceedings J*, vol. 140, no. 6, pp. 359-366, 1993.

[113] Lerner, J., "Solitons Form the Basis for WDM Replacement Technology," 1998, Lightwave

[114] Boardman, A. D., Bertolotti, M., and Twardowski, T., *Nonlinear Waves in Solid State Physics* Plenum Press, 1990.

[115] Someda, C. G. and Stegeman, G., *Anisotropic and Nonlinear Optical Waveguides* 2003.

[116] Liu, A. M., Wu, C. Q., Lim, M. S., Gong, Y. D., and Shum, P., "Optical buffer configuration based on a 3 x 3 collinear fibre coupler," *Electronics Letters*, vol. 40, no. 16, pp. 1017-1018, 2004.

[117] Seung-Woo Seo, Bergman, K., and Prucnal, P. R., "Transparent optical networks with time-division multiplexing," *Selected Areas in Communications, IEEE Journal on*, vol. 14, no. 5, pp. 1039-1051, 1996.

[118] Glesk, I., Kang, K. J., and Prucnal, P. R., "Demonstration of ultrafast all-optical packet routing," *Electronics Letters*, vol. 33, no. 9, pp. 794-795, 1997.

[119] Deng, K.-L., Runser, R. J., Toliver, P., Coldwell, C., Zhou, D., Glesk, I., and Prucnal, P. R., "Demonstration of highly scalable 100 Gbit/s OTDM computer interconnect with rapid interchannel switching capability," *Electronics Letters*, vol. 34, no. 25, pp. 2418-2419, 1998.

[120] Yamamoto, T., "640-Gbit/s optical TDM transmission over 92 km through a dispersion-managed fiber consisting of single-mode fiber and “reverse dispersion fiber”" *Photonics Technology Letters, IEEE*, vol. 12, no. 3, pp. 353-355, 2000.

[121] Prucnal, P. R., "Optically processed self-routing, synchronization, and contention resolution for 1-D and 2-D photonic switching architectures," *Quantum Electronics, IEEE Journal of*, vol. 29, no. 2, pp. 600-612, 1993.

[122] Hunter, D. K., Chia, M. C., and Andonovic, I., "Buffering in optical packet switches," *Lightwave Technology, Journal of*, vol. 16, no. 12, pp. 2081-2094, 1998.

[123] Shun, Y., "Advances in photonic packet switching: an overview," *Communications Magazine, IEEE*, vol. 38, no. 2, pp. 84-94, 2000.

[124] Desurvire, E., *Erbium-Doped Fibre Amplifiers* Wiley, 1994.

[125] Senior, J. M., *Optical Fiber Communications* Prentice Hall, 1992.

[126] Stremler, F. G., *Introduction to Communication Systems*, 3rd ed. Addison-Wesley, 1990.

[127] Sheung-Han, C. and Hisashi, K., "Buffer Architectures and Routing Algorithms in the Performance if Shufflenet," Singapore 1993, pp.34-38.

[128] Park, H., Burmeister, E., Björlin, S., and Bowers, J., "40-Gb/s Optical Buffer Design and Simulation," University of California at Santa Barbara 2004, pp.TUC2.

[129] Gordon, J. P. and Haus, H. A., "Random walk of coherently amplified solitons in optical fiber transmission," *Optics Letters*, vol. 11, no. 10, pp. 665-667, 1986.

[130] Ferreira, M. F. S. and Latas, S. C. V., "Timing jitter in soliton transmission with up- and down-sliding-frequency guiding filters," *Lightwave Technology, Journal of*, vol. 19, no. 3, pp. 332-335, 2001.

[131] Ferreira, M. F. S. and Latas, S. C. V., "Timing jitter in soliton transmission with up- and down-sliding-frequency guiding filters," *Lightwave Technology, Journal of*, vol. 19, no. 3, pp. 332-335, 2001.

[132] Harboe, P. B. and Souza, J. R., "Soliton control with fixed- and sliding-frequency filters: a feasibility study," *Proceedings of the International*

Microwave and Optoelectronics Conference, IMOC '01 Brazil 2001, pp.503-507.

[133] Smith, N. J., Doran, N. J., and Forysiak, F., "Gordon-Haus jitter suppression using an intra-span phase modulator and post transmission dispersion compensator," *Photonics Technology Letters, IEEE*, vol. 8, no. 3, pp. 455-457, 1996.

[134] Kutz, J. N. and Wai, P. K. A., "Gordon-Haus timing jitter reduction in dispersion-managed soliton communications," *Photonics Technology Letters, IEEE*, vol. 10, no. 5, pp. 702-704, 1998.

[135] Schwartz, M., *Information Transmission, Modulation, and Noise* McGraw-Hill, 1970.

[136] Mauro, J. C., "Timing jitter in Soliton Communication Systems," 2004, http://homepage.mac.com/maurojc/papers/pdf/jitter.pdf

[137] Islam, M. N., "Raman Amplifiers for Telecommunications," *IEEE JOURNAL OF SELECTED TOPICS IN QUANTUM ELECTRONICS*, vol. 8, no. 3, pp. 548-559, 2002.

[138] Marcuse, D., "An alternative derivation of the Gordon-Haus effect," *Lightwave Technology, Journal of*, vol. 10, no. 2, pp. 273-278, 1992.

[139] VPISystems, *VPItransmissionMaker VPIcomponentMaker - Photonic Modules Reference Manual (VOL 2)* 2001.

[140] Steele, R. C., Walker, G. R., and Walker, N. G., "Sensitivity of optically preamplified receivers with optical filtering," *Photonics Technology Letters, IEEE*, vol. 3, no. 6, pp. 545-547, 1991.

[141] VPISystems, *VPItransmissionMaker VPIcomponentMaker - Photonic Modules Reference Manual (VOL1)* VPIsystems, 2001.

[142] Smith, D. W., *Optical Network Technology*, First ed. Chapman & Hall, 1995.

[143] Moores, J. D., Hall, K. L., LePage, S. M., Rauschenbach, K. A., Wong, W. S., Haus, H. A., and Ippen, E. P., "20-GHz optical storage loop/laser using amplitude modulation, filtering, and artificial fast saturable absorption," *Photonics Technology Letters, IEEE*, vol. 7, no. 9, pp. 1096-1098, 1995.

[144] Harvey, H. J., "Concepts in soliton control," *Optical Solitons: Principles and Applications, IEE Colloquium on*, pp. 6-1-6/6, 1994.

[145] Friberg, S. R. and Machida, S., "Soliton Excess-noise Reduction By >18 db Using Soliton Spectral Filtering," 1997, pp.63-64.

[146] Nakazawa, M., Yamada, E., Kubota, H., and Suzuki, K., "10 Gbit/s soliton data transmission over one million kilometres," *Electronics Letters*, vol. 27, no. 14, pp. 1270-1272, 1991.

[147] Friberg, S. R. and Machida, S. Soliton spectral filtering for suppression of intensity noise: demonstration of >23 dB reduction of 1/f noise. 1997.
Ref Type: Unpublished Work

[148] *VPItransmissionMaker VPIcomponentMaker - Photonic Modules Reference Maual (VOL 2)* 2001.

[149] O'Mahony, M. J., "Semiconductor laser optical amplifiers for use in future fiber systems," *Lightwave Technology, Journal of*, vol. 6, no. 4, pp. 531-544, 1988.

[150] Agrawal, G. P. and Olsson, N. A., "Self-phase modulation and spectral broadening of optical pulses in semiconductor laser amplifiers," *Quantum Electronics, IEEE Journal of*, vol. 25, no. 11, pp. 2297-2306, 1989.

[151] Ruiz-Moreno, S. and Guitart, J., "Practical method for modelling the nonlinear behaviour of a travelling wave semiconductor optical amplifier," *Optoelectronics [see also IEE Proceedings-Optoelectronics], IEE Proceedings J*, vol. 140, no. 1, pp. 39-43, 1993.

[152] Gillner, L., "Comparative study of some travelling-wave semiconductor laser amplifier models," *Optoelectronics [see also IEE Proceedings-Optoelectronics], IEE Proceedings J*, vol. 139, no. 5, pp. 339-347, 1992.

[153] Lowery, A. J., "New inline wideband dynamic semiconductor laser amplifier model," *Optoelectronics [see also IEE Proceedings-Optoelectronics], IEE Proceedings J*, vol. 135, no. 3, pp. 242-250, 1988.

[154] Agrawal, G. P. and Olsson, N. A., "Amplification and compression of weak picosecond optical pulses by using semiconductor-laser amplifier," *Optics Letters*, vol. 14, no. 10, pp. 500-502, 2003.

[155] Gillner, L., "Modulation properties of a near travelling-wave semiconductor laser amplifier," *Optoelectronics [see also IEE Proceedings-Optoelectronics], IEE Proceedings J*, vol. 139, no. 5, pp. 331-338, 1992.

[156] K.Tajima, S.Nakamura, Y.Ueno, J.Sasaki, T.Sugimoto, T.Kato, M.Itoh, H.Hatakeyama, T.Tamanuki, and T.Sasaki, "Hybrid Integrated Symmetric Mach-Zehnder All-Optical Switch with Untrafast, High Extinction Ratio," *Electronic Letters*, vol. 35, no. 23, pp. 2030-2031, 1999.

[157] S.Nakamura, Y.Ueno, J.Sasaki, T.Sugimoto, T.Kato, T.Shimoda, M.Itoh, H.Hatakeyama, T.Tamanuki, and T.Sasaki, "168 Gbps Error-Free Demultiplexing with Hybrid-Integrated Symmetric Mach-Zehnder All-Optical Switch," *Optical Fiber Communication Conference*, Baltimore, MD , USA 2000, pp.81-83.

[158] S.Nakamura, Y.Ueno, and K.Tajima, "Ultrafast (200-fs Switching, 1.5-Tb/s Demultiplexing) and High-Repetition (10 GHz) Operations of a Polarization-Discriminating Symmetric Mach-Zehnder All-Optical Switch," *IEEE Photonics Technology Letters*, vol. 10, no. 11, pp. 1575-1577, 1998.

[159] Eiselt, M., Pieper, W., and Weber, H. G., "SLAOLM: Semiconductor Laser Amplifier in a loop mirrir," *Lightwave Technology, Journal of*, vol. 13, no. 10, pp. 2099-2112, Oct.1995.

[160] Laevens, K. and Bruneel, H., "Analysis of a single-wavelength optical buffer," 2003, pp.2262-2267.

[161] Laevens, K., Van Houdt, B., Blondia, C., and Bruneel, H., "Sustainable load of fibre delay line buffers," *Electronics Letters*, vol. 40, no. 2, pp. 137-138, 2004.

[162] Chang-Hasnain, C. J., Pei-cheng, K., Jungho, K., and Shun-lien, C., "Variable optical buffer using slow light in semiconductor nanostructures," *Proceedings of the IEEE*, vol. 91, no. 11, pp. 1884-1897, 2003.

Appendix A

An all-optical TOAD-Based Router

A.1 Introduction

This appendix is intended to present the operation of a TOAD based all-optical router. Figure A.1 shows a block diagram of an OTDM transmission system. It consists of an OTDM packet generator, additive white Gaussian noise (AWGN) channel, optical router, matched filter and a detector. This proposed system was modelled using MATLAB and it was assumed that the router architecture has as its input an OTDM packet containing header and payload information. The model simulates extraction of header information, from the data stream using a TOAD, which is subsequently used to make a routing decision. The payload information is routed through a second TOAD according to the information contained in the header. A bit period of 4 ps corresponding to a 0.25 Tb/s bandwidth optical network is assumed.

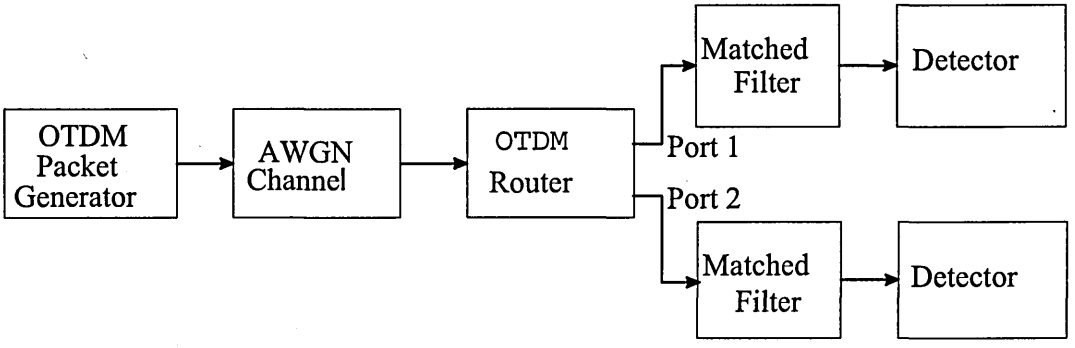

Figure A.1 Block diagram of OTDM system

Figure A.2 shows the format of two consecutive packets at the output from the OTDM packet generator. Framing bits indicate the inter-packet boundaries thereby providing a synchronisation mechanism. The address bits indicate the destination port to which the payload information is routed. A value of '0' ('1') results in the payload information being routed to port 1 (port 2) of the OTDM router.

Frame Bit	Address 0/1	Payload Information 1101...01		Frame Bit	Address 0/1	Payload Information 0110...10

Figure A.2 Format of OTDM packet

A.2 Analysis of Switching Operation

To demonstrate all-optical address recognition and single bit self-routing, a single node of all optical time division multiplexed router is constructed from two TOADs. As shown in Figure A.3, the switching node consists of an all-optically controlled routing switch (TOAD2 with $\Delta x = T_p c/2$, where $T_p = 20$ ps is the width of switching window), an ultrafast controller (TOAD1 with $\Delta x = \tau c/2$, where τ is the width of the window equals to the duration of the address bit) and a buffer. The ultrafast controller all-optically sets the states of the routing switch (TOAD2) in a switched or un-switched state, and the optical buffer matches the delays of the input packet to the processing delay of the routing controller [1]. When an OTDM data signal enters the node, the clock, which is an orthogonal polarisation signal, is separated from the optical packet using a polarisation beam splitter (PS) and then used as the control signal of TOAD1. A portion of the packet is split off and sent to TOAD1 before entering the buffer. The TOAD1 reads the packet destination address bit and uses it as the optical routing control

for the routing switch (TOAD2). The optical packet, in which the constituent bit duration is 4 ps (i.e. 250Gbit/s), is composed of a leading clock pulse, a 1-bit header, and a 3-bit payload. In a single bit routing scheme, the packet with address bit of value "0" are routed to output port 1, while packet with an address bit of value "1" are routed to output port 2. Thus photonic packets are self-routed through an all optical ultrafast switch without the need for optoelectronic conversion.

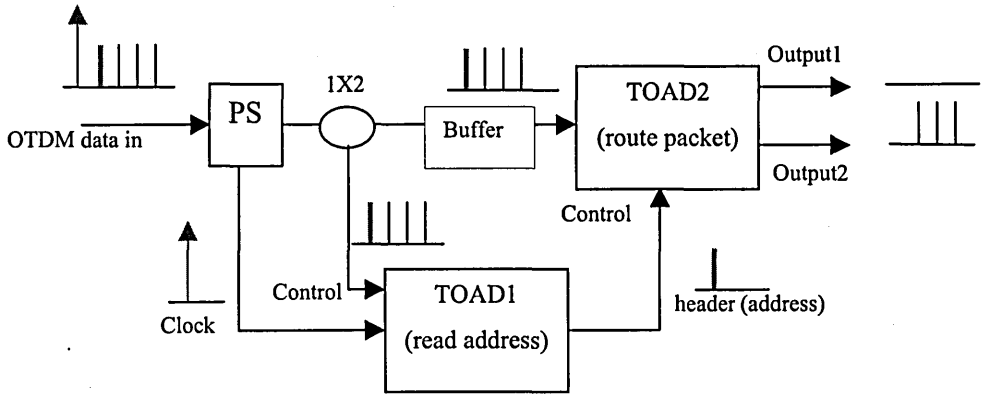

Figure A.3 Node of all optical time division multiplexed router

A.3 Simulation of the OTDM System

Using the model described in section A.1, the output of the OTDM system was simulated with the parameters listed in Table A.1.

Figure A.4 shows three packets of the OTDM waveform at the output of the OTDM packet generator. Packet 1 to 3 formats are 1001, 0010 and 1011, respectively. Observe that the packet consists of a frame signal, distinguishable by its higher amplitude, a bit address and payload information, which is in accordance to the format illustrated in Figure A.2. Thus according to the routing convention established in section A.1, packets one and three should be routed to the port 2 whereas packet 2 should be routed to the port 1. Successful routing is highlighted in Figure A.5, which shows the waveform at

output port 2 of the OTDM router. Note that the change in the amplitude levels is due to the non-symmetric profile of the TOAD switching window. The crosstalk observed in Packet 2 is also due to the switching window profile. For more on this see [2].

Table A.1 TOAD router simulation parameters

Parameters	Values
Control pulse width FWHM	2 ps
Control pulse wavelength	1500 nm
Control pulse power	0.8 pJ
Data signal width FWHM	2 ps
Data signal wavelength	1550 nm
SOA length	300 um
Number of SOA	200
SOA active area	$0.2 \times 10^{-12} m^2$
SOA carrier lifetime	300 ps
SOA transparent carrier density	$10^{24} m^{-3}$
SOA confinement factor	0.3
SOA position Δx	2 ps
Number of Packets	5000
Number of framing bits per packet	1
Number of address bits per packet	1
Number of payload bits per packet	3
Bit period	4 ps
Packet Period (T_p)	20 ps

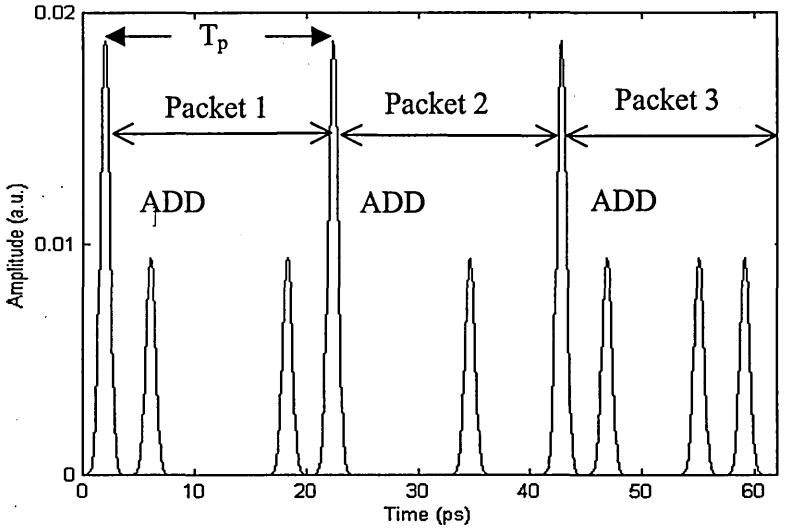

Figure A.4 Three packets of a transmitted OTDM waveform

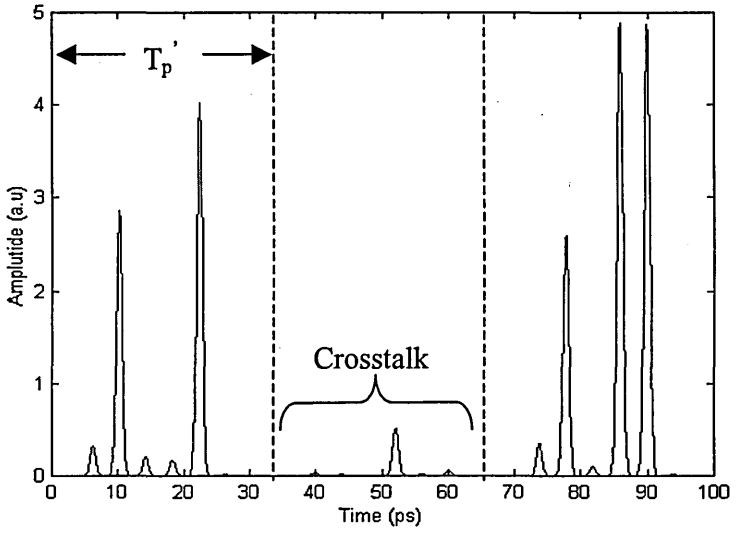

Figure A.5 OTDM Signal at output of Router

REFERENCES

1. R. Gao, Z. Ghassemlooy, G. Swift and P. Ball "Simulation of all optical time division multiplexed router", West Electronics 2001 Proceedings, Jan. 2001.

2. J. P. Sokolof, I. Glest, P.R.Prucnal, and R.K. Boncek, "Performance of a 50Gbit/s optical time domain multiplexed system using a terahertz optical asymmetric demultiplexer", IEEE Photonics Technology Letters, 6(1), pp. 123-126, Jan. 1994

Appendix B

This appendix presents the details of the calculations covered in Chapter 4. In particular, section B1 shows the calculations for the elimination of the flux densities from Maxwell's curl equations. Section B2 presents the solution for the wave equation assuming that the propagation medium is linear and isotropic. Finally, the linearity assumption is removed and its affect of the propagation constant is presented in section B3.

B.1 Flux Density Elimination from Maxwell's Curl Equations

Recall from Maxwell's curl equation (4.3) that

$$\nabla \times \mathbf{E} = -\frac{\partial}{\partial t}\mathbf{B} \tag{B.1}$$

Hence the curl of (B.1) may be given by:

$$\nabla \times \nabla \times \mathbf{E} = \nabla \times \left(-\frac{\partial}{\partial t}\mathbf{B} \right) \tag{B.2}$$

Substituting for **B** from (4.7) into (B.2) yields

$$\nabla \times \nabla \times \mathbf{E} = \nabla \times \left[-\frac{\partial}{\partial t}(\mu_0 \mathbf{H} + \mathbf{M}) \right] \tag{B.3}$$

With **M** = 0 for optical fibre (B.3) simplifies to

$$\nabla \times \nabla \times \mathbf{E} = -\mu_0 \frac{\partial}{\partial t}(\nabla \times \mathbf{H}) \tag{B.4}$$

Substituting for $\nabla \times \mathbf{H}$ from (4.4) into (B.4) yields:

$$\nabla \times \nabla \times \mathbf{E} = -\mu_0 \frac{\partial}{\partial t}\left(\mathbf{J} + \frac{\partial}{\partial t}\mathbf{D}\right)$$

$$= -\mu_0 \frac{\partial}{\partial t}\left(\sigma \mathbf{E} + \frac{\partial}{\partial t}\mathbf{D}\right) \tag{B.5}$$

As $\sigma \approx 0$ for optical fibre (B.5) may be reduced to:

$$\nabla \times \nabla \times \mathbf{E} = -\mu_0 \frac{\partial^2}{\partial t^2}\mathbf{D} \tag{B.6}$$

Finally, the electric flux density may be eliminated from (B.6) by substituting for **D** using the identity in (4.6) to yield:

$$\nabla \times \nabla \times \mathbf{E} = -\varepsilon_0 \mu_0 \frac{\partial^2}{\partial t^2}\mathbf{E} - \mu_0 \frac{\partial^2}{\partial t^2}\mathbf{P} \tag{B.7}$$

B.2 The Wave Equation

To solve for the wave equation from (B.7), first note the Fourier transforms of **E** and **P** are given as:

$$\mathbf{E}(\mathbf{r}, t) = \frac{1}{2\pi}\int_{-\infty}^{\infty} \tilde{\mathbf{E}}(\mathbf{r}, \omega)\exp(-i\omega t)d\omega \tag{B.8}$$

$$\mathbf{P}(\mathbf{r}, t) = \frac{1}{2\pi}\int_{-\infty}^{\infty} \tilde{\mathbf{P}}(\mathbf{r}, \omega)\exp(-i\omega t)d\omega \tag{B.9}$$

The partial derivatives of (B.8) and (B.9) with respect to t yields their Fourier transforms. Consequently, the Fourier transform of (B.7) gives:

$$\nabla \times \nabla \times \tilde{\mathbf{E}} = \varepsilon_0 \mu_0 \omega^2 \tilde{\mathbf{E}} + \mu_0 \omega^2 \tilde{\mathbf{P}} \tag{B.10}$$

Assuming that the non-linear effects are negligible, substitute the linear portion of (4.9) into (B.10) to give:

$$\nabla \times \nabla \times \tilde{\mathbf{E}} = \varepsilon_0 \mu_0 \omega^2 \tilde{\mathbf{E}} + \mu_0 \omega^2 \varepsilon_0 \tilde{\chi} \tilde{\mathbf{E}} \tag{B.11a}$$

$$= \varepsilon_0 \mu_0 \omega^2 \tilde{\mathbf{E}} (1 + \tilde{\chi}) \tag{B.11b}$$

$$= \frac{\omega^2 n^2}{c^2} \tilde{\mathbf{E}} \tag{B.11c}$$

where $c = 1/\sqrt{\mu_0 \varepsilon_0}$ and $n = \sqrt{1 + \tilde{\chi}}$. Note that the assumption of a negligible succeptibility in (B.11a) leads to the result given in (4.11).

Using the curl identity given in (4.13) then the wave equation (B.11c) may be expressed as:

$$\frac{\omega^2 n^2}{c^2} \tilde{\mathbf{E}} = \nabla \left(\nabla \cdot \tilde{\mathbf{E}} \right) - \nabla^2 \tilde{\mathbf{E}}$$

$$\nabla^2 \tilde{\mathbf{E}} + \frac{\omega^2 n^2}{c^2} \tilde{\mathbf{E}} = 0 \tag{B.12}$$

Equation (B.12) describes the propagation of waves in a linear, isotropic medium.

B.3 Non-linear Effect on Propagation Constant

Using the curl identity given in (4.13), (B.10) may be expressed in the form:

$$\nabla^2\widetilde{\mathbf{E}} + \varepsilon_0\mu_0\omega^2\widetilde{\mathbf{E}} + \mu_0\omega^2\widetilde{\mathbf{P}} = 0 \tag{B.13}$$

Taking both the linear and non-linear dielectric polarisations of (B.13) into consideration (i.e. $\widetilde{\mathbf{P}} = \widetilde{\mathbf{P}}_L + \widetilde{\mathbf{P}}_{NL}$) gives:

$$\nabla^2\widetilde{\mathbf{E}} + \varepsilon_0\mu_0\omega^2\widetilde{\mathbf{E}} + \mu_0\omega^2\left(\widetilde{\mathbf{P}}_L + \widetilde{\mathbf{P}}_{NL}\right) = 0 \tag{B.13}$$

Substituting for $\widetilde{\mathbf{P}}_L$ and $\widetilde{\mathbf{P}}_{NL}$ from (4.9) into (B.13) gives:

$$\nabla^2\widetilde{\mathbf{E}} + \varepsilon_0\mu_0\omega^2\widetilde{\mathbf{E}} + \varepsilon_0\mu_0\omega^2\widetilde{\chi}^{(1)}\widetilde{\mathbf{E}} + \varepsilon_0\mu_0\omega^2\widetilde{\chi}^{(3)}\widetilde{\mathbf{E}}^3 = 0 \tag{B.14}$$

Assuming a monochromatic plane wave with an electric field given by $\mathbf{E}(z,t) = E\cos(\omega_0 t - \beta_0 z)$ then the Fourier transform of (B.14) may be expanded to yield:

$$\begin{aligned}&\frac{\partial^2}{\partial z^2}\left[E\cos(\omega_0 t - \beta_0 z)\right] + \varepsilon_0\mu_0\omega^2 E\cos(\omega_0 t - \beta_0 z) + \varepsilon_0\mu_0\omega^2\chi^{(1)}E\cos(\omega_0 t - \beta_0 z)\\ &+ \varepsilon_0\mu_0\omega^2\chi^{(3)}\left[E\cos(\omega_0 t - \beta_0 z)\right]^3 = 0\end{aligned} \tag{B.15}$$

Calculating the second order partial differential and expanding the last term in (B.15) gives:

$$-\beta_0^2 E\cos(\omega_0 t-\beta_0 z)+\varepsilon_0\mu_0\omega^2 E\cos(\omega_0 t-\beta_0 z)+\varepsilon_0\mu_0\omega^2\chi^{(1)}E\cos(\omega_0 t-\beta_0 z)$$
$$+\varepsilon_0\mu_0\omega^2\chi^{(3)}E^3\left[\frac{3}{4}\cos(\omega_0 t-\beta_0 z)+\frac{1}{4}\cos(3\omega_0 t-\beta_0 z)\right]=0 \qquad \text{(B.16)}$$

Neglecting the component at $3\omega_0$ in (B.16) and simplifying yields:

$$-\beta_0^2+\varepsilon_0\mu_0\omega^2+\varepsilon_0\mu_0\omega^2\chi^{(1)}+\frac{3}{4}\varepsilon_0\mu_0\omega^2\chi^{(3)}E^2=0 \qquad \text{(B.17)}$$

Finally, (B.17) may be solved for β_0 as shown in (B.18)

$$\beta_0^2=\varepsilon_0\mu_0\omega^2\left(1+\chi^{(1)}+\frac{3}{4}\chi^{(3)}E^2\right)$$
$$=\frac{\omega_0^2}{c^2}\left(1+\chi^{(1)}+\frac{3}{4}\chi^{(3)}E^2\right)$$
$$=\frac{\omega_o n}{c}\sqrt{\left(1+\frac{3}{4n^2}\chi^{(3)}E^2\right)} \qquad \text{(B.18)}$$

As $\chi^{(3)}$ is very small for optical fibre (B.18) may be approximated to yield [1]:

$$\beta_0^2=\frac{\omega_o}{c}\left(n+\frac{3}{8n}\chi^{(3)}E^2\right) \qquad \text{(B.19)}$$

REFERENCES:

1. Ramaswami R, Sivarajan KN: Optical Networks - A Practical Perspective, Morgan Kaufmann Publishers, 2002.

Appendix C

C.1 Introduction

The purpose of this appendix is to mathematically validate the BER simulation results for the passive RFLB presented in Chapter 5.

As the soliton pulses are launched with a fixed peak power and pulse width, it is valid to assume that the launched energy ($\sqrt{E_0}$) is constant. Consequently, transmitted logical '1' (/'0') bits will have energy $\sqrt{E_0}$ (/0). The AWGN channel corrupts the data signal causing the received signal energies to be $\sqrt{E_0} + n(t)$ and $n(t)$ for logical '1' and '0', respectively. To distinguish between the two logical data signals a decision threshold mechanism is employed at the receiver. Received energy values greater than a preset threshold value T_H are interpreted as '1' bits, and the reverse holds true for '0' bits. Assuming that the transmissions of '1' and '0' bits are equiprobable, Figure C.1 shows a plot of the conditional density functions with mean values of $\sqrt{E_0}$ and 0, respectively. Assuming that a 1-bit is transmitted, then an error is detected if the received energy value (x) falls below the threshold value (i.e. $x < \sqrt{E_0}/2$). Similarly, assuming that a 0-bit is transmitted, then an error is detected if the received energy value lies above below this threshold value.

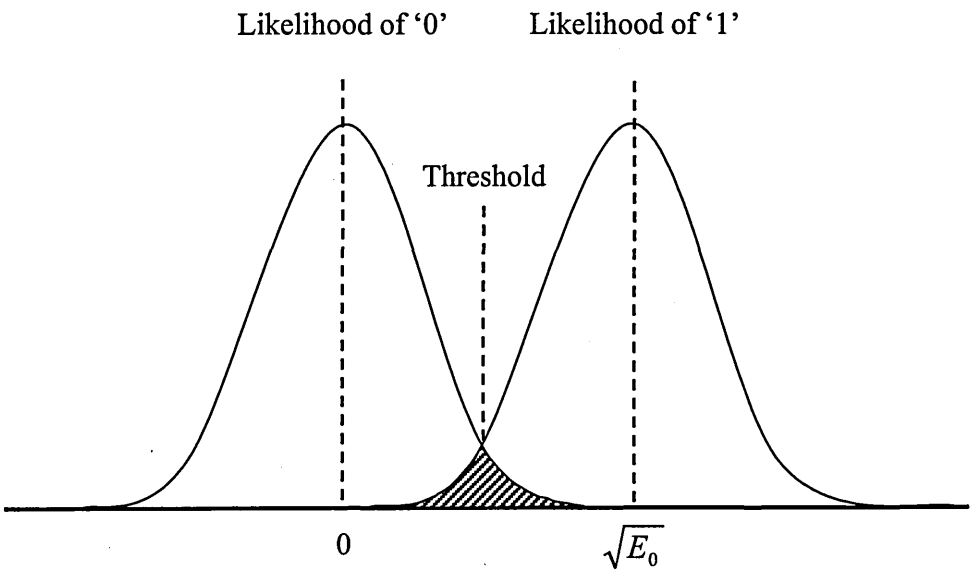

Figure C.1 Conditional probability density functions: $f(x|0), f(x|1)$

C.2 Proof of BER Expression for the Passive RFLB

The likelihood that x is received given that a 1-bit was transmitted is given by:

$$f(x \mid 1) = \frac{1}{\sigma\sqrt{2\pi}} \exp\left[-\frac{\left(x - \sqrt{E_0}\right)^2}{2\sigma^2} \right], \tag{C.1}$$

where the noise variance σ^2 is equivalent to $N_0/2$. Note that N_0 is the noise spectral density.

Similarly, likelihood that x is received given that a 0-bit was transmitted is given by:

$$f(x \mid 0) = \frac{1}{\sigma\sqrt{2\pi}} \exp\left[-\frac{x^2}{2\sigma^2} \right], \tag{C.2}$$

Figure C.1 highlights that the conditional probability of the receiver deciding in favour of a 1-bit given that a 0-bit was transmitted $P(1|0)$, is equivalent to the (shaded) area under the $f(x|0)$ curve that lies above the threshold. Consequently,

$$P(1|0) = P(x > T_h \mid 0),$$

$$P(1|0) = \frac{1}{\sigma\sqrt{2\pi}} \int_{T_h}^{\infty} \exp\left[-\frac{x^2}{2\sigma^2}\right] dx \qquad \text{(C.3)}$$

To solve equation C.3 let $u = \frac{x}{\sigma}$, thus $dx = \sigma\, du$.

Changing the variable of integration in C.3 from x to u gives:

$$P(1|0) = \frac{1}{\sqrt{2\pi}} \int_{T_h/\sigma}^{\infty} \exp\left[-\frac{u^2}{2}\right] du$$

$$= Q\left(\frac{T_h}{\sigma}\right) \qquad \text{(C.4)}$$

Substituting for T_h and σ in (C.4) yields:

$$P(1|0) = Q\left(\sqrt{\frac{E_0}{2N_0}}\right) \qquad \text{(C.5)}$$

By employing the same technique above it is easy to show that the probability of an bit error $P_e = P(1|0) = P(0|1)$.

Note that (C.5) describes the probability of an error for the unbuffered case. Recall from Chapter 5 (Section 3), that the inherent fibre loss α causes the energy of the incident pulses to decay exponentially as a function of the number of loop traversals l_n. Incorporating this loss into equation C.5 forms the final expression given in (C.6).

$$P_e = Q\left(\sqrt{\frac{E_0 \cdot \exp(-\alpha l_n)}{2N_0}}\right) \tag{C.6}$$

Equation C.6 now describes the probability of a bit error of a buffered pulse. Observe that for l_n=0 the equations defaults back to OOK.

Appendix D

D.1 Introduction

In this appendix, the development of the mathematical expression describing the gain characteristic of the SOA for ultra-short pulses, given in Chapter 7, is presented. Moreover, the mathematical expression for the momentary gain during the recovery stage of the device is also presented. The material presented here is based the work done by Eiselt [1]. The main objective is to present the mathematical intricacies that are absent in that work.

D.2 SOA Gain Depletion Characteristic Equation

In chapter 6, it was highlighted that the carrier density of the SOA played a critical role in determining the gain of the device. Moreover, the carrier density is time dependent and may be expressed using the rate equation given in (7.5). To highlight this time dependency and the fact that the carrier density is not the same at each spatial position within the device (7.5) may be rewritten to form:

$$\frac{dN(z,t)}{dt} = \frac{I_B}{qV} - \frac{N(z,t)}{\tau_c} - \frac{P(z,t)}{hfA}\Gamma \cdot g \cdot \left[N(z,t) - N_{tr}\right] \tag{D.1}$$

where z and A represent the spatial position within the SOA and the cross-sectional area of the SOA, respectively.

The power within the device at any given spatial location $P(z,t)$, is the product of the incident power and the total gain $G(N, z)$ experienced by the optical wave at z (7.3) and may be expressed as:

$$P(z,t) = P_{in}(t)\cdot\left(\exp\left[\Gamma\cdot g\cdot N(z,t) - N_{tr}\right] - \alpha_{AMP}\right), \tag{D.2}$$

where $P_{in}(t) = P(0,t)$. Hence, the differential power may be expressed as:

$$\frac{dP(z,t)}{dz} = P(z,t)\cdot\left(\Gamma\cdot g\cdot\left[N(z,t) - N_{tr}\right] - \alpha_{AMP}\right), \tag{D.3}$$

and the gain at the output of the device G_0 as:

$$G_0 = \frac{P(L,t)}{P(0,t)} = \exp\left(\Gamma\cdot g\cdot\left[N(z,t) - N_{tr}\right]\cdot L - \alpha_{AMP}\cdot L\right), \tag{D.4}$$

where L is the length of the SOA.

In assuming that the device saturation is caused by an incident optical pulse with high intensity and short duration, only the third term in (D.1) which describes the decrease in the carrier density due to stimulated emission is considered. Consequently, the change of carrier density over the length of the device $\frac{dN_{tot}}{dt}$ may then be expressed as:

$$\begin{aligned}\frac{dN_{tot}}{dt} = \int_0^L N(z,t)dz &= -\frac{1}{hfA}\int_0^L P(z,t)\cdot\Gamma\cdot g\cdot\left[N(z,t) - N_{tr}\right]\cdot L\,dz \\ &= -\frac{1}{hfA}\int_0^L P(z,t)\cdot\left[\frac{\ln(G_0)}{L} + \alpha_{amp}\right]dz \\ &= -\frac{1}{hfA}\left(\frac{\ln(G_0)}{L} + \alpha_{amp}\right)\cdot\int_0^L P(z,t)dz\end{aligned} \tag{D.5}$$

Using (D.2) the integral in (D.5) is determined as follows:

$$\int_0^L P(z,t)\,dz = \int_0^L P_{in}\cdot\left(\exp\left[\Gamma\cdot g\cdot\left(N(z,t)-N_{tr}\right)\right]-\alpha_{AMP}\right)dz$$

$$=\frac{P_{in}}{\exp\left[\Gamma\cdot g\cdot\left(N(z,t)-N_{tr}\right)\right]-\alpha_{AMP}}\cdot\left[\exp\left(\left[\Gamma\cdot g\cdot\left(N(z,t)-N_{tr}\right)\right]\cdot z\right)-\alpha_{AMP}\cdot z\right]_0^L$$

$$=\frac{P_{in}\cdot L}{\ln(G_0)}\cdot\left[\left(\exp\left(\left[\Gamma\cdot g\cdot\left(N(z,t)-N_{tr}\right)\right]\cdot L\right)-\alpha_{AMP}\cdot L\right)-1\right]$$

$$=\frac{L}{\ln(G_0)}\cdot\left[P_{out}(t)-P_{in}(t)\right] \qquad \text{(D.6)}$$

where $P_{out}(t) = P(z,t)$ at $z = L$.

Substituting (D.6) into (D.5) yields:

$$\frac{dN_{tot}}{dt}=-\frac{1}{hfA}\left(\frac{\ln(G_0)}{L}+\alpha_{amp}\right)\cdot\left(\frac{L}{\ln(G_0)}\cdot\left[P_{out}(t)-P_{in}(t)\right]\right)$$

$$=-\frac{1}{hfA}\left(1+\frac{\alpha_{amp}\cdot L}{\ln(G_0)}\right)\cdot\left[P_{out}(t)-P_{in}(t)\right]$$

$$=-\frac{1}{hfA}\left(1+\frac{\alpha_{amp}\cdot L}{\ln(G_0)}\right)\cdot P_{in}(t)\cdot\left[G(t)-1\right] \qquad \text{(D.7)}$$

To solve (D.7) for G_0 first, rearrange the equation and then integrate thereby eliminating references to the carrier density. Rearranging (D.7) yields:

$$\frac{1}{\left[G(t)-1\right]}dN_{tot}=-\frac{1}{hfA}\left(1+\frac{\alpha_{amp}\cdot L}{\ln(G_0)}\right)\cdot P_{in}(t)\,dt\,. \qquad \text{(D.8)}$$

Integrating both sides of (D.8) with respect to t results in:

$$\int_0^{N_{tot}} \frac{1}{[G(t)-1]} dN_{tot}(t) = -\frac{1}{hfA}\left(1+\frac{\alpha_{amp}\cdot L}{\ln(G_0)}\right)\cdot \int_0^t P_{in}(t)dt\,. \tag{D.9}$$

Taking the LHS of (D.9) yields:

$$\int_0^{N_{tot}} \frac{1}{[G(t)-1]} dN_{tot}(t) = \int_0^{N_{tot}} \frac{1}{(\exp[\Gamma\cdot g\cdot N_{tot}(t)]-\alpha_{AMP}\cdot L)-1} dN_{tot}(t).$$

$$= \frac{1}{\Gamma\cdot g}\ln\left[\frac{(\exp[\Gamma\cdot g\cdot N_{tot}(t)]-\alpha_{AMP}\cdot L)-1}{(\exp[\Gamma\cdot g\cdot N_{tot}(t)]-\alpha_{AMP}\cdot L)}\right]_0^{N_{tot}}$$

$$= \frac{1}{\Gamma\cdot g}\cdot\ln\left[\frac{G(t)-1}{G(t)}\right]_0^{N_{tot}}$$

$$= \frac{1}{\Gamma\cdot G}\cdot\ln\left[\frac{G(t)-1}{G(t)}\right]-\ln\left[\frac{G_0-1}{G_0}\right]$$

$$= \frac{1}{\Gamma\cdot g}\cdot\ln\left(\frac{1-\frac{1}{G(t)}}{1-\frac{1}{G_0}}\right) \tag{D.10}$$

In examining the RHS of (D.9), first define the energy of the incident pulse by [2]

$$E_{in}(t) = \int_0^t P_{in}(t)dt\,, \tag{D.11}$$

and the saturation energy by:

$$E_{sat} = -\frac{hfA}{\Gamma\cdot g\cdot\left(1+\frac{\alpha_{amp}\cdot L}{\ln(G_0)}\right)}. \tag{D.12}$$

Thus the final expression for the RHS becomes:

$$-\frac{1}{hfA}\left(1+\frac{\alpha_{amp}\cdot L}{\ln(G_0)}\right)\cdot\int_0^t P_{in}(t)dt=-\frac{1}{\Gamma\cdot g\cdot E_{sat}}E_{in}(t). \tag{D.13}$$

Substituting equations (D.10) through (D.13) into (D.9) gives:

$$\ln\left(\frac{1-\frac{1}{G(t)}}{1-\frac{1}{G_0}}\right)=-\frac{1}{E_{sat}}E_{in}(t)$$

$$\frac{1-\frac{1}{G(t)}}{1-\frac{1}{G_0}}=\exp\left[-\frac{1}{E_{sat}}E_{in}(t)\right] \tag{D.14}$$

Solving (D.14) for *G(t)* yields:

$$G(t)=\frac{G_0}{G_0-(G_0-1)\cdot\exp\left[-\frac{1}{E_{sat}}E_{in}(t)\right]} \tag{D.15}$$

D.3 SOA Gain Recovery Characteristic Equation

After saturation the gain of the SOA recovers dues to the injection of current. To describe this process mathematically the stimulated emission term is omitted from the rate equation (D.1), to form:

$$\frac{dN(z,t)}{dt}=\frac{I_B}{qV}-\frac{N(z,t)}{\tau_c} \tag{D.16}$$

Integrating (D.16) over the length of the SOA and noting that:

$$N_{tot}(t) = \int_0^L [N(z,t) - N_{tr}]dz$$

thus,
$$\int_0^L N(z,t)\,dz = \int_0^L N_{tr}\,dz + N_{tot}(t) \qquad \text{(D.17a)}$$

The result of the integrations is:

$$\frac{d}{dt}\int_0^L N(z,t)\,dz = \int_0^L \frac{I_B}{qV}\,dz - \frac{1}{\tau_c}\int_0^L N(z,t)\,dz \qquad \text{(D.17b)}$$

Thus,

$$\frac{dN_{tot}(t)}{dt} = \int_0^L \frac{I_B}{qV}dz - \frac{1}{\tau_c}\int_0^L N(z,t)\,dz \qquad \text{(D.17c)}$$

$$= \int_0^L \frac{I_B}{qV}dz - \frac{1}{\tau_c}\left[\int_0^L N_{tr}\,dz + N_{tot}(t)\right] \qquad \text{(D.17d)}$$

$$= \left(\frac{I_B}{qV} - \frac{N_{tr}}{\tau_c}\right)\cdot L - \frac{1}{\tau_c}N_{tot}(t) \qquad \text{(D.17e)}$$

Equation D.17 may now be solved using differential equations. The first step is to multiple both sides of (D.17e) by the integrating factor and rearranging to yield (D.18)

$$\exp(t/\tau_c)\cdot\frac{dN_{tot}(t)}{dt} + \exp(t/\tau_c)\cdot\frac{1}{\tau_c}N_{tot}(t)dz = \exp(t/\tau_c)\cdot\left(\frac{I_B}{qV} - \frac{N_{tr}}{\tau_c}\right)\cdot L \qquad \text{(D.18)}$$

Thus (D.18) may be rewritten in the form,

$$\frac{d}{dt}[N_{tot}(t)\cdot\exp(t/\tau_c)] = \exp(t/\tau_c)\cdot\left(\frac{I_B}{qV} - \frac{N_{tr}}{\tau_c}\right)\cdot L \qquad \text{(D.19)}$$

Integrating both sides of (D.19) with respect to t gives:

$$N_{tot}(t)\cdot\exp(t/\tau_c)=\int_0^t\exp(t/\tau_c)\cdot\left(\frac{I_B}{qV}-\frac{N_{tr}}{\tau_c}\right)\cdot L\,dt$$

$$=\left[\exp(t/\tau_c)\cdot\left(\frac{I_B}{qV}-\frac{N_{tr}}{\tau_c}\right)\cdot L\cdot\tau_c\right]_0^t \qquad \text{(D.20)}$$

Using (D.20) the solution of the differential equation may be expressed as:

$$N_{tot}(t)=\left(\frac{I_B\tau_c}{qV}-N_{tr}\right)\cdot L-\left[\left(\frac{I_B\tau_c}{qV}-N_{tr}\right)\cdot L\cdot\exp(-t/\tau_c)\right] \qquad \text{(D.21a)}$$

$$N_{tot}(t)=[N(z,t)-N_{tr}]\cdot L-[(N(z,t)-N_{tr})\cdot L\cdot\exp(-t/\tau_c)] \qquad \text{(D.21b)}$$

Recall from (D.10) that

$$G(t)=\exp[\Gamma\cdot g\cdot N_{tot}(t)-\alpha_{AMP}\cdot L]$$

Thus, substituting for $N_{tot}(t)$ into the above equation yields:

$$G(t)=\exp\{\Gamma\cdot g\cdot[N(z,t)-N_{tr}]\cdot L-[\Gamma\cdot g\cdot(N(z,t)-N_{tr})\cdot L\cdot\exp(-t/\tau_c)]-\alpha_{AMP}\cdot L\} \qquad \text{(D.22)}$$

Rearranging (D.22) gives:

$$G(t)=\frac{\exp(\Gamma\cdot g\cdot[N(z,t)-N_{tr}]\cdot L-\alpha_{AMP}\cdot L)}{\exp[\Gamma\cdot g\cdot(N(z,t)-N_{tr})\cdot L\cdot\exp(-t/\tau_c)]} \qquad \text{(D.23)}$$

$$G(t)\approx\frac{G_0}{G_0^{\exp(-t/\tau_c)}}$$

$$= G_0 \cdot \left(\frac{1}{G_0} \right)^{\exp(-t/\tau_c)} \tag{D.24}$$

Thus the momentary gain during the recovery period may be given as:

$$G(t) = G_0 \cdot \left[\frac{G(t_s)}{G_0} \right]^{\exp[(-t-t_s)/\tau_c]} \tag{D.25}$$

where t_s is the time at which saturation occurs. Note from (D.25) that at time $t = t_s$, $G(t) = G(t_s)$ and for $t >> t_s$, $G(t) = G_0$.

REFERENCES

1. Eiselt, M., Pieper, W., and Weber, H. G., "SLAOLM: Semiconductor Laser Amplifier in a loop mirror," *Lightwave Technology, Journal of*, vol. 13, no. 10, pp. 2099-2112, Oct.1995.

2. Agrawal GP: Applications of Nonlinear Fiber Optics., Academic Press, 2001.